



# Garibaldi Geothermal Energy Project - Phase 2 Mount Cayley 2021 Field Report

Geoscience BC Report 2022-14

Grasby, S.E., Barendregt, R.W., Borch, A., Calahorrano-DiPatre, A., Chen, Z., Hanneson, C., Harris, M., Quane, S.L., Russell, J.K., Slobodian, E.G., Unsworth, M.J., Williams-Jones, G., Yuan, W.



# Garibaldi Geothermal Energy Project – Phase 2

## Mount Cayley 2021 Field Report

Grasby, S.E.<sup>1</sup>, Barendregt, R.W.<sup>1</sup>, Borch, A.<sup>3</sup>, Calahorrano-DiPatre, A.<sup>4</sup>, Chen, Z.<sup>1</sup>, Hanneson, C.<sup>5</sup>, Harris, M.<sup>3</sup>, Quane, S.L.<sup>6</sup>, Russell, J.K.<sup>3</sup>, Slobodian, E.G.<sup>1</sup>, Unsworth, M.J.<sup>5</sup>, Williams-Jones, G.<sup>4</sup>, Yuan, W.<sup>1</sup>

<sup>1</sup>Geological Survey of Canada, <sup>2</sup>The University of Lethbridge, <sup>3</sup>University of British Columbia, <sup>4</sup>Simon Fraser University, <sup>5</sup>University of Alberta, <sup>6</sup>Sea to Sky Fire & Ice Geopark

### INDEX

Chapter 1 – The Garibaldi Volcanic Belt Geothermal Energy Project – Phase 2.....	1
Grasby, S.E., Barendregt, R.W., Borch, A., Calahorrano-DiPatre, A., Chen, Z. Hanneson, C., Harris, M., Quane, S.L., Russell, J.K., Slobodian, E.G., Unsworth, M.J., Williams-Jones, G., Yuan, W.	
Chapter 2 – Results of <sup>40</sup> Ar/ <sup>39</sup> Ar Age-Dating in Support of the Garibaldi Geothermal Initiative .....	5
Harris, M., and Russell, J.K.	
Chapter 3 – Distribution and Age of the Cheakamus Basalts, Garibaldi Volcanic Belt, British Columbia..	14
Borch, A., Russell, J.K., Barendregt, R. W., and Quane, S.L.	
Chapter 4 – Gravity Survey at Mount Meager and Mount Cayley Volcanic Complexes.....	34
Calahorrano-Di Patre, A., Williams-Jones, G.	
Chapter 5 – Summary of Broadband Magnetotelluric Measurements in the Garibaldi Volcanic Belt in August 2021.....	55
Unsworth, M.J., Hanneson, C., Slobodian, E.G.	
Chapter 6 – Ground Temperature Data and Fracture System Analyses of the Mount Meager and Mount Cayley Areas .....	82
Chen, Z., Grasby, S.E., Yuan, W.	

# Chapter 1 – The Garibaldi Volcanic Belt Geothermal Energy Project – Mount Cayley 2021 Field Report

Grasby, S.E.<sup>1</sup>, Barendregt, R.W.<sup>1</sup>, Borch, A.<sup>3</sup>, Calahorrano-DiPatre, A.<sup>4</sup>, Chen, Z.<sup>1</sup>, Hanneson, C.<sup>5</sup>, Harris, M.<sup>3</sup>, Quane, S.L.<sup>6</sup>, Russell, J.K.<sup>3</sup>, Slobodian, E.G.<sup>1</sup>, Unsworth, M.J.<sup>5</sup>, Williams-Jones, G.<sup>4</sup>, Yuan, W.<sup>1</sup>

<sup>1</sup>Geological Survey of Canada, <sup>2</sup>The University of Lethbridge, <sup>3</sup>University of British Columbia, <sup>4</sup>Simon Fraser University, <sup>5</sup>University of Alberta, <sup>6</sup>Sea to Sky Fire & Ice Geopark

## Introduction

To meet climate targets of net zero CO<sub>2</sub> emissions by 2050, Canada requires development of new renewable energy resources. Numerous renewable energy options are being examined but these have a common problem of not being dispatchable (ramping up and down to meet changing load demand) nor reliable (e.g., wind and solar are dependent on weather conditions). As such these renewables require storage solutions to form a significant portion of the energy supply. Compared to other renewables, geothermal energy has numerous advantages, the most important of which is the ability to provide a stable baseload-power supply. However, this greater reliability comes with much greater exploration risk. While it is relatively easy to determine where it is windy and sunny, defining a hot aquifer in the deep subsurface ultimately requires expensive drilling operations. Geoscience research is essential for developing new approaches to reduce this exploration risk.

Canada initiated a Geothermal Energy Program, in response to the global Energy Crisis of the 1970's, that ran from 1975-1985. This program provided the first insight into the thermal regime of Canada (Jessop, 2008; Grasby et al., 2011). This work included defining some of the highest temperature geothermal systems in Canada, those related to hot sedimentary basins (found in the Northwest Territories, Yukon, British Columbia [BC], Alberta and Saskatchewan), as well as volcanic belts (Yukon and BC). As part of this earlier program, geothermal-exploration wells were drilled in the Garibaldi Volcanic Belt of Southwest BC, near active thermal springs on the southern flank of Mount Meager, as well as further south on the southern flank of Mount Cayley. This drilling was a technical success, defining high-temperature geothermal resources exceeding 250 °C (Jessop, 2008; Witter, 2019). However, the project was never economically viable because flow rates were too low to justify the power-transition cost over the distance required. Ultimately, development was limited by the low permeability rocks at depth. Subsequent industry drilling at Mount Meager defined higher permeability zones (Witter, 2019) but these have not been produced to date as the water tables were too far below the well pad, such that parasitic pumping costs were too high.

Interest in geothermal potential in Canada has revived over the last decade with growing concern over CO<sub>2</sub> emissions. This has led to initiation of a research project to help reduce exploration risk for geothermal energy associated with volcanic systems in Canada. The main aim of this work is to develop new techniques and tools that can better predict the occurrence of hot and permeable aquifers in the subsurface. To this end, a multidisciplinary geoscience field program was conducted at Mount Meager in the summer of 2019, with a reduced program in 2020 due to COVID-19 restrictions (Grasby et al., 2021). A second phase of this work was initiated in 2021 to examine the geothermal potential of the Mount Cayley area. This report summarises work completed to date and provides all data collected from the summer 2021 field season.

## Methods

Access to the Mount Cayley area can be had on a network of old logging roads along the east and west flanks of the massif. Higher elevation locations required helicopter access. COVID-19 restrictions had significant impact on the 2021 field program, reducing total personnel in the field and eliminating helicopter sharing during the day, such that only one field crew went out each day. Field staff were also required to stay in individual hotel rooms based in Whistler to be close to the heliport.

The field program in 2021 focused on: bedrock mapping and age dating of the volcanic eruption history (UBC); a gravity survey (SFU); establishing an array of magnetotelluric (MT) stations focused on the deeper volcanic plumbing (UofA); and ground temperature and fracture studies (GSC).

The volcanic history of the Garibaldi Volcanic Belt can provide some insight into areas with higher temperatures related to shallower magma chambers. Such knowledge can also aid in assessment of the volcanic hazards associated with any future development. Given this, work was conducted to refine the eruptive history of the core Garibaldi Belt area (Chapters 2 and 3). Results show that mafic volcanism spans a greater and older range of ages than previously thought. As well, novel combination of <sup>40</sup>Ar/<sup>39</sup>Ar with paleomagnetic studies helped to refine the total eruptive history of some events. The results also provided new insight into the history of the Cordilleran Ice Sheet over the past 500 ka, with newly dated glaciovolcanic deposits showing that ice reached elevations of 1650 and 2000 m a.s.l. at ~450 ka and ~200 ka, respectively. Whereas newly dated subaerial erupted lavas recorded an absence of ice at elevations below 1700 m a.s.l. at ~500 ka and again at ~115 ka (Chapter 2).

New work was also conducted on the Cheakamus basalts, to build on work completed in 2020 and report new observations and data from the 2021 field mapping program (Chapter 3). Here we present the revised stratigraphy and eruptive phases, the presumed source location (i.e., vent), expanded paleomagnetic study, and new <sup>40</sup>Ar/<sup>39</sup>Ar ages of the basalts. These results inform on a more precise distribution of some of the youngest lavas in the Garibaldi Volcanic Belt, as well as the age and duration of volcanism.

Gravity measurements were taken at 75 stations around the Mount Cayley complex with the aim of mapping the internal structure (Chapter 4). Results will be equally useful to understand the geothermal potential of both areas, and to identify possible geohazards that might impact future developments.

Collection of MT data was aimed at expanding coverage beyond previous studies and the Lithoprobe MT survey along the Sea-to-Sky Corridor using modern and more field-portable instruments (Chapter 5). A

set of 11 MT measurements was taken by the UofA MT group to understand the deeper structure of the volcanic system; this required longer recording time and consequently reduced the total number of measurement locations (Chapter 5). The deeper focus MT survey was designed to image pathways that carry fluids to the geothermal reservoir. Results produced high quality data that are consistent with legacy data from Lithoprobe.

New work was conducted to test the utilisation of ground temperature monitoring, where a series of 22 data loggers were placed in a grid to monitor ground temperatures over 330 days (Chapter 6). Initial temperature data has been collected and recording is ongoing. In addition, over 400 new fracture measurements were collected across the Mount Caley area to characterize potential reservoir properties. This work is ongoing and will be incorporated with additional data collected in 2022.

Plans are underway for a summer 2022 field season that will complete Phase2 data collection. Full results and interpreted data will also be released in a revised version of this report along with published peer reviewed science papers and university theses.

## Data Collected

New data has been collected as part of this research activity. Data are either included as tables within this report, or as online resources from Geoscience BC. The table below indicates the data available.

Report section	Data type	Source
Chapter 2	Bedrock age dates	This report
Chapter 3	1) Paleomagnetic data 2) Bedrock age dates	1) This report 2) This report
Chapter 4	Gravity measurements	This report
Chapter 5	MT time series data	Geoscience BC
Chapter 6	1) Ground temperature records 2) Fracture orientations	1) Geoscience BC 2) Geoscience BC

## References

- Grasby, S.E., Allen, D.M., Bell, S., Chen, Z., Ferguson, G., Jessop, A., Kelman, M., Ko, M., Majorowicz, J., Moore, M., Raymond, J. and Therrien, R. (2011): Geothermal energy resource potential of Canada; Geological Survey of Canada, Open File 6914, 322 p., <<https://doi.org/10.4095/288745>>[October 2019].
- Grasby, S. E., Ansari, S. M., Barendregt, R. W., Borch, A., Calahorrano-DiPatre, A., Chen, Z., Craven, J. A., Dettmer, J., Gilbert, H., Hanneson, C., Harris, M., Hormozzade, F., Leiter, S., Liu, J., Muhammad, M.,

Quane, S. L., Russell, J. K., Salvage, R. O., Savard, G., Tschirhart, V., Unsworth, M.J., Vigouroux-Caillibot, N., Williams Jones, G., Williamson, A., and Vestrum, Z. E. (2021). Garibaldi Geothermal Energy Project - Phase 1 Final Report. *Geoscience BC Report, 2021-08*.

Jessop, A. (2008): Review of National Geothermal Energy Program, Phase 2 – geothermal potential of the Cordillera; Geo-logical Survey of Canada, Open File 5906, 86 p., <<https://doi.org/10.4095/225917>>[October 2019].

Jones, A.G. and Dumas, I. (1993): Electromagnetic images of a volcanic zone; *Physics of the Earth and Planetary Interiors*, v. 81, no. 1-4, p. 289-314, <[https://doi.org/10.1016/0031-9201\(93\)90137-X](https://doi.org/10.1016/0031-9201(93)90137-X)>[October 2019].

Witter, J. (2019): South Meager geothermal project – new perspectives from recently unearthed data; Geoscience BC, Report 2019-07, 5 p., URL <<http://www.geosciencebc.com/i/pdf/Report-2019-07-Innovate-Geothermal.pdf>>[November 2019].

# Chapter 2 – Results of $^{40}\text{Ar}/^{39}\text{Ar}$ Age-Dating in Support of the Garibaldi Geothermal Initiative

Harris, M. and Russell, J.K.

Volcanology and Petrology Laboratory  
Earth, Ocean, and Atmospheric Sciences  
The University of British Columbia, Vancouver BC

## Introduction

The Mount Meager Volcanic Complex (MMVC), within the Garibaldi Volcanic belt (GVB) of Southwest British Columbia (BC), is an active volcanic system identified for its geothermal potential (Lewis and Souther, 1978; Jessop, 1998; Grasby and Salas, 2020). As part of Natural Resources Canada's (NRCan) continued MMVC geothermal exploration program, we collected a suite of six new volcanic samples for  $^{40}\text{Ar}/^{39}\text{Ar}$  age-dating (Fig 1; Table 1). Our rationale for this work was to provide new data that can inform upon the eruptive history of the MMVC. Our work has bolstered geochronological data for the MMVC, which will aid future geologists in assessing recurrence intervals for the volcanic eruptions, which inform on both magmatic recharge rates and overall hazard for the volcanic complex.

## Methods

Widespread mapping was done across the MMVC and nearly 200 geologic samples were collected to build upon prior studies such as Woodsworth (1977), Read (1979, 1990), and Green et al., (1988). The new mapping and sample collections as part of this work were focused on previously understudied areas of the volcanic complex (e.g., Harris et al., 2020; Harris and Russell, 2021) and included a small suite of samples from newly mapped geological deposits for age-dating. Sample selection criteria are based on whether the geological samples were fresh, unaltered, holocrystalline, and contained non-vesiculated groundmasses. Samples were irradiated at the research reactor at Oregon State University, USA, and analytical procedures were conducted at WiscAr Labs, University of Wisconsin-Madison, USA. For each sample, 10-15 mg of groundmass was separated into a 5 mm diameter well, cut in a copper planchet. A 60 W  $\text{CO}_2$  laser beam of a Noblesse 5 Collector Mass Spectrometer was then defocused to a 4 mm diameter to evenly heat the entire sample during each heating step of the analyses. Instrument detectors simultaneously measured  $^{40}\text{Ar}/^{39}\text{Ar}$ ,  $^{36}\text{Ar}/^{39}\text{Ar}$ , and  $^{37}\text{Ar}/^{39}\text{Ar}$  ratios through cycles of beam switching. Ages were calculated relative to the 1.1864 Ma Alder Creek sanidine standard (Jicha et al., 2016). Argon decay constants and isotopic abundances are after Min et al. (2000). Plateau ages were determined from the inverse-variance-weighted mean of selected steps. The errors on the plateau age are reported as  $2\sigma$  calculated by multiplying the inverse-variance-weighted mean error (Taylor, 1982) by root MSWD where  $\text{MSWD} > 1$ .

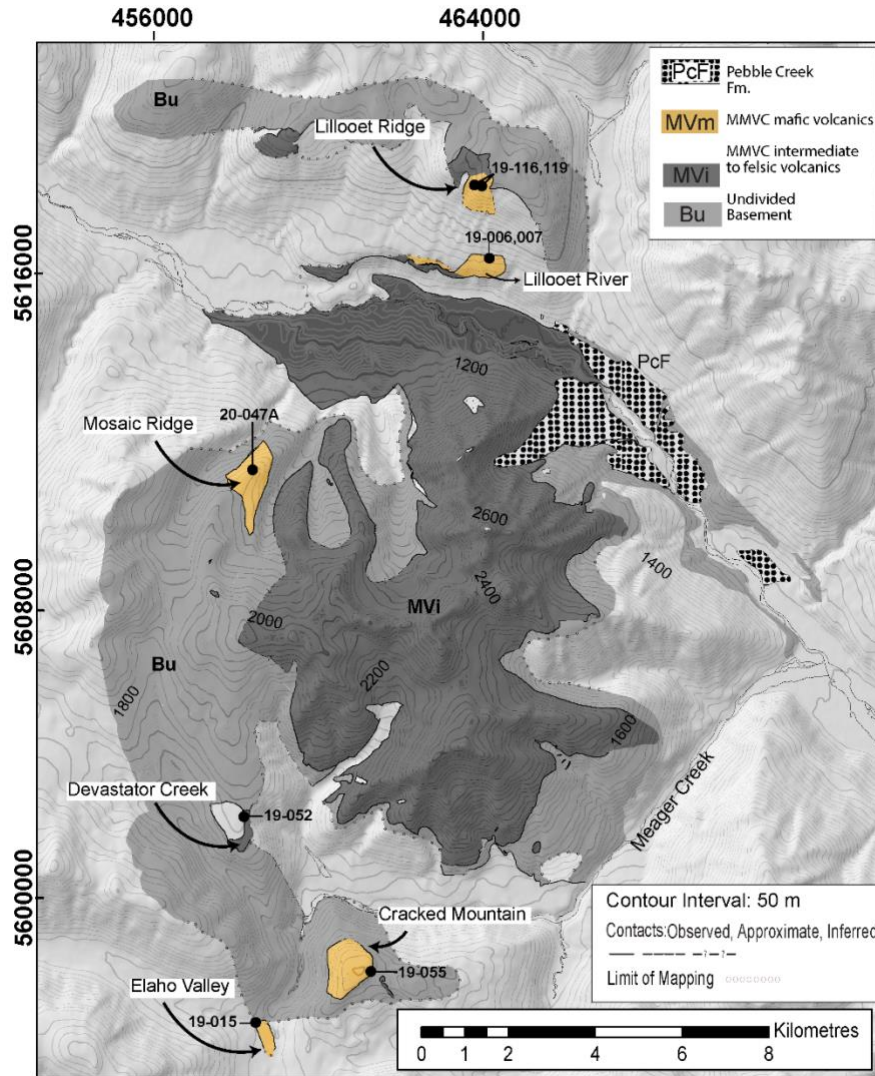


**Figure 1.** Undivided geological map of MMVC shows the distribution of intermediate volcanic (MVi) and peripheral mafic volcanic rocks (MVm) overlying basement lithologies (Bu). Distributions are based on maps of Read (1979), Woodsworth (1977), and our own field mapping. The youngest MMVC eruption, 2350 B.P. Pebble Creek Formation (PcF) is distinguished from other volcanic deposits (Hickson et al., 1999; Stewart et al., 2008). Locations of samples selected for  $^{40}\text{Ar}/^{39}\text{Ar}$  dating are shown by filled circles and sample labels (Table 1).

**Table 1.**  $^{40}\text{Ar}/^{39}\text{Ar}$  data for Mount Meager Volcanic Complex based on samples prepared and analysed by WiscAr laboratories, University of Wisconsin-Madison, Madison WI, USA.

Samples	UTM Easting	UTM Northing	Material	$^{40}\text{Ar}/^{36}\text{Ar}_i \pm 2s$	Isochron			MSWD	Plateau
					Age (ka) $\pm 2s$	N	$^{39}\text{Ar}$ %		Age (ka) $\pm 2s$
<b>Devastator Creek</b>									
MH-19-052	457900	5603470	groundmass	$297.3 \pm 2.4$	$502.7 \pm 6.6$	14/17	92.8	1.13	$499.7 \pm 3.7$
<b>Lillooet River</b>									
MH-19-007	464179	5616808	groundmass	$297.2 \pm 2.2$	$450.9 \pm 17.7$	15/15	100.0	1.16	$441.7 \pm 9.8$
MH-19-006	464179	5616808	groundmass	$299.0 \pm 2.2$	$454.8 \pm 10.0$	15/17	99.8	1.06	$456.5 \pm 5.8$
<b>Cracked Mountain</b>									
MH-19-055	461014	5599824	groundmass	$298.3 \pm 2.0$	$413.5 \pm 88.8$	24/24	100.0	0.49	$401.6 \pm 38.1$
<b>Lillooet Ridge</b>									
MH-19-116	463843	5618872	groundmass	$300.0 \pm 2.9$	$197.8 \pm 16.1$	18/18	100.0	0.59	$205.1 \pm 6.5$
MH-19-119	463789	5619051	groundmass	$298.1 \pm 1.5$	$206.8 \pm 20.0$	21/21	100.0	1.12	$201.1 \pm 11.8$
<b>Mosaic Ridge</b>									
MH-20-047A	457933	5611861	groundmass	$296.9 \pm 2.8$	$127.6 \pm 22.6$	13/13	100.0	0.26	$115.2 \pm 9.7$
<b>Elaho Valley</b>									
MH-19-015	458120	5598544	groundmass	$296.1 \pm 3.8$	$126.5 \pm 31.4$	11/15	88.3	0.65	$106.3 \pm 11.0$

Ages calculated relative to 1.1864 Ma Alder Creek sanidine standard using the decay constants of Min et al. (2000).

Atmospheric  $^{40}\text{Ar}/^{36}\text{Ar} = 298.56 \pm 0.62$  (Lee et al., 2006)

N = number of plateau steps/number of total incremental heating steps

## Results

### **Devastator Creek**

The Devastator Creek lava was first identified by Harris et al. (2020) and was included in Harris and Russell's (2021) geological map of west MMVC. This newly described lava outcrops on the southwest flank of the Mount Meager massif ~2 km NW of Devastator Creek at ~1700 m a.s.l. (Fig. 1). The lava is a subaerial, columnar jointed dacite and the sample sent to the WiscAr lab for age-dating (19-052) (Fig. 1; Table 1) returned a plateau age of  $499.7 \pm 3.7$  ka and an isochron age of  $502.7 \pm 6.6$  ka (Fig. 2A, 3A).

### **Lillooet River**

The Lillooet River volcanic deposits are located in the north MMVC, exposed above the present day Lillooet River (Fig. 1). Samples were collected at a waterfall formed by a cliff of basaltic hyaloclastites at ~1100 m a.s.l. (Harris et al., 2020; Harris and Russell, 2021). Multiple dykes intrude the cliffs of hyaloclastite and geochemical analyses of hyaloclastite material and dykes show they are sourced from the same magma. The morphology of the deposit and types of lithofacies present at the waterfall exposure indicate a glaciovolcanic origin. Two dyke samples were sent to WiscAr lab, 19-006 and 19-007 (Fig. 1; Table 1) and they returned plateau ages of  $456.5 \pm 5.8$  ka and  $441 \pm 9.8$  ka respectively (Figs. 2B and C). Isochron ages are  $454.8 \pm 10.0$  ka and  $450.9 \pm 17.7$  ka respectively (Figs. 3B and C).

### ***Cracked Mountain***

Cracked Mountain is a subglacial landform located in the southwest corner of the MMVC (Fig. 1; Wilson and Russell, 2018). The edifice has a summit at ~1650 m a.s.l and comprises basaltic tephra, subvolcanic dykes, and pillow lava (Harris et al., 2020; Harris and Russell, 2021). Field based analyses and paleomagnetic data indicate a single monogenetic eruption. Two samples were sent to WiscAr lab, 19-031 (dyke) and 19-055 (pillow lava interior) (Fig. 1; Table 1). Sample 19-031 was overloaded with excess argon and, thus, did not yield an age. Sample 19-055 had low radiogenic argon but returned a plateau age of  $401 \pm 38$  ka and isochron age of  $413 \pm 88.8$  ka (Figs. 2D, 3D).

### ***Lillooet Ridge***

The Lillooet Ridge basalts are located north of the MMVC, across and ~2 km above the present day Lillooet River at elevations of ~2000 m a.s.l. (Fig. 1). The deposits are radially jointed pods of basaltic pillow lava, hyaloclastites, and dykes. The location and type of lithofacies indicate a glaciovolcanic origin, and the petrochemical signatures indicate that these basalts are different than the basalts exposed within the Lillooet River valley (Harris and Russell, 2021). Two samples were sent to WiscAr lab Samples, 19-116 and 19-119 (dykes) (Fig. 1, Table 1). Their plateau ages are  $205 \pm 6.5$  and  $201.1 \pm 11.8$  ka respectively (Figs. 2E and F). The isochron ages are  $197.8 \pm 16.1$  ka and  $206.8 \pm 20.0$  ka respectively (Figs. 3E and F).

### ***Mosaic Ridge***

The Mosaic Ridge lavas are located in the northwest flank of Mount Meager Massif (Fig. 1) (Read, 1979, 1990). The deposits are a series of subaerial basaltic lavas, tephra, and dykes that outcrop at ~1700 m a.s.l. One sample was sent to WiscAr lab, 20-047A (dyke) (Fig. 1; Table 1). The sample returned a plateau age of  $115.2 \pm 9.7$  ka and an isochron age of  $127.6 \pm 22.6$  ka (Figs. 2G, 3G).

### ***Elaho Valley***

The Elaho Valley lavas are located in the southwest corner of the MMVC (Fig 1). The basalt lavas are subaerial, source at elevations above (i.e. > ~1000 m a.s.l.) the waterfall at the head of the Elaho Valley, and extend ~20 km south of the waterfall (Woodsworth, 1977; Read, 1990). Samples 19-015 and 19-018A were sent to the WiscAr lab, (Table 1). Sample 19-018A was overloaded with atmospheric argon and undatable. Sample 19-015 returned a plateau age of  $106.3 \pm 11.0$  ka and an isochron age of  $126.5 \pm 31.4$  ka (Figs. 2H, 3H).

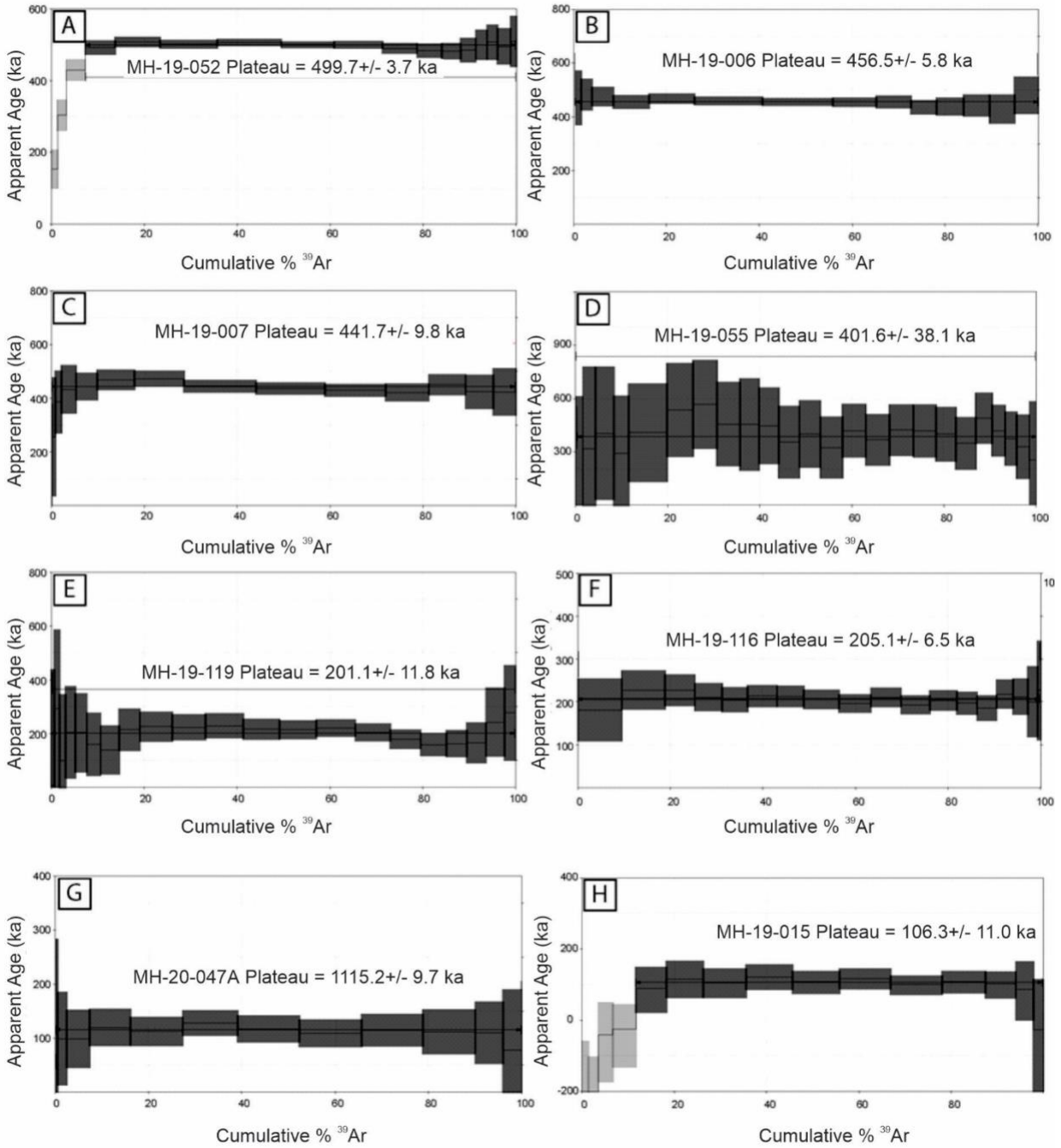


**Figure 2.**  $^{40}\text{Ar}/^{39}\text{Ar}$  geochronometry for samples from six previously undated volcanic deposits within the MMVC. Plateau diagrams show individual heating steps used to integrate the plateau age for each sample. The height of individual boxes (steps) is  $2\sigma$  error.

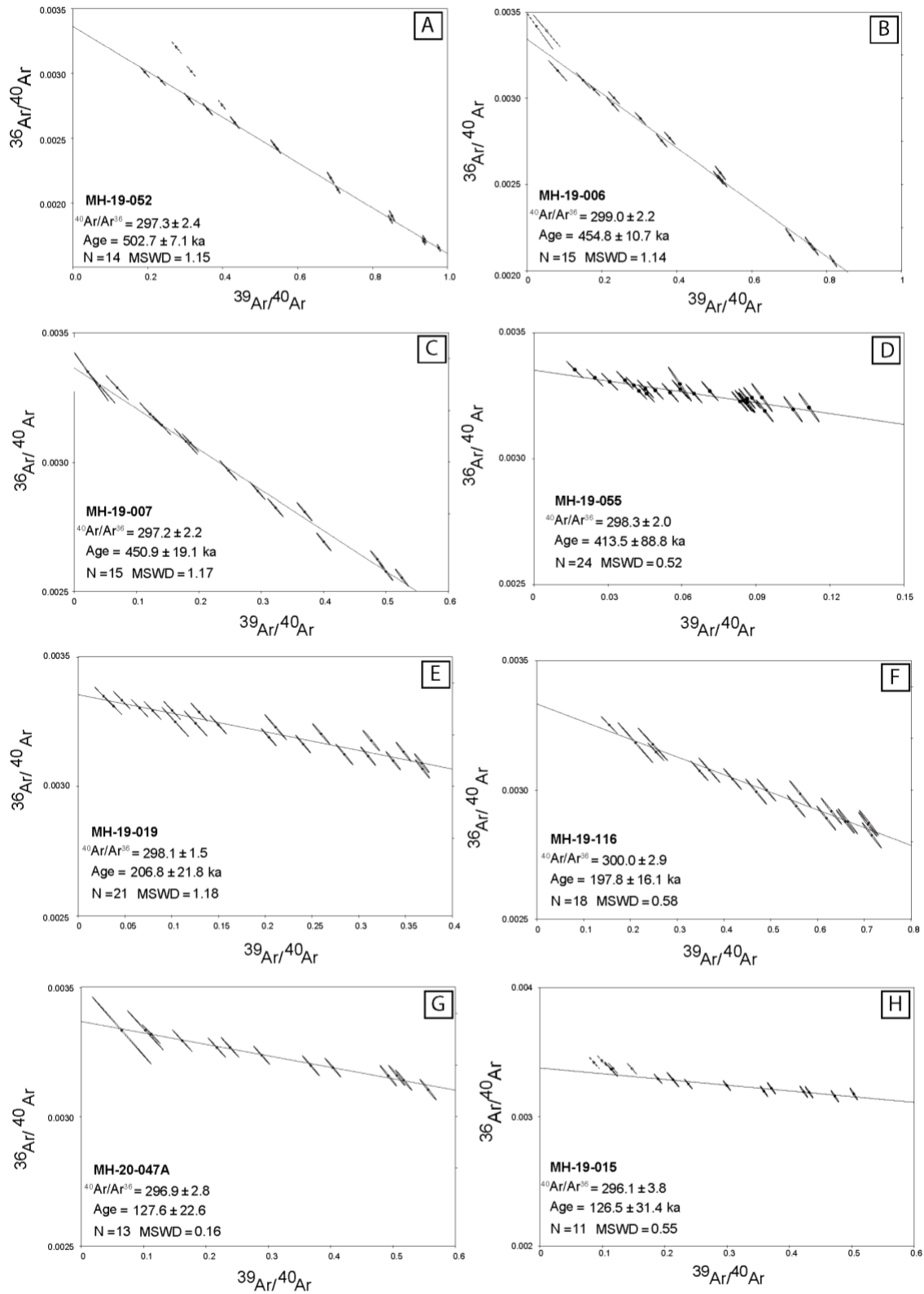


**Figure 3.**  $^{40}\text{Ar}/^{39}\text{Ar}$  geochronometry for samples from six previously undated deposits within the MMVC. Inverse isochron plots display all heating steps for each sample. Ellipses show  $2\sigma$  errors for each step.

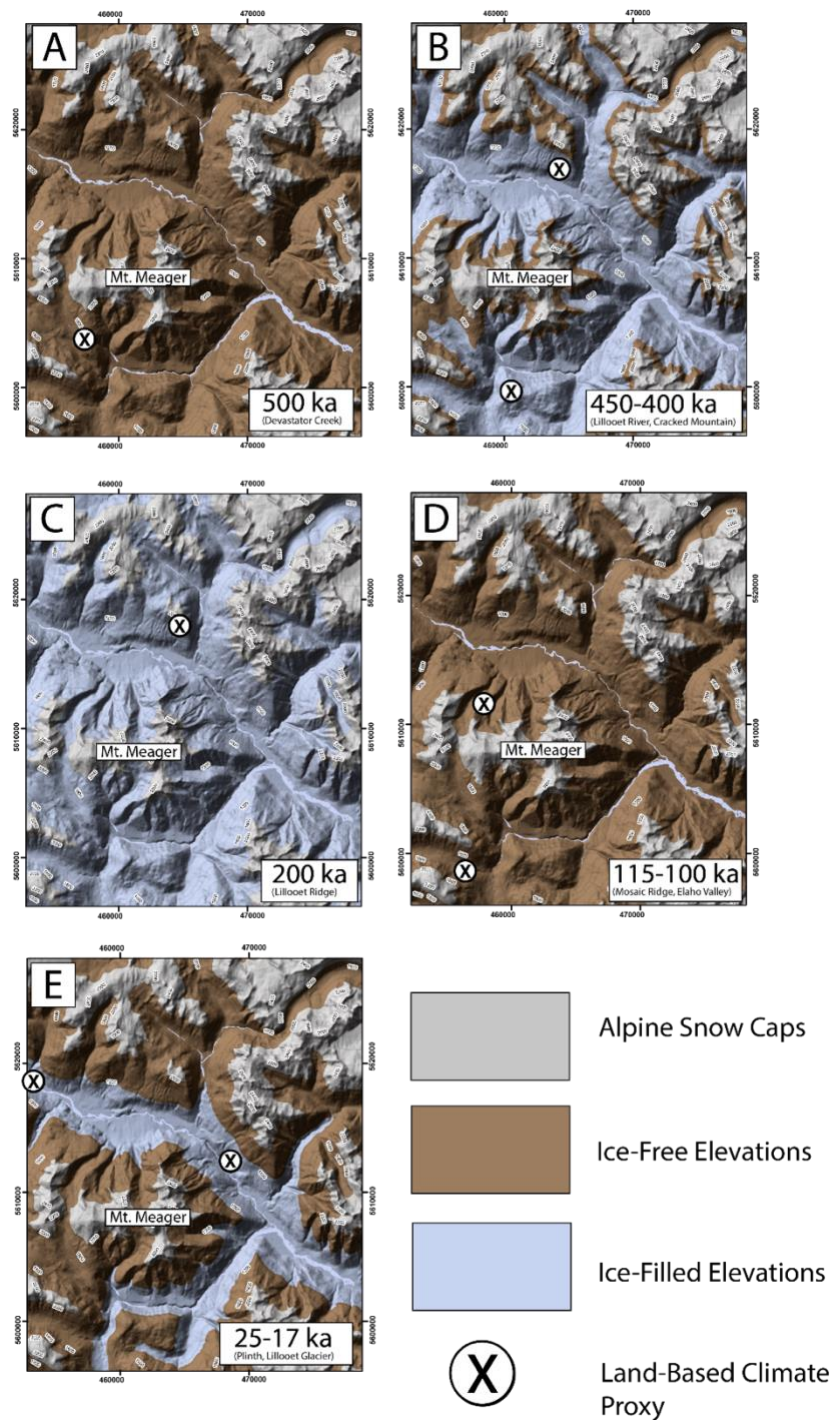


**Figure 4.** Paleo-glacial reconstructions for the MMVC over the last 500 ka shown on hillshade DEMs and illustrating distributions of glacial ice (blue) vs. ice-absent regions (brown) and high-elevation snow caps (grey). Ice-elevation models are based on land-based records of precisely dated volcanic deposits (shown with an X). A) subaerial Devastator Creek lava requires a minimum ice-free environment up to 1700 m at ~500 ka. B) Lillooet River and Cracked Mountain glaciovolcanic deposits require glacial ice up to a

minimum height of 1650 m at ~450 ka. C) Lillooet Ridge glaciovolcanic deposits require valley-filling ice up to ~2000 m at ~200 ka. D) subaerial Mosaic Ridge and Elaho Valley lavas require ice-free environments below a minimum elevation of 1700 m at ~115 ka. E) the Plinth block and ash (Russell et al., 2021) and Lillooet Glacier Basalts (Wilson and Russell, 2017, 2018) glaciovolcanic deposits require that valley filling glaciers were present at elevations up to ~1000 m at ~25 ka.

## Age Relationships and Implications

Our new  $^{40}\text{Ar}/^{39}\text{Ar}$  age dates indicate six discrete eruptive events within the MMVC over the past 500 ka. These data show that mafic volcanism within the MMVC spans a greater and older range of ages than previously shown by Green et al., (1988) and Read (1990). We identify three separate periods of mafic volcanism: a) ~450-400 ka (Lillooet River and Cracked Mountain), b) ~200 ka (Lillooet Ridge), and c) ~115-100 ka (Mosaic Ridge and Elaho Valley). The evidence of Fraser Glaciation (~25 ka) (Fig. 4E) within the MMVC has been documented through prior glaciovolcanic studies (e.g., Wilson and Russell, 2017; Russell et al., 2021) and our new age-dates expand the knowledge of a localized waxing and waning of Cordilleran ice sheet (CIS) across the MMVC throughout the late Pleistocene. Similarly, the data presented here have regional paleoenvironmental implications and provide land-based records for the presence and absence of previous incarnations of the CIS over the past 500 ka. The newly dated glaciovolcanic deposits at the Lillooet River, Cracked Mountain, and Lillooet Ridge show that progenitors of the CIS reached minimum elevations of 1650 and 2000 m a.s.l. at ~450 ka and ~200 ka, respectively (Figs. 4B and C). Conversely, the newly dated subaerial erupted lavas record an absence of the CIS at elevations below 1700 m a.s.l. at ~500 ka (Devastator Creek) and again at ~115 ka (Mosaic Ridge and Elaho Valley) (Figs. 4A and D).

## Summary

Here we present new  $^{40}\text{Ar}/^{39}\text{Ar}$  age dates for six late-Pleistocene eruptions within the MMVC. Our findings provide the first age constraints for the newly mapped Devastator Creek lavas, Cracked Mountain volcano, Lillooet River, and Lillooet Ridge volcanic deposits. We also provide new dates for the Mosaic Ridge and Elaho Valley lavas with smaller uncertainties than reported in prior studies (Woodsworth, 1977; Green et al., 1988; Read, 1990). Overall, this new collection of data bolsters the understanding of volcanic activity within the MMVC over the past 500 ka.

## References

- Grasby, S.E., and Salas, C., 2020, Searching for Mount Meager's Geothermal Heart: EOS, v. 101, doi:<https://doi.org/10.1029/2020EO140214>.
- Green, N.L., Harakal, J.E., Souther, I.J.G., and Read, P.B., 1988, Eruptive history and K-Ar geochronology of the late Cenozoic Garibaldi volcanic belt, southwestern British Columbia: Geological Society of America Bulletin, v. 100, p. 563–579.
- Harris, M., Muhammad, M., Williams-Jones, G., and Russell, J.K., 2020, Bedrock mapping for Mount Meager Geothermal Research Initiative: Geoscience BC, p. 6–29, doi:[10.13140/RG.2.2.15103.64169](https://doi.org/10.13140/RG.2.2.15103.64169).
- Harris, M., and Russell, J.K., 2021, Bedrock Mapping Results for the Mount Meager Geothermal Research Initiative: Geoscience BC, p. 7–34.

- Hickson, C.J., Russell, J.K., Stasiuk, M. V, and Swanson, D.A., 1999, Volcanology of the 2350 B.P. Eruption of Mount Meager Volcanic Complex, British Columbia, Canada: implications for Hazards from Eruptions in Topographically Complex Terrain 1: *Bulletin of Volcanology*, v. 60, p. 489–507.
- Jessop, A.M., 1998, Geothermal Energy in Canada: *Geoscience Canada*, v. 25, p. 33–41.
- Jicha, B.R., Singer, B.S., and Sobol, P., 2016, Re-evaluation of the ages of  $^{40}\text{Ar}/^{39}\text{Ar}$  sanidine standards and supereruptions in the western U.S. using a Noblesse multi-collector mass spectrometer: *Chemical Geology*, v. 431, p. 54–66, doi:10.1016/j.chemgeo.2016.03.024.
- Lewis, T.J., and Souther, J.G., 1978, Meager Mountain, B.C.: a possible geothermal energy resource: *Geothermal Service of Canada*, v. 9, p. 1–17.
- Min, K., Mundil, R., Renne, P.R., and Ludwig, K.R., 2000, A test for systematic errors in  $^{40}\text{Ar}/^{39}\text{Ar}$  geochronology through comparison with U/Pb analysis of a 1.1-Ga rhyolite: *Geochimica et Cosmochimica Acta*, v. 64, p. 73–98, doi:10.1016/S0016-7037(99)00204-5.
- Read, P.B., 1979, Meager Creek Geothermal Area: p. 1 Sheet, doi:10.4095/129507.
- Read, P., 1990, Mt Meager Complex, Garibaldi Belt, Southwestern BC.: *Geoscience Canada*, v. 17, p. 167–170.
- Russell, J., Stewart, M., Wilson, A., and Williams-Jones, G., 2021, Eruption of Mount Meager, British Columbia, during the early Fraser glaciation: *Canadian Journal of Earth Sciences*, doi:10.1139/cjes-2021-0023.
- Stewart, M.L., Russell, J.K., and Hickson, C.J., 2008, Geology, Pebble Creek formation, British Columbia: p. 1 sheet.
- Taylor, J.R., 1982, *An Introduction to Error Analysis-The Study of Uncertainties in Physical Measurements*: 1–327 p.
- Wilson, A.M., and Russell, J.K., 2017, Lillooet Glacier basalts, southwestern British Columbia, Canada: Products of Quaternary Glaciovolcanism: *Canadian Journal of Earth Sciences*, v. 54, p. 639–653, doi:10.1139/cjes-2016-0201.
- Wilson, A.M., and Russell, J.K., 2018, Quaternary glaciovolcanism in the Canadian Cascade volcanic arc—Paleoenvironmental implications: *Field Volcanology: A Tribute to the Distinguished Career of Don Swanson*. Geological Society of America, v. 538, doi:10.1130/2018.2538(06).
- Woodsworth, G., 1977, Geology of Pemberton (92J) Map Area: Geological Survey of Canada, p. 1 sheet.

# Chapter 3 – Distribution and Age of the Cheakamus Basalts, Garibaldi Volcanic Belt, British Columbia

Borch, A.<sup>1</sup>, Russell, J.K.<sup>1</sup>, Barendregt, R. W.<sup>2</sup>, and Quane, S.L.<sup>3</sup>

<sup>1</sup>Earth, Ocean and Atmospheric Sciences, The University of British Columbia

<sup>2</sup>Department of Geography & Environment, The University of Lethbridge

<sup>3</sup>Sea to Sky Fire & Ice Aspiring Geopark

## Introduction

The Cheakamus River basalt lavas (herein called the Cheakamus basalts) comprise a group of Quaternary basaltic lavas within the Garibaldi Volcanic Belt (GVB) of British Columbia, Canada (Fig. 1). They are distributed within the Cheakamus River and Callaghan valleys, 30 km north of Squamish and 12 km southwest of Whistler. Our current understanding of the origins, distribution, stratigraphic relationships, and age of the Cheakamus basalts derives from the field mapping of Mathews (1948, 1958) and air photo mapping, petrological, geochemical, and geochronological studies of Green (1977, 1981, 1988, 1990).

The Cheakamus basalts are some of the youngest volcanic rocks within the GVB, based on their distribution, volume and age. As such, they have relevance for geothermal energy exploration, as well as the assessment of natural hazards within the Whistler-Squamish corridor. The Cheakamus basalts have a length of 26 km stretching from their southern limit, exposed near Daisy Lake, to Conflict Lake in the north. The lavas have lateral extents of 1-2 km and span the widths of both the Cheakamus and Callaghan River valleys. The basalt lavas cover an area of ~35 km<sup>2</sup> (Fig. 1), and where exposed in sections through paleo-valleys, reach thicknesses of 80 m; previous estimates place the minimum volume of the Cheakamus basalts at 1.25 km<sup>3</sup> (Mathews, 1958). This erupted volume is likely to be matched by 3-10 times greater volumes of stored magma (Huppert & Woods, 2002; Townsend & Huber, 2020). Geochronological data, although sparse, combined with field mapping suggest the volcanism could be as young as < 50 ka (Green, 1981; McNeely, 1989; Borch et al., 2021).

Here, we build on work completed in 2020 and report new observations and data from the 2021 field mapping program on the Cheakamus basalts. Specifically, we report on their revised stratigraphy and eruptive phases, the presumed source location (i.e., vent), expanded paleomagnetic study, and new <sup>40</sup>Ar/<sup>39</sup>Ar ages. These results inform on a more precise distribution of lavas, as well as the age and duration of volcanism.

## The 2021 Field Season

Published studies by Mathews (1958) and Green (1977, 1981) on the distribution, lithology, geochemistry and mineralogy of the Cheakamus basalts, provided some constraints on the age of volcanism and explored their paleo-environmental implications.

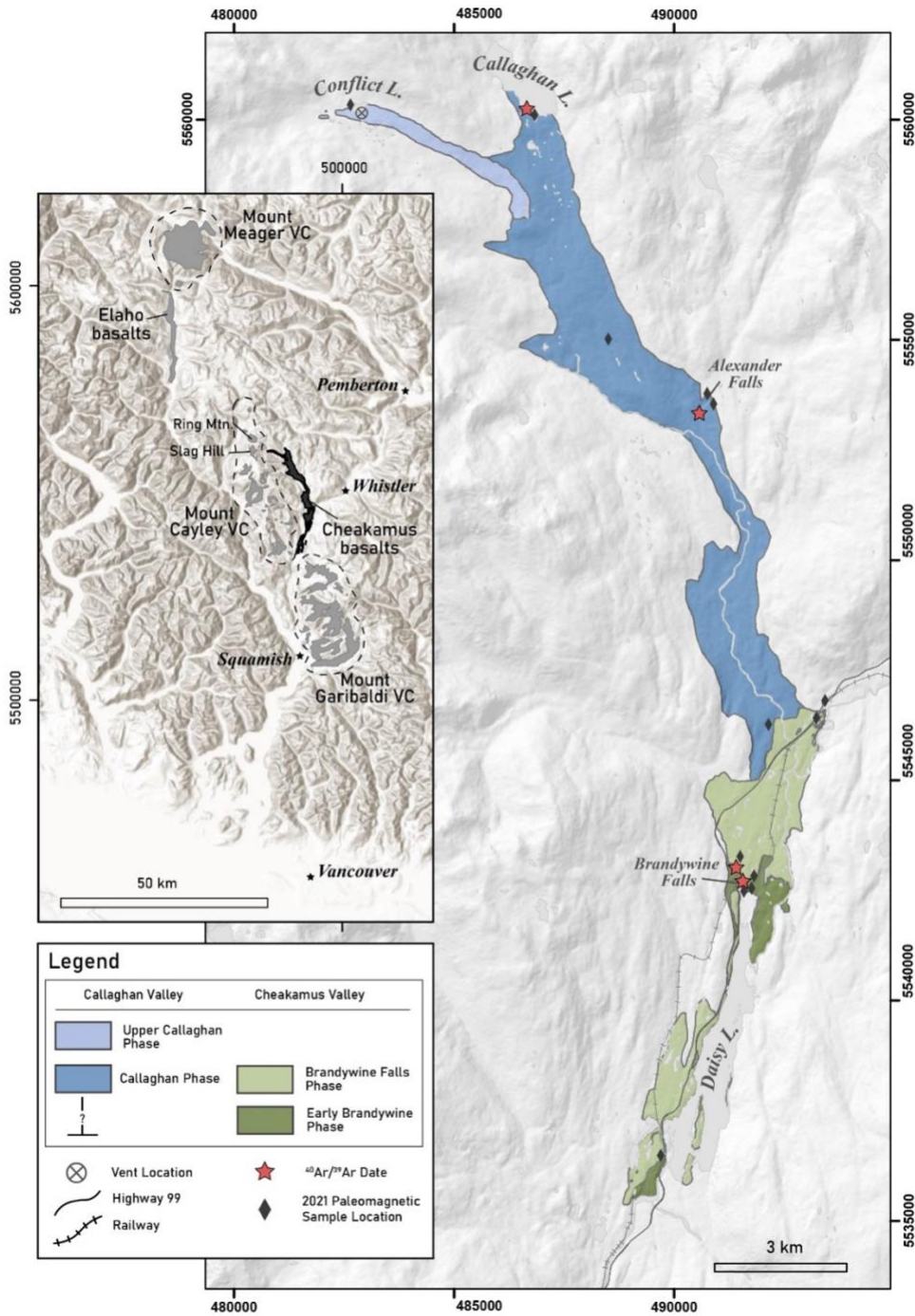


**Figure 1.** Volcanological map of the Cheakamus basalts with locations of samples used for radiometric dating and sites sampled for paleomagnetic study (see text). Inset map indicates the location of the Mount Garibaldi, Mount Cayley and Mount Meager volcanic fields, as well as the proximal Ring Mountain, Slag Hill, and Slag Hill Tuya edifices.

Our work in 2020 refined the stratigraphy, mapped distribution, and volume of the lavas and provided better constraints on age and duration of volcanism (Borch et al., 2021). In addition, preliminary paleomagnetic data from the 2020 field season indicated that the entire volume of Cheakamus basalts erupted within a very short span of time, i.e., a paleomagnetic moment of <2000 years. Lastly, Borch et al. (2021) constrained the eruption age to  $23.9 \pm 15.7$  ka based on a single  $^{40}\text{Ar}/^{39}\text{Ar}$  date for a sample collected at Brandywine Falls.

Our 2021 field-based study of the Cheakamus basalts was aimed at filling gaps in knowledge and providing a better understanding of when the basalts erupted and over what time span. Here, we report results from our 2021 field-based research programme which we use to: a) refine the stratigraphy and stratigraphic relationships of the Cheakamus basalts; b) test the initial paleomagnetic results (i.e., a single paleomagnetic moment) with study of additional sites distributed over a larger area and including localities (sites) exhibiting single as well as multiple flow sequences; c) identify the vent(s) to the Cheakamus lava field; and d) better constrain the eruption age using  $^{40}\text{Ar}/^{39}\text{Ar}$  dating. We investigated these questions using detailed lithostratigraphic analysis combined with geochemical, radiometric, and paleomagnetic analysis.

### ***Field results***

The 2021 field season comprised conventional field mapping of Cheakamus basalts, detailed stratigraphic analysis of well-exposed sections, and mapping of the lava flow surfaces for properties reflecting post-emplacement events. Detailed graphic logs were created for multiple sites in the Cheakamus Valley to inform and support the construction of map units. Distinct groups of lava were recognized on the basis of lava morphology, (micro-)phenocryst mineralogy, and key stratigraphic features including the presence of interbedded sediments and glaciated surfaces.

Our revised stratigraphic succession (Fig. 2) retains Green's Brandywine Falls phase (BFP) and associated glaciofluvial sedimentary deposits as the youngest mappable units. The BFP lavas were originally interpreted as erupting when the valley was occupied by the Fraser Glaciation ice sheet and are thought to have possibly flowed, in part, within subglacial drainage systems (i.e., 'esker-like' lavas; Mathews, 1957; Green, 1977). Green separated the BFP lavas, with their anastomosing flow shape, restricted lateral extent, and fanned entablature joint-columns from his Cheakamus Dam phase (CDP), which he describes as highly glaciated and otherwise sheet-like in morphology (1977). The two share other characteristics including scoriaceous flow bases, spiracles, vesicle cylinders, and olivine and plagioclase phenocrysts (Green, 1977). New results from 2021 field mapping suggest that the top flow of the CDP is part of the same eruptive unit as the BFP lavas. The top lavas of both the CDP and the BFP share glaciated surfaces. Discontinuous but widespread lenses of glaciofluvial sediments underly the lowest lava in the BFP and the uppermost lava in the CDP. Eruption environment indicators such as blow out cavities, squeeze ups, and minor basal palagonite are shared between both. On the basis of these similarities, we include the top flow of Green's CDP within the BFP. We suggest that the apparent difference in morphology between the BFP and Green's uppermost CDP may be the result of abrupt spatial changes in paleo-eruptive environment, where the northern Cheakamus Valley may have been partially blocked by advancing or retreating glacial ice or associated meltwater while the southern portion of the valley remained ice-free.

Underlying the Brandywine Falls phase, we define the Early Brandywine phase as including all but the top flow of Green’s Cheakamus Dam phase (Green, 1977) as well as Green’s entire Alpine Lodge phase. Originally, Green (1977) separated the Alpine Lodge phase (ALP) into two parts (i.e., I and II) based on the highly irregular, undulatory nature of their contact (Fig. 2). He interpreted the contact irregularities as comprising erosional channels incised into the upper surface of ALP I lavas and indicative of a considerable passage of time between eruptive phases. Our re-examination of this undulatory contact at a number of locations suggests that it is not an unconformity, but a primary feature produced by overlapping lava lobes of variable thickness. Green’s type locality for the Alpine Lodge phase(s) is located at the Cheakamus basalts’ southernmost extent. This location is at the front of the lava field where the gradient is less steep relative to the more proximal-to-source valleys. Here, the advancing lava front is likely to feature more individual breakout lobes of varying thicknesses whilst, to the north and towards the source, the lavas are confined to steep narrow valleys and occur as broad sheet-like layers. Lastly, there are no significant petrographic differences between lavas of the Alpine Lodge and Cheakamus Dam phases; all lavas are olivine+plagioclase porphyritic basalts and contain variable abundances of strongly-zoned, sieve-textured plagioclase xenocrysts. Future laboratory work will continue to test our grouping of the two phases into the single Early Brandywine Phase.

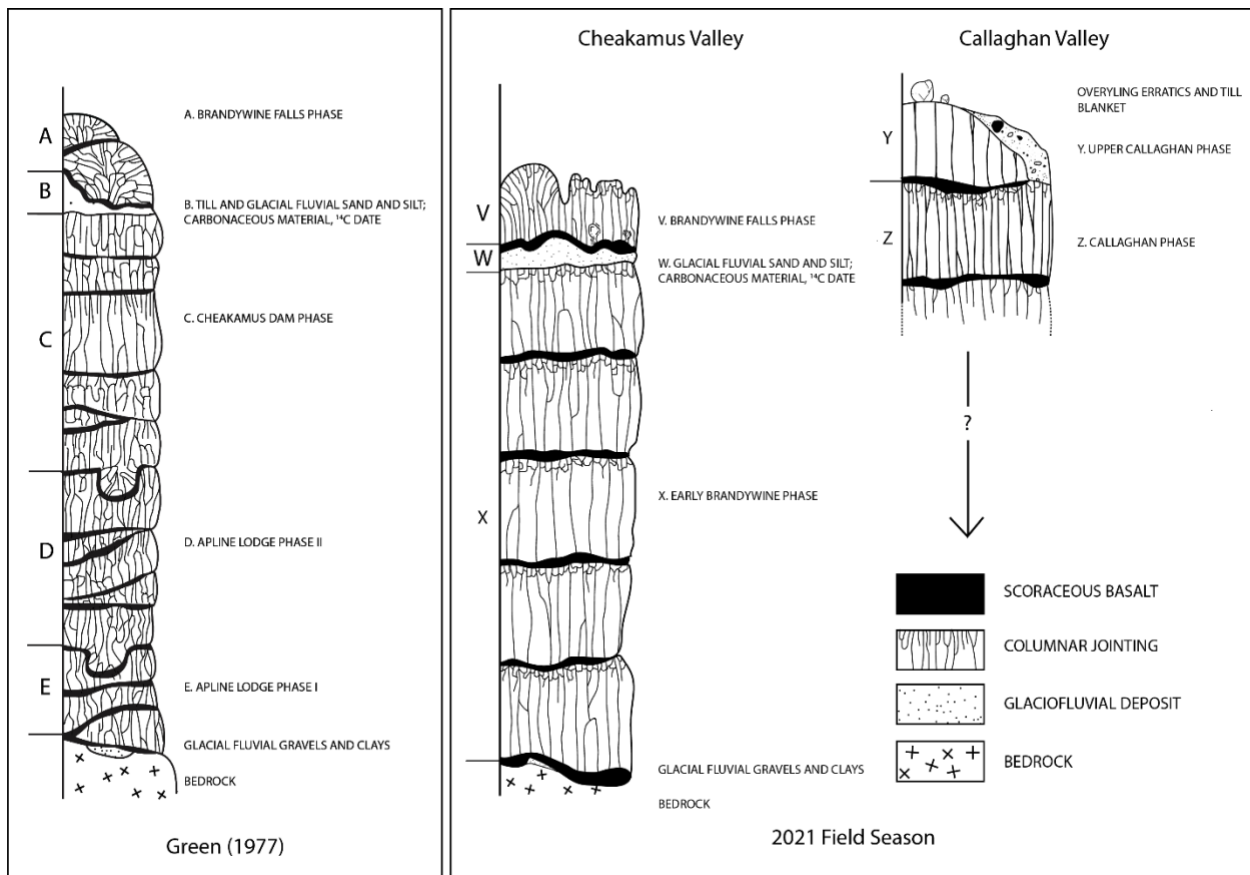


**Figure 2.** Comparison of Cheakamus basalt stratigraphy developed in the 2021 field season and Green’s 1977 stratigraphic section. Extensive till cover and lack of exposure in the Callaghan Valley did not allow for a direct correlation of lava flows between the Callaghan and Cheakamus Valleys.

Cheakamus basalt lavas are poorly exposed in the Callaghan Valley due to glacial cover which has hindered making stratigraphic correlations. Where exposed, we sampled the lavas extensively, with the goal of using geochemical and paleomagnetic information to constrain stratigraphic relationships with lavas exposed down-valley and in the Cheakamus Valley (Fig. 2). Geochemical and petrographic differences suggest two populations of lavas filling the Callaghan Valley. Plagioclase olivine basalt lavas occupy the southern part of Callaghan Valley and some outcrop exposures yield stratigraphic sections with thicknesses in excess of 45 m. On the basis of shared groundmass olivine grains, fresh olivine-plagioclase glomerophyric phenocrysts, and minor sieve-textured plagioclase xenocrysts, these lavas are comparable to Early Brandywine phase lavas. We have also mapped a plagioclase+olivine glomerophyric basaltic andesite in the northern portion of the valley surrounding Conflict Lake. These lavas are aurally restricted (Fig. 1) and may be the youngest erupted phase.

Based on our 2021 field mapping, the northern extent of the Cheakamus basalts is found at Conflict Lake and forms a broad, glaciated, valley-filling plateau of  $\geq 5$  m thickness (Fig. 3). The plateau comprises massive to coarsely jointed lava and is bounded to the south by a series of bedrock whalebacks and parallel gullies, and to the north by Conflict Lake. We propose that the vent for eruption of the Cheakamus basalts was located at Conflict Lake, although glacial erosion appears to have removed material that would define the exact vent location (i.e., scoria cone, spatter ramparts, etc.).

### ***Conflict Lake bathymetric mapping***

Previous studies did not establish the vent location for the eruptions that fed the Callaghan and Cheakamus valley-filling lavas. One plausible location for the vent was Callaghan Lake, which Green (1981) and Mathews (1958) mapped as the northernmost extent of the Cheakamus basalts. Alternatively, several proximal volcanic edifices (e.g., Slag Hill, Ring Mountain) within the Mount Cayley Volcanic Field (MCVF; Kelman et al., 2001) were considered possible sources for the Cheakamus basalts (Fig. 1). Our 2020 and 2021 field seasons tested these ideas through a mixture of field mapping, bathymetric mapping, and comparison of paleomagnetic field directions. The bathymetric profile of Callaghan Lake presents as a typical glaciated u-shaped valley, with a steep shelf of basalt that comprises the shallow southern shore (Borch et al., 2021). Additionally, the presence of Cheakamus basalts at a higher elevation in the adjacent valley, which branches from the main Callaghan Valley like a 'Y' (Fig. 1), indicates Callaghan Lake is not the source of the Cheakamus basalts. Instead, the lake, which sits just north of the 'Y' intersection, may have been formed by the damming of the drainage network as lava erupted from the adjacent branch and blocked the valley mouth during eruption. A source located within the MCVF was also ruled out through lithological and paleomagnetic comparisons between the Cheakamus basalts and the closest edifices, namely Ring Mountain, Slag Hill Tuya, and Slag Hill (Kelman, 2001). All of these edifices are andesitic in composition, have differing paleomagnetic directional means (discussed below), and have no mappable relation to the Cheakamus basalts. The basalts themselves terminate a few km east of Ring Mountain, and are not exposed anywhere past the southern shores of Conflict Lake which we interpret as the glaciated remains of the volcanic vent.

The location of the volcanic vent near Conflict Lake is partially covered by the lake itself. We mapped the bathymetry of Conflict Lake via paddleboard-mounted sonar to obtain a more complete picture of the morphology of the area (Fig. 3). The lake is shallow (<12 m deep), with marshy, gradually sloped shorelines to the east, west, and north. In contrast, the southern shoreline is steep, with almost continuous basaltic andesite outcrops which comprise the edge of the glaciated basaltic andesite plateau (Fig. 3). We interpret Conflict Lake as having formed upstream of the lava plateau via the following sequence: (a) the Cheakamus basalts erupted onto the flat bottom of the glacially-carved Callaghan Valley; (b) subsequent glaciation(s) smoothed and leveled the basalts into a plateau, but left enough relief to form a shallow longitudinal slope of the valley floor; (c) post-glaciation, the plateau caused damming of mountain streams behind it, building up Conflict Lake to a level where an outlet stream overtopped the plateau, allowing drainage to continue (Fig. 3). An alternative hypothesis is that Conflict Lake occupies a glacial scour hole; however, the difference in lithologies between upstream and downstream shorelines suggests that the volcanic plateau is responsible for its existence.

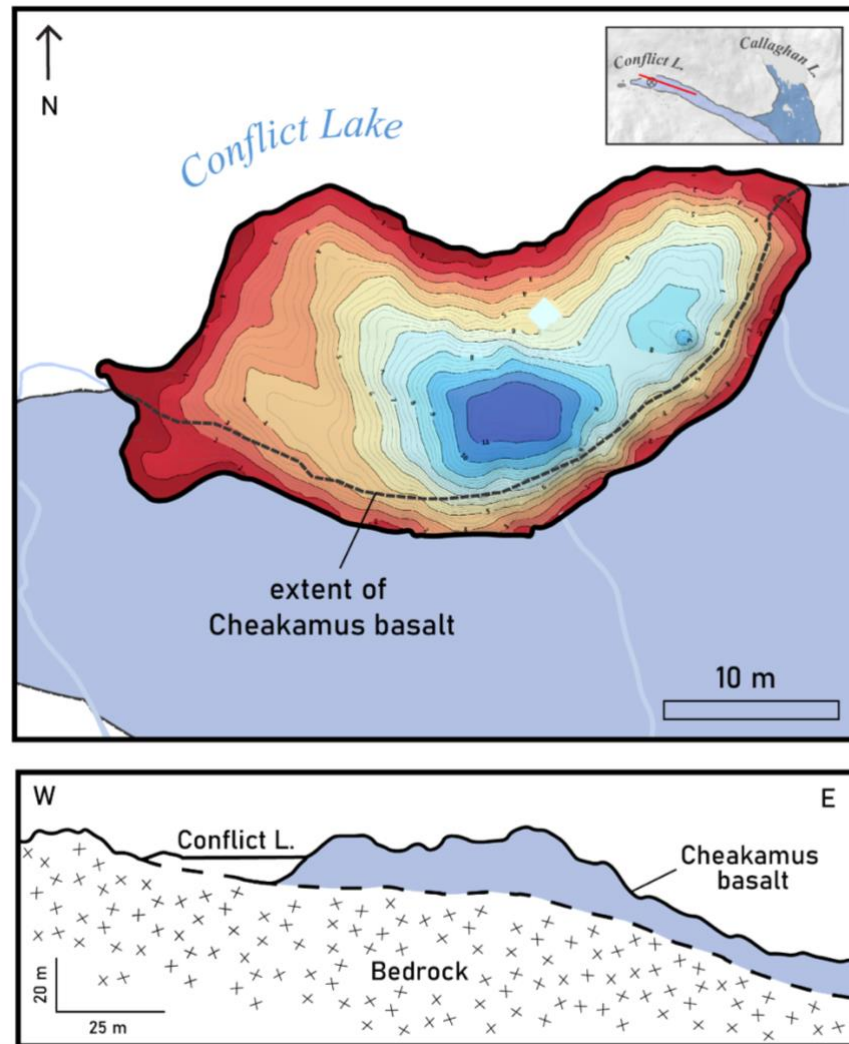


**Figure 3.** (Top) Bathymetric contour map (in m) of Conflict Lake developed from sonar data collected during the 2021 field season. Note the steep southern bank where the edge of the Cheakamus basalts

begin. (Bottom) Longitudinal cross-section of Cheakamus lava plateau at Conflict Lake, indicating lake damming and formation behind the plateau. Longitudinal profile line indicated in red on inset map in top right corner.

## Paleomagnetic Estimates of Duration of Emplacement of Cheakamus Basalt

Measurements of paleomagnetic directions recorded by volcanic rocks represent an important complement to dating volcanic sequences (Hagstrum & Champion, 2002) and estimating the duration(s) of volcanism (Hagstrum & Champion, 1994; Sherrod et al., 2006; Speranza et al., 2006, 2008, 2010; Di Chiara et al., 2012). Significant differences in paleomagnetic mean directions that exceed measurement uncertainties indicate significant time differences between eruptions. Conversely, where paleomagnetic directions between volcanic rocks (i.e., flows) are equal to or less than measurement uncertainties, volcanic eruptions can be considered as coincident in time or to have occurred within a single paleomagnetic moment (Greve et al., 2016; Williams-Jones et al., 2020).

During the 2020 field season we collected an initial sample suite consisting of 128 cores from 17 sites spanning the stratigraphic diversity of the Cheakamus basalts (Borch et al., 2021). These samples, which cover a wide geographic and stratigraphic range, suggest that the Cheakamus basalts were emplaced over a short amount of time (<2000 years; Hagstrum & Champion, 2002). In 2021, we collected an additional 290 cores to increase the number of total sites to 34. The sites span the Cheakamus Valley, Callaghan Valley, and Conflict Lake area and further test our 2020 results. They also create a more complete dataset, including sites for which we were not certain were part of the Cheakamus basalts (Table 1). We also sampled from four surrounding Mount Cayley Volcanic Field edifices to compare their paleomagnetism to the Cheakamus basalts (Table 2). All samples were drilled into volcanic lithofacies that cooled quickly, thus locking in the geomagnetic field orientation at the time of emplacement (e.g., Johnson et al., 2008). We made every effort to sample in situ outcrops and avoid areas of obvious post-emplacement rotation. Standard 2.5-cm-diameter paleomagnetic cores were drilled in the field. Approximately eight cores were taken from most sites. Each sample was oriented using a magnetic compass, and where possible a sun compass was used in conjunction with magnetic orientations.

Samples were analyzed at the paleomagnetic laboratory at the University of Lethbridge, Alberta. Magnetic susceptibility was determined with a Sapphire Instruments (SI-2B) susceptibility meter. The magnetization of each sample was measured with an AGICO JR-6A spinner magnetometer before demagnetization and again after each level of stepwise demagnetization. Samples were held in magnetic shields following field collection and between laboratory measurements. All samples were subjected to alternating field (AF) demagnetization, performed using an ASC Scientific D-2000 demagnetizer with a three-axis manual tumbler, and carried out at 10 milli-tesla (mT) steps (up to 100 mT). Thermal demagnetization was carried out at 100, 200, 300, 400, 500, 525, 550, and 580 °C, using an ASC Model TD48 dual-chamber thermal demagnetizer to confirm that alternating field demagnetization was sufficient to resolve the primary remanence. Directions of characteristic magnetization were determined for each sample by principal component analysis (Kirschvink, 1980) using Remasoft version 3.0 (Chadima and Hrouda, 2006). Mean directions of characteristic magnetization were calculated for each site and an overall mean was also calculated (Tables 1-2). All samples were subject to stepwise AF demagnetization and principal

component analysis and mean directions were calculated from the AF data only. The results of these additional data are outlined below.

### ***Paleomagnetic results for Cheakamus basalts***

A few (<10%) of the individual sites sampled during our 2020 research showed greater dispersion between cores than could be ascribed to measurement uncertainty. Generally, these situations arose where we were working with smaller or broken cores obtained from less-than-ideal outcrops, or had sampled exposures where solar compass readings were not possible, or where we sampled tilted or slumped blocks for which the tilting or slumping was not readily apparent. In 2021 we resampled these sites, where possible, and were able to reduce the “within-site” dispersion for some and locate better exposures for others. We also added new sites which represented the same eruptive phases but were from more suitable outcrops. Additionally, we sampled entire sections of exposed stratigraphy (i.e., Alexander Falls and Brandywine Falls) to fill in the gaps left by 2020 research that targeted only the lowermost and uppermost stratigraphic units. This additional sampling has now produced a total of 34 sites collected from 19 localities (some localities contain multiple flows) and has reinforced our results from the 2020 sampling (Fig. 4; Table 1). Based on the expanded dataset, the entirety of the Cheakamus basalts was emplaced over a very short span of time, essentially within a paleomagnetic moment of <2000 years (Fig. 4). This result has implications for  $^{40}\text{Ar}/^{39}\text{Ar}$  dates obtained for these very young, K-poor basalts, in that it allows us to confidently reject dates for which uncertainties do not overlap.

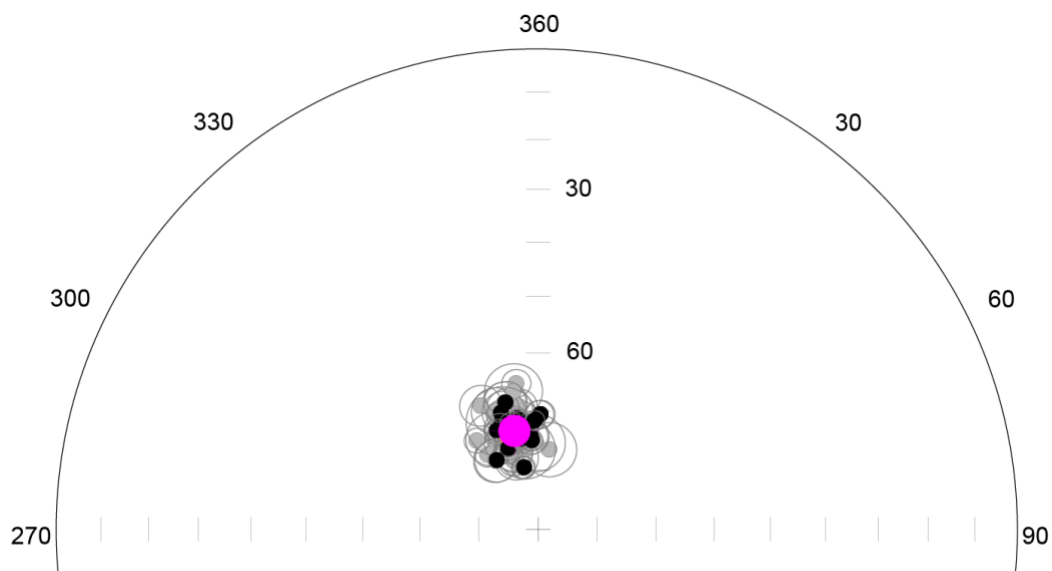


**Figure 4.** Paleomagnetic mean directions, their 95 $\alpha$  ( $p = 0.05$ ) confidence circles, and mean of all sites (pink) for the Cheakamus basalts. Grey circles represent the mean inclination and declination of each sample site ( $N = 34$ ). There are multiple sample sites for some of our sample localities (i.e., where we have sampled stacked lava flows). Given research results that argue that the Cheakamus basalts erupted in a short period of time, we have combined multiple flows at the same locality into one sample, represented

by the superimposed black circles (N = 19). Combining our data in this way results in a tighter cloud for the Cheakamus basalts. Details of directional data is provided in Tables 1 and 2.

***Paleomagnetic results for other proximal volcanic rocks***

We sampled volcanic edifices within the Mount Cayley Volcanic Field that are proximal to the Cheakamus basalts to rule out any volcanological connections (Fig. 5). We are able to reject any genetic relationship between the three most proximal volcanic edifices and the Cheakamus basalts on the basis of: a) the mapped distributions of the associated volcanic deposits; and b) pronounced differences in petrographic character and geochemical compositions. Our 2021 paleomagnetic results serve as a further test of these potential connections, and a preliminary inquiry into the timing of proximal volcanic edifices (Table 2). Our sample suite includes cores (N=8) from the top of Ring Mountain, from the top of Slag Hill Tuya (N=8), and from three different sites at Slag Hill (N=23) (Fig. 1). Most of these sampling sites show a marked difference in paleomagnetic mean direction from that obtained for the Cheakamus basalt (Fig. 5). Samples from the lower emplacement units of Slag Hill and a satellite flow of Ring Mountain do overlap the Cheakamus cloud, suggesting that parts of these eruptions occurred within a short period of time (i.e., <2000 years) and providing an interesting future opportunity to compare eruption histories and paleoenvironmental conditions between the edifices. However, a more complete paleomagnetic dataset for the MCVF would be required to do so.

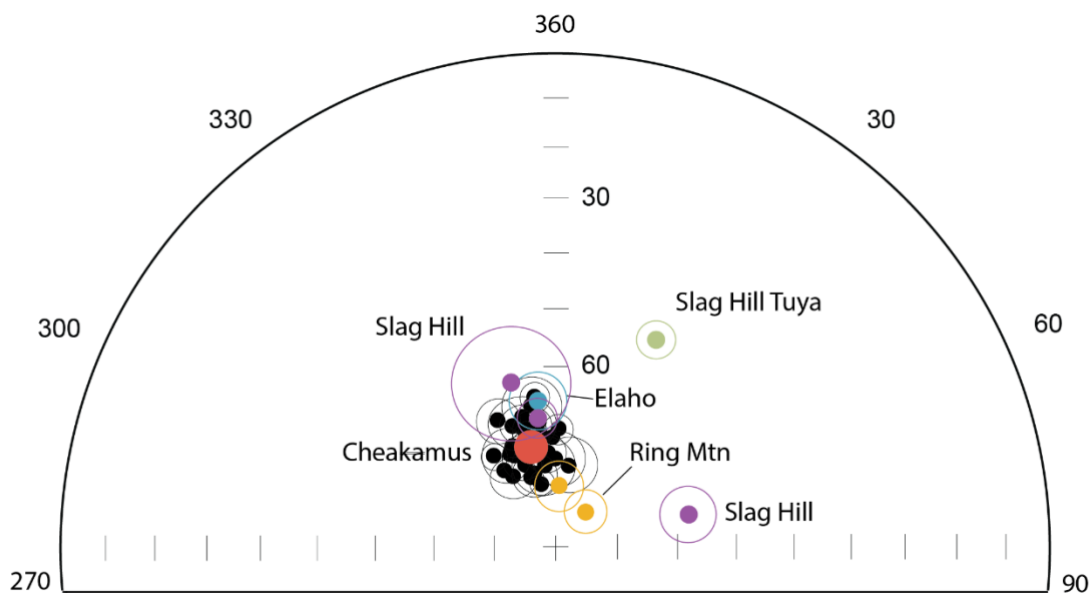


**Figure 5.** Paleomagnetic mean directions for 34 Cheakamus basalt sites (black circles) and their 95 $\alpha$  ( $p = 0.05$ ) confidence circles, and mean of all sites (red). Individual sites fall within the 95% confidence interval of the mean, suggesting that the Cheakamus basalts were emplaced over a short period of time (<2000 years). Paleomagnetic mean direction and confidence circle for the Elaho basalt site (blue) overlaps error circle for the Cheakamus basalt mean. Given that its direction is not significantly different, it likely erupted at the same time as the Cheakamus basalt. The proximal volcanic edifices of Slag Hill Tuya (green), and

some sample sites from Ring Mountain (yellow) and Slag Hill (purple) have different paleomagnetic mean directions and were therefore not erupted at the time of the Cheakamus basalts. The stratigraphically older samples from Slag Hill have some overlap with the Cheakamus basalts, as does Ring Mountain NW, suggesting that these eruptions could have occurred at or near the same time as the Cheakamus basalts. Details of directional data is provided in Tables 1 and 2.

Samples collected from a basalt flow in the Elaho Valley falls within error (95% circle of confidence) for the Cheakamus basalt mean (Fig. 5). The Elaho basalts are a voluminous set of valley-filling basalts situated southwest of the Mount Meager Complex. They have striking, if superficial, similarities to the Cheakamus basalts (Wilson & Russell, 2018) in that they are voluminous, olivine-phyric basalts and subaerially emplaced. Furthermore, the two groups of basaltic lavas are only ~40 km apart, separated to the NW-SE by the Squamish River Valley. Research on the Elaho is preliminary, with only one site sampled for paleomagnetic data. More data, including extensive mapping and increased paleomagnetic and  $^{40}\text{Ar}/^{39}\text{Ar}$  sampling is required to better understand the temporal and genetic relationship between these two voluminous suites of basaltic lavas.

## Radiometric Estimates of Absolute Age

The current published estimates of age for the Cheakamus basalts are sparse and have high uncertainties. The two published radiometric age estimates include: a) a single K/Ar age of  $50 \text{ ka} \pm 50 \text{ ka}$  for a sample of basalt lava located 1 km north of the Chance Creek FSR turnoff (previously referred to as Garibaldi Station; Green et al., 1988); and b) a single  $^{14}\text{C}$  date of  $34,200 \text{ ka} \pm 800 \text{ ka}$  from organic material recovered from the sedimentary horizon underlying the Brandywine Falls phase lavas, situated 0.5 km north of the Callaghan Valley FSR turnoff and exposed along Highway 99 (Green, 1981; McNeely, 1989). The published  $^{14}\text{C}$  age is based on a sample comprised of material of uncertain origin with low amounts of  $^{14}\text{C}$  (McNeely, 1989). These age determinations allow for volcanic eruption(s) contemporaneous with the Fraser Glaciation (25-10 ka, Clague & Ward, 2011; Lian et al., 2001) or Recent (i.e., < 10 ka) or as old as 100 ka coinciding with the Olympia non-glacial interval (Clague, Armstrong & Mathews, 1980; Clague, 1981; Clague & Ward, 2011). Our 2020  $^{40}\text{Ar}/^{39}\text{Ar}$  date obtained from the base of the Cheakamus basalts at Brandywine Falls gives an age is  $23.9 \pm 15.7 \text{ Ka}$  (Borch et al., 2021) and overlaps the  $^{14}\text{C}$  age estimate reported by Green (1981).

**Table 1.** Paleomagnetic directions and sample locations for the Cheakamus basalts. NC/NU = number of samples collected/used, D = declination, I = inclination,  $\alpha_{95}$  (P=0.05), radius of 95% circle of confidence,  $k$  = precision parameter, P = polarity, \* mean of multiple flows sampled at locality. See Figure 1 for sampling localities. G.A.D. (Geocentric Axial Dipole Field) inclination = 67.02°. P.E.F. (Present Earth's Field) at mean sampling location: inclination = 70.3°, declination = 16° easterly.

Locality	Latitude/ Longitude	Site No.	Sample Nos.	NC	NU	D (°)	I (°)	$\alpha_{95}$ (°)	k	P
Garibaldi Railway Station										
Cut: 3 flows										
Flow 1	49.973648/-123.149325	1	CBB011-018	8	7	346.9	69.3	3.9	235.2	N
Flow 2	49.973601/-123.149141	9	CBB901-908	8	8	350.8	71.3	3.4	260.4	N
Flow 3	49.973601/-123.149141	10	CBB101-108	8	8	350	71.8	2	736.9	N
		<i>*mean,</i>								
<i>Garibaldi Railway Station</i>		<i>sites 1,9,</i>								
<i>Cut</i>		<i>10</i>		24	23	349.5	70.9	1.6	345	N
McGuire FSR: 2 flows										
Flow 1	50.000234/-123.132984	11	CBB111-118	8	8	326.7	74.8	2	838	N
Flow 2	50.000234/-123.132984	12	CBB121-128	8	7	341.7	75	3.6	273.3	N
		<i>*mean,</i>								
<i>McGuire FSR</i>		<i>sites 11,</i>								
		<i>12</i>		16	15	334.2	75.3	1.8	477.7	N
Cal-Cheak FSR Gravel										
Quarry										
West facing BC Rail Quarry										
Cliff: 4 flows										
Flow 1	50.069716/-123.094314	22	CBB221-228	8	8	355.6	72.1	2.9	367.7	N
Flow 2	50.069716/-123.094314	5	CBB501-513	13	10	341.3	77.7	2.6	345.7	N
Flow 3	50.069716/-123.094314	7	CBB701-708	8	7	343	76.8	3	398.3	N
Flow 4	50.069344/-123.09364	6	CBB601-608	8	7	352	64.9	2.4	617.1	N
		<i>*mean,</i>								
<i>West facing BC Rail Quarry</i>		<i>sites 5-</i>								
<i>Cliff</i>		<i>7,22</i>		37	32	345.9	71.7	2.1	145	N

Sugarcube Hill, BC Rail Q. Flow 1	50.070636/-123.092869	37	CBB371-377	7	7	323.7	77.5	8.3	66	N
Sugarcube Hill, BC Rail Q. Flow 2	50.070636/-123.092869	36	CBB361-368	9	9	350.4	66.2	4.8	117	N
<i>Sugarcube Hill</i>		<i>*mean, sites 36,37</i>		<i>16</i>	<i>16</i>	<i>341.4</i>	<i>70.8</i>	<i>6</i>	<i>38.2</i>	<i>N</i>
McGuire Rd. Transfer Stn. (glac.)	50.061335/-123.112999	4	CBB401-408	8	8	339.9	75.5	2	758.3	N
South Callaghan Valley uppermost flow (glac.)	50.071166/-123.109156	8	CBB801-808	8	6	355.4	74.2	3.1	467.2	N
Lucille Lake: Uppermost flow (glac.)	49.98629/-123.144838	13	CBB131-138	8	8	352.7	72.8	2.4	545	N
Lucille Lake: Lowermost flow	49.986693/-123.144584	14	CBB141-148	8	8	352.1	76.3	5	121.4	N
<i>Lucille Lake flows</i>		<i>*mean, sites 13,14</i>		<i>16</i>	<i>16</i>	<i>350</i>	<i>74.5</i>	<i>2.4</i>	<i>222</i>	<i>N</i>
Upper Callaghan Rd. flow (glac.)	50.128865/-123.126047	15	CBB151-158	8	8	337.4	71.9	1.9	858.2	N
Dority & Callaghan Ck. confluence	50.127408/-123.131499	16	CBB161-168	8	8	1.3	70.5	2.4	549.1	N
Shadow Lake: High Standing Basalt (southernmost)	49.975628/-123.152969	17	CBB171-178	8	8	356.1	74.9	1.8	950.4	N
Shadow Lake: High Standing Basalt (horizontal columns)	49.984868/-123.146591	18	CBB181-188	8	8	349.9	71.8	2	761.9	N
Daisy L. Highway Roadcut: uppermost flow (glac.)	49.97812/-123.1442563	19	CBB191-198	8	6	359.5	75.3	4.9	186.4	N
Daisy L. Highway Roadcut: lowermost flow	49.97812/-123.1442573	21	CBB211-218	8	7	334.4	73	4	173.1	N

<i>Daisy L. Highway Roadcut flows</i>		<i>*mean, sites 19,21</i>		16	13	344.7	73.4	2.9	192	N
Callaghan V. Rd./Highway 99 Intersection (glac.)	50.06384/-123.10875	23	CBB231-238	8	8	329.2	76.4	3.7	230.5	N
Widel Outcrop: 3 flows										
Flow 1	50.07317/-123.0922	24	CBB241-248	8	8	335.6	66.9	3.5	246.3	N
Flow 2	50.07317/-123.0922	25	CBB251-258	8	6	340.7	68.7	4	277.4	N
Flow 3	50.07317/-123.0922	26	CBB261-268	8	8	344.9	72.9	3	332.2	N
<i>Widel Outcrop flows</i>		<i>*mean, sites 24-26</i>		24	22	342.3	69.3	2.2	177	N
Early Brandywine Phase: Second uppermost flow	50.03425/-123.1144	27	CBB271-2710	10	10	344.3	69.3	3.6	183.1	N
Early Brandywine Phase: Uppermost flow	50.034439/-123.116988	28	CBB281-2813	13	13	339	74.2	3.2	168.4	N
Early Brandywine Phase: lowermost flow	50.03504/-123.12069	29	CBB291-299	9	9	344	77.4	3.7	197.6	N
Glaciated Brandywine Phase (Brandywine Park)	50.03855/-123.12038	31	CBB311-318	8	8	340.5	75.6	2.4	528.6	N
<i>Brandywine Falls flows</i>		<i>*mean, sites 27-31</i>		40	40	342.5	73.4	1.9	139	N
Alexander Falls: second uppermost flow	50.12762/-123.12863	32	CBB321-3210	10	10	326	71.8	2.1	518.8	N
Alexander Falls: lowermost flow	50.134693/-123.128573	34	CBB341-348	8	6	347.4	71.4	2.8	566.5	N
<i>Alexander Falls flows</i>		<i>*mean, sites 32,34</i>		18	16	339	71.9	2.7	161	N
Callaghan Valley Real Life Trail	50.151252/-123.158504	33	CBB331-339	9	7	358.2	71.6	1.7	1240	N

Callaghan Lake	50.19175/-123.1829293	35	CBB351-358	8	7	347.3	79.3	1.9	982	N
<b>Mean, all sampling sites (N=34)</b>						<b>345.2</b>	<b>73</b>	<b>1.3</b>	<b>319.2</b>	<b>N</b>
<i>Mean, all sampling localities (N=19)</i>						<i>346.6</i>	<i>72.9</i>	<i>1.5</i>	<i>536</i>	<b>N</b>
<b>Mean, all samples (N=269)</b>						<b>345.3</b>	<b>72.8</b>	<b>0.6</b>	<b>198.7</b>	<b>N</b>

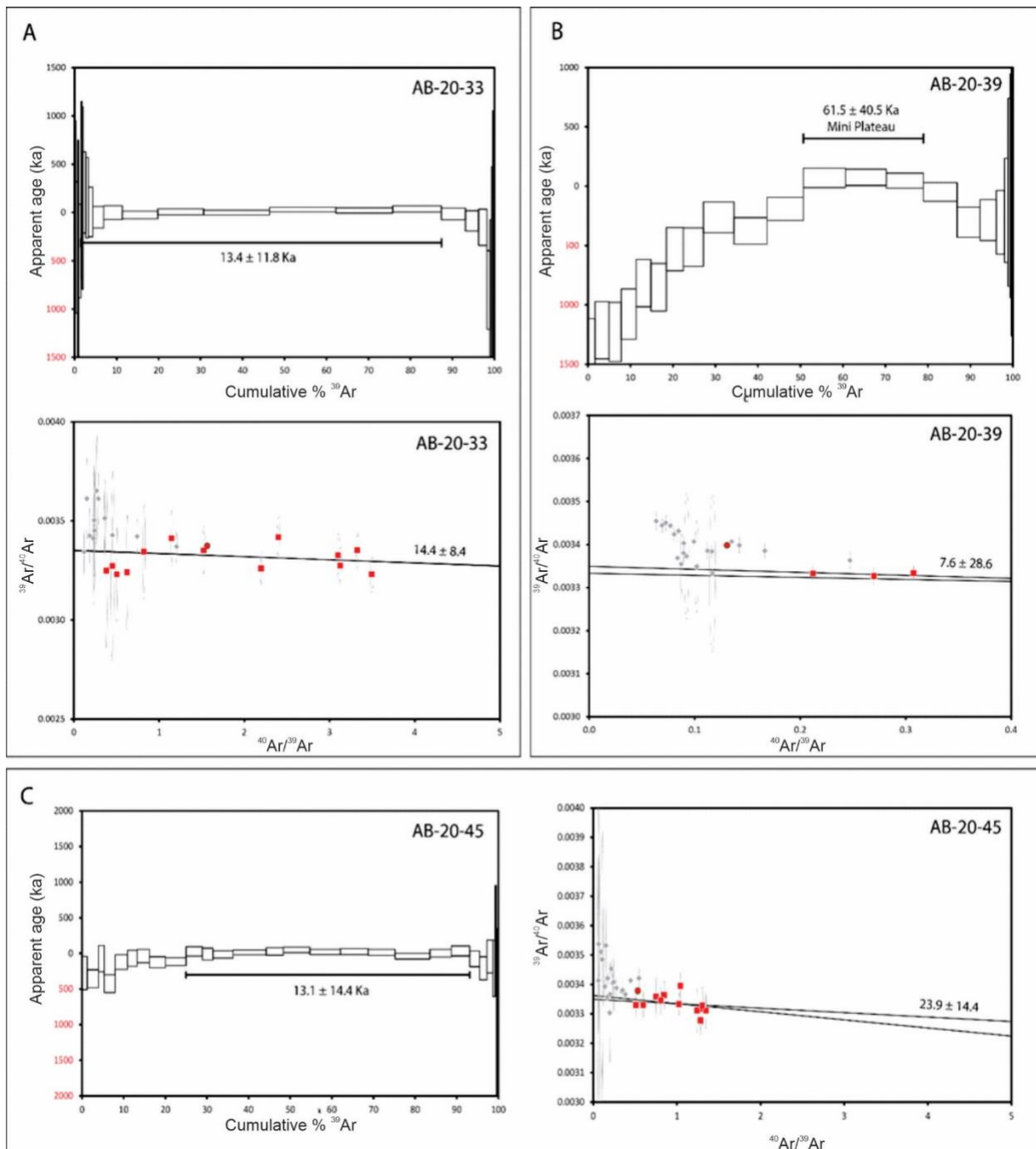


**Figure 6.**  $^{40}\text{Ar}/^{39}\text{Ar}$  geochronometry for samples (a) AB-20-33, (b) AB-20-39, and (c) AB-20-45. (Top) Plateau diagram based on analysis of groundmass material; height of individual boxes equals  $2\sigma$  errors. (Bottom) Inverse isochron plot showing all heating steps. Ellipses denote  $2\sigma$  uncertainties.

We collected material from key stratigraphic localities for  $^{40}\text{Ar}/^{39}\text{Ar}$  dating of the Cheakamus basalt lavas with the goal of better establishing the age and duration of volcanism. We sampled locations at the base

and top of well-exposed, thick stratigraphic sections (Brandywine Falls and Alexander Falls; Fig. 2) to constrain maximum and minimum eruptive ages. We collected sample AB-20-33 from the lowest exposed flow in the valley below Alexander Falls, which represents the earliest stage of eruption in the Callaghan Valley. This sample returned an inverse isochron date of  $14.4 \pm 8.4$  ka (Fig. 6a). Sample AB-20-45 was collected from the stratigraphically highest unit in the Cheakamus Valley, the Brandywine Falls phase glaciated plateau that comprises most of the valley floor to the north of Brandywine Falls. This sample returned an inverse isochron date of  $23.9 \pm 14.4$  ka (Fig. 6b), which compares favorably to the sample dated at the base of this exposure (Borch et al., 2021). Sample AB-20-39, from the stratigraphically highest lava at Callaghan Lake returned a plateau age of  $61.5 \pm 40.5$  ka (Fig. 6c).

The young age of the Cheakamus basalts combined with their low potassium content produces radiometric age determinations that have characteristically high uncertainties; in our case, 58-66%. However, our  $^{40}\text{Ar}/^{39}\text{Ar}$  results are internally consistent and allow for either a limited protracted period of volcanism <100 ka or, potentially, a single eruptive age of  $19.2 \pm 6.5$  ka based on weighted mean calculation, accounting for unequal variance.

## Discussion

Field mapping,  $^{40}\text{Ar}/^{39}\text{Ar}$  dating and paleomagnetic study allow us to infer the age of volcanism, its duration, and its relation to the Fraser Glaciation. Because of the limits on the precision of  $^{40}\text{Ar}/^{39}\text{Ar}$  results, we interpret  $^{40}\text{Ar}/^{39}\text{Ar}$  results in the context of our paleomagnetic data, which restricts eruptive duration to <2000 years. If we accept the weighted mean age of 19.2 ka, this restricted time period likely places volcanism between ~17-22 ka, with a minimum of 12.7 ka and a maximum of 25.7 ka.

Mapping the surfaces of the stratigraphically highest basalt lavas reveal glacial-striae and chatter marks, as well as erratics of crystalline bedrock. These observations strongly suggest that the youngest lavas predate the latest glacial advance within the Cheakamus River and Callaghan Creek valleys. The best estimates for the onset, peak, and waning of the Fraser Glaciation are ~ 25 ka, ~15, and ~10 ka BP, respectively (Clague & Ward, 2011), with periods of rapid glacial retreat during the Port Moody Interstade (~23-21 ka), followed by readvance at ~19-18 ka and another retreat at ~13-12 ka (Everson Interstade; Booth et al., 2003). Thus, we have very good correspondence between the radiometric age estimates and the field constraints.  $^{40}\text{Ar}/^{39}\text{Ar}$  age determinations (within uncertainty) show Cheakamus volcanism to predate or overlap with the onset of Fraser Glaciation, and the field data also indicate emplacement of the Cheakamus basalts in a subaerial environment prior to peak Fraser Glaciation (i.e., >15 ka). These field observations suggest a minimum age closer to peak glaciation, as opposed to the 12.7 ka minimum suggested purely by the  $^{40}\text{Ar}/^{39}\text{Ar}$  data.

In summary, we propose the following sequence of events and dates: a) onset of Fraser Glaciation at ~25 ka; b) emplacement of Cheakamus basalts into ice-free or ice-marginal Callaghan and Cheakamus valleys, likely pre- or syn-Port Moody Interstade at ~17-22 ka, with possible abrupt spatial changes in ice cover and emplacement environment; c) full occupation of valleys by glacial ice (likely Vashon Stade), polishing and striating the surface of the Cheakamus basalts, and; d) final glacial retreat post 10 ka.

**Table 2.** Paleomagnetic directions and sample locations for the Elaho basalts, Slag Hill and Tuya, and Ring Mountain volcanic edifices. NC/NU = number of samples collected/used, D = declination, I = inclination,  $\alpha_{95}$  (P=0.05), radius of 95% circle of confidence,  $k$  = precision parameter, P = polarity, \* mean of multiple flows sampled at locality. See Fig. 1 for sampling localities. G.A.D. (Geocentric Axial Dipole Field) inclination = 67.02°. P.E.F. (Present Earth's Field) at mean sampling location: inclination = 70.3°, declination = 16° easterly.

Locality	Latitude/Longitude	Site No.	Sample Nos.	NC	NU	D (°)	I (°)	$\alpha_{95}$ (°)	k	P
Elaho Basalts (North)	50.53908/-123.60983	ELB01	ELB011-016	9	9	353	65.5	4.7	122	N
Ring Mountain	50.22049/-123.29913	MCV01	MCV011-019	9	8	37.5	82.1	3.5	248	N
Slag Hill West (4)	50.18603/-123.30712	MCV02	MCV020-027	10	7	76.1	67.4	4.6	171	N
Slag Hill Tuya	50.20207/-123.28018	MCV05	MCV051-058	9	7	25.7	51.4	3	385	N

## Summary

Detailed mapping and stratigraphic work undertaken in the 2021 field season expanded on the work of Mathews (1948) and Green (1977, 1981, 1988) by updating and extending the stratigraphy and emplacement units (Fig. 2), locating the source vent (Fig. 1), and constraining both age and duration of eruption (Figs. 4-6). The significant increase in samples dated by  $^{40}\text{Ar}/^{39}\text{Ar}$  carried out in 2021 encompasses the entire stratigraphic succession, improves the dispersion of multiple sample sites, and sets a maximum range in age(s) of 6.0-102 ka, with a weighted average of  $19.2 \pm 6.5$  ka. The extensive paleomagnetic work tests the original premise that the basalts were erupted over a short timespan and confirms that the Cheakamus basalts were erupted within one paleomagnetic moment of <2000 years. Field mapping has constrained the location of the eruption source (i.e., vent) to near modern-day Conflict Lake. This new constraint on duration allows for better interpretation of  $^{40}\text{Ar}/^{39}\text{Ar}$  dates, which, along with mapping of glacial surfaces, indicate the basalts erupted pre-Fraser Glaciation, likely between ~17 and 22 Ka. Future work will focus on the Cheakamus basalts as a recorder of paleoenvironment, using continued surface and sediment mapping to understand their syn- and post-glacial history, and their glacial and hydrological interaction and role in landscape evolution. A more complete understanding of the distribution, volume, eruptive duration, and age of the Cheakamus basalts will help clarify their feasibility as a potential future geothermal energy source.

## Acknowledgments

Many thanks to Dr. Randy Enkin (Geological Survey of Canada) for his instruction in field sampling provided to students and the loan of sampling equipment; and to S. Leiter, M. Harris, K. Landoni, Dr. L. Anthony, and M. Wen for their assistance in the field.

## References

- Booth, D., Goetz Troost, K., Clague, J.J., & Waitt, R.B., 2003, The Cordilleran Ice Sheet, Development in Quaternary Science, v. 1, p. 17-43.
- Borch, A., Russell, J.K., Barendregt, R., Quane, S.L. & Wilson, A., 2021, Distribution and Age of the Cheakamus Basalts, Garibaldi Volcanic Belt, British Columbia. Geosciences BC Report 2021-08, 254-265.
- Chadima, M., Hrouda, F., 2006. Remasoft 3.0 – a user-friendly paleomagnetic data browser and analyzer. *Travaux Geophysiques*, XXVII, 20-21.
- Clague, J.J., Armstrong, J.E., Mathews, W.H., 1980, Advance of the late Wisconsinan Cordilleran ice sheet in southern British Columbia since 22,000 yr BP. *Quaternary Research*, v. 13, p. 322–326.
- Clague, J.J., 1981, Late Quaternary geology and geochronology of British Columbia, Part 2: summary and discussion of radiocarbon-dated Quaternary history. Geological Survey of Canada, Paper 80-35.
- Clague, J.J., and Ward, B.C., 2011, Pleistocene Glaciation of British Columbia. *Developments in Quaternary Science*, v. 15, p. 563–573.
- Cui, Y., Miller, D., Schiarizza, P., and Diakow, L.J., 2017, British Columbia digital geology. British Columbia Ministry of Energy, Mines and Petroleum Resources, British Columbia Geological Survey Open File 2017-8, 9p.
- Di Chiara, A., Speranza, F., and Porreca, M., 2012, Paleomagnetic secular variation at the Azores during the last 3 ka: *Journal of Geophysics*, Res.117 B07101, doi:10.1029/2012JB009285
- Huppert, H.E., and Woods, A.W., 2002, The role of volatiles in magma chamber dynamics: *Nature*, v. 420, p. 493–495, <https://doi.org/10.1038/nature01211>.
- Jessop, A., 2008, Review of National Geothermal Energy Program, Phase 2 – geothermal potential of the Cordillera: Geological Survey of Canada, Open File 5906, p. 86, <https://doi.org/10.4095/225917>
- Kelman, M.C., Russell, J.K., and Hickson, C.J., 2001, Preliminary petrography and chemistry of the Mount Cayley volcanic field, British Columbia: Geological Survey of Canada, Current Research 2001-A11, p. 9
- Kirschvink, J.L., 1980, The least-squares line and plane analysis of palaeomagnetic data: *Geophysics Journal of Research, Astronomical Society*, v 62, p. 699-718.
- Grasby, S.E., Allen, D.M., Bell, S., Chen, Z., Ferguson, G., Jessop, A., Kelman, M., Ko, M., Majorowicz, J., Moore, M., Raymond, J. and Therrien, R., 2011, Geothermal energy resource potential of Canada: Geological Survey of Canada ,Open File 6914, p. 322, <https://doi.org/10.4095/288745>.
- Grasby, S.E., Ansari, S.M., Calahorrano-Di Patre, A., Chen, Z., Craven, J.A., Dettmer, J., Gilbert, H., Hanneson, C., Harris, M., Liu, J., Muhammad, M., Russell, K., Salvage, R.O. Savard, G. Tschirhart, V., Unsworth, M.J., Vigouroux-Caillibot, N. and Williams-Jones, G., 2020, Geothermal resource potential of the Garibaldi volcanic belt, southwestern British Columbia (part of NTS 092J): GeoscienceBC Summary of Activities 2019: Energy and Water, Geoscience BC, Report 2020-02, p. 103–108.
- Green, N.L., 1977. Multistage andesite genesis in the Garibaldi Lake area, southwestern British Columbia: University of British Columbia, p. 1–256.
- Grasby, S.E., Ansari, S.M., Barendregt, R.W., Borch, A., Calahorrano-DiPatre, A., Chen, Z., Craven, J.A., Dettmer, J., Gilbert, H., Hanneson, C., Harris, M., Hormozzade, F., Leiter, S., Liu, J., Muhammad, M., Quane, S.L., Russell, J.K., Salvage, R.O., Savard, G., Tschirhart, V., Unsworth, M.J., Vigouroux-Caillibot, N., Williams Jones, G., Williamson, A., and Vestrum, Z.E., 2021, Geothermal resource

- potential of the Garibaldi volcanic belt, southwestern British Columbia (part of NTS 092J): GeoscienceBC Summary of Activities 2020: Energy and Water, Geoscience BC, Report 2021-08.
- Green, N.L., 1977, Multistage andesite genesis in the Garibaldi Lake area, southwestern British Columbia [Ph.D. thesis]: Vancouver, British Columbia, Canada, University of British Columbia.
- Green, N.L., 1981, Geology and petrology of the Quaternary volcanic rocks, Garibaldi Lake area, southwestern British Columbia: Geological Society of America Bulletin, v. 92, p. 1359–1470.
- Green, N.L., Harakal, J.E., Souther, I.J.G., and Read, P.B., 1988, Eruptive history and K-Ar geochronology of the late Cenozoic Garibaldi volcanic belt, southwestern British Columbia: Geological Society of America Bulletin, v. 100, p. 563–579.
- Green, N.L., 1990, Late Cenozoic volcanism in the Mount Garibaldi and Garibaldi Lake areas, Garibaldi volcanic belt, southwestern British Columbia: Journal of the Geological Association of Canada, v. 17, p. 171-175.
- Greve, A., Turner, G.M., Conway, C.E., Townsend, D.B., Gamble, J.A., Leonard, G.S., 2016, Palaeomagnetic refinement of the eruption ages of Holocene lava flows, and implications for the eruptive history of the Tongariro Volcanic Centre, New Zealand: Geophysical Journal International, v. 207, p. 702–718, <https://doi.org/10.1093/gji/ggw296>.
- Hagstrum, J.T., and Champion, D.E., 2002, A Holocene paleosecular variation record from 14C-dated volcanic rocks in western North America. Journal of Geophysical Research: Solid Earth, **107**(B1): 2025. doi:10.1029/2001JB000524.
- Hagstrum, J.T., and Champion, D.E., 1994, Paleomagnetic correlation of Late Quaternary lava flows in the lower east rift zone of Kilauea Volcano, Hawaii Journal of Geophysics, Res. 99 B11 21 47921 690.
- Johnson, C.L., 2008, Recent investigations of the 0-5 Ma geomagnetic field recorded by lava flows. Geochemistry, Geophysics, Geosystems, v. 9, Q04030, doi: 10.1029/2007GC001719.
- Kirschvink, J.L. (1980) The Least Squares Line and Plane Analysis of Palaeomagnetic Data. Geophysical Journal International, 62, 699-718. <http://dx.doi.org/10.1111/j.1365-246X.1980.tb02601.x>
- Lian, O., and Mathewes, R.W., 2001, Palaeoenvironmental reconstruction of the Port Moody Interstade, a nonglacial interval in southwestern British Columbia at about 18000 14C years BP: Canadian Journal of Earth Sciences, v. 38 p. 943-952.
- Mathews, W.H., 1948, Geology of the Mount Garibaldi Map-Area, Southwestern British Columbia [Ph.D. thesis]: Berkeley, University of California, Berkeley.
- Mathews, W.H., 1958, Geology of the Mount Garibaldi map area, southwestern British Columbia, Canada. Part II: Geomorphology and Quaternary Volcanic Rocks: Geological Society of America Bulletin, v. 69, p. 179–196.
- McNeely, R., 1989, Geological Survey of Canada radiocarbon dates XXVIII: Geological Survey of Canada Paper 88-7, p. 44, <https://emrlibrary.gov.yk.ca/gsc/papers/88-7.pdf>.
- Souther, J.G., 1980, Geothermal reconnaissance in the central Garibaldi Belt, British Columbia: in Current Research, Part A: Geological Survey of Canada, Paper 80-1A, p. 1–11.
- Sherrod, D.R., Hagstrum, J.T., McGeehin, J.P., Champion, D.E., and Trusdell, F.A., 2006, Distribution, <sup>14</sup>C chronology, and paleomagnetism of latest Pleistocene and Holocene lava flows at Haleakalā volcano, Island of Maui, Hawai'i: a revision of lava flow hazard zones: Journal of Geophysics, Res. 111 B5 B05205 doi:10.1029/2005JB003876.

- Speranza, F., Branca, S., Coltelli, M., Caracciolo, F.D.A, and Vigliotti, L, 2006, How accurate is 'paleomagnetic dating'? New evidence from historical lavas from Mount Etna: *Journal of Geophysics, Res* 111 B12S33 doi:10.1029/2006JB004496.
- Speranza, F., Pompilio, M., D'Ajello Caracciolo, F., and Sagnotti, L., 2008, Holocene eruptive history of the Stromboli volcano: constraints from paleomagnetic dating: *Journal of Geophysics, Res* 113 B9 doi:10.1029/2007JB005139.
- Speranza, F., Landi, P., D'Ajello Caracciolo, F., and Pignatelli, A., 2010, Paleomagnetic dating of the most recent silicic eruptive activity at Pantelleria (Strait of Sicily): *Bulletin of Volcanology*, v. 72 p. 874-858.
- Townsend, M., and Huber, C., 2020, A critical magma chamber size for volcanic eruptions: *Geology*, v. 48, p. 431–435, <https://doi.org/10.1130/G47045.1>.
- Williams-Jones, G., Barendregt, R.W., Russell, J.K., Le Moigne, Y., Enkin, R.J., and Gallo, R., 2020, The age of the Tseax volcanic eruption, British Columbia, Canada: *Canadian Journal of Earth Sciences*, v. 57, <https://cdnsiencepub.com/doi/10.1139/cjes-2019-0240>.
- Wilson, A.M., and Russell, J.K., 2018, Quaternary glaciovolcanism in the Canadian Cascade volcanic arc—Paleoenvironmental implications, in Poland, M., Garcia, M., Camp, V., and Grunder, A., eds., *Field Volcanology: A Tribute to the Distinguished Career of Don Swanson: Geological Society of America Special Paper 538*, p. 1–XXX, [https://doi.org/10.1130/2018.2538\(06\)](https://doi.org/10.1130/2018.2538(06)).
- Witter, J., 2019, South Meager geothermal project – new perspectives from recently unearthed data: *Geoscience BC, Report 2019-07*, p. 5, <http://www.geosciencebc.com/i/pdf/Report-2019-07-Innovate-Geothermal.pdf>.

# Chapter 4 – Gravity Survey at Mount Meager and Mount Cayley Volcanic Complexes: Summer 2021

Calahorrano-Di Patre, A., Williams-Jones, G.

Physical Volcanology Group, Centre for Natural Hazards Research  
Department of Earth Sciences  
Simon Fraser University, Burnaby BC

## Introduction

Gravity data is routinely used as a valuable tool for monitoring natural hazards as well as for underground resource exploration (Domra Kana et al., 2015; Miller et al., 2018). It is uniquely capable of detecting and characterizing subsurface mass change through the detection of density changes below the ground (MacQueen et al., 2016; Zurek et al., 2015). Bouguer gravity surveys aim to map density changes through the detection of gravity anomalies in comparison with the theoretical gravity at a certain site. They have been deployed in the context of geothermal projects as a non-invasive way to determine the size and shape of a geothermal reservoir, as well as to identify geological structures that may not have been detected through other geophysical methods (Domra Kana et al., 2015).

In 2019 and 2020, gravity measurements were performed in the Mount Meager Volcanic Complex, BC, in order to better understand the density changes associated with the South Meager Geothermal Project. This work was undertaken to characterize possible hazardous areas, and to determine the potential for geothermal exploration in other parts of this volcanic complex (Grasby et al., 2021). The results of these surveys were described in the Geological Survey of Canada Open File 8732 (Grasby et al., 2020) and the Garibaldi Geothermal Energy Project - Phase 1 Final Report for Geoscience BC (Grasby et al., 2021). A Bouguer anomaly map was presented in the [Phase 1 Geoscience BC Final Report](#) using data surveyed at 113 sites throughout the volcanic complex. This Bouguer anomaly map showed a negative gravity anomaly in the South Meager Geothermal Project area, a very large negative anomaly on the northern flanks of the Mount Meager Volcanic Complex, and a large positive anomaly south of the volcanic complex. Since the survey was designed to enable higher resolution closer to areas of interest (e.g., the South Meager Geothermal Project), the grid density of surveyed stations was much lower farther away from the Meager Massif. However, because of the interesting results presented in the two earlier reports, it was decided that additional sites would be surveyed in the south and north areas where the anomalies were detected, in order to further constrain the anomaly areas and their causes.

In contrast, despite the known geothermal potential of the Mount Cayley Volcanic Complex, there have been fewer geophysical studies done in this area in comparison with Mount Meager (Jessop, 2008). Additionally, the Mount Cayley Volcanic Complex spans a much larger area than Mount Meager and has comparatively easier access through forestry service roads. Thus, in order to better understand the underground geological features that might indicate the viability of a geothermal project (e.g., rock permeability) and the characteristics of the subsurface hydrothermal features, we designed a Bouguer

gravity survey with a regular grid of campaign stations that encompassed the largest possible area of Mount Cayley. Depending on the results and the detected anomalies of the 2021 gravity survey, the grid will be modified in the future so that areas of greater interest have a denser network of stations.

## Methods

Gravity measurements at Mount Meager and Mount Cayley volcanic complexes were collected with a LaCoste & Romberg (G127) relative gravity meter. This gravity meter consists of a zero-length spring attached to a mass: this spring lengthens or contracts depending on the changes in gravity between locations, measuring this difference with a resolution up to a 1  $\mu\text{Gal}$  (1 mGal= 0.00001  $\text{m/s}^2$ ) (Lowrie, 2007). The LaCoste & Romberg gravity meters have been found to achieve a repeatability of less than 10  $\mu\text{Gal}$  between measurements, allowing them to be used for both spatial gravity surveys and gravity monitoring surveys (Rymer, 1994). The G127 meter is equipped with an Alliod feedback system that connects through Bluetooth to a data receiver allowing for continuous recordings of gravity data. During the 2021 summer surveys, we collected data at a frequency of 1 measurement per second for approximately 3 minutes. Data collection at each station was only started after allowing the gravity meter to stabilize for approximately one minute to ensure the quality of the measurement. Additionally, since the range of fine measurements of the G127 only spans from approximately 74 mGals to - 74 mGals, any larger gravity changes between measurement sites force the user to reset the coarse range of the gravity meter by finding the appropriate “counter”. In each gravity site, if so needed, the dial counter was changed and appropriately recorded.

After recording the data on site, we corrected gravity measurements for temporal effects: linear drift; Earth and ocean tides; and removed outliers from the data. Each of these effects was corrected using the open-source MATLAB software gTOOLS (Battaglia et al., 2022) in the following order:

### ***Filtering of outliers***

gTOOLS computes the weighted mean of the gravity values at each station and the standard deviation of the readings. The weights represent the reciprocal of the errors for each reading as relayed by the gravity meter (Battaglia et al., 2022). In the case of the current survey, all individual readings (1 per second) have the same standardized error as there is no averaging of the values before recording and processing them. gTOOLS plots the readings before filtering occurs, and then plots new filtered data after discarding all values that differ more than one sigma from the weighted mean (Battaglia et al., 2022). An example of the result of this process at one of the survey gravity benchmarks can be found in Fig. 1.

### ***Solid earth tides and ocean loading***

Due to the gravitational influence of the Sun and the Moon, the solid body of the Earth is deformed with a certain periodicity. The gravitational potential of the Earth is thus modified due to the changing distribution of its mass (Agnew, 2007; Lowrie, 2007). These body Earth-tides (also called load-tides) can be calculated for any point of the Earth's surface using Longman's formulas for computing the Tidal

accelerations due to the Moon and the Sun, and have been implemented by gTOOLS to correct the gravity values (Agnew, 2007; Battaglia et al., 2022; Longman, 1959).

The formation of tides in the oceans and other marine bodies is also a consequence of the gravitational pull of the Sun and the Moon and the change of Earth's mass distribution. The movement of large masses of water can be detected by precise gravity meters and can be substantial when measuring gravity near ocean bodies (Agnew, 2007; Duncan Carr Agnew, 2013); however, because its effect is smaller than our measurement error, in this case the ocean loading effect does not need to be corrected.

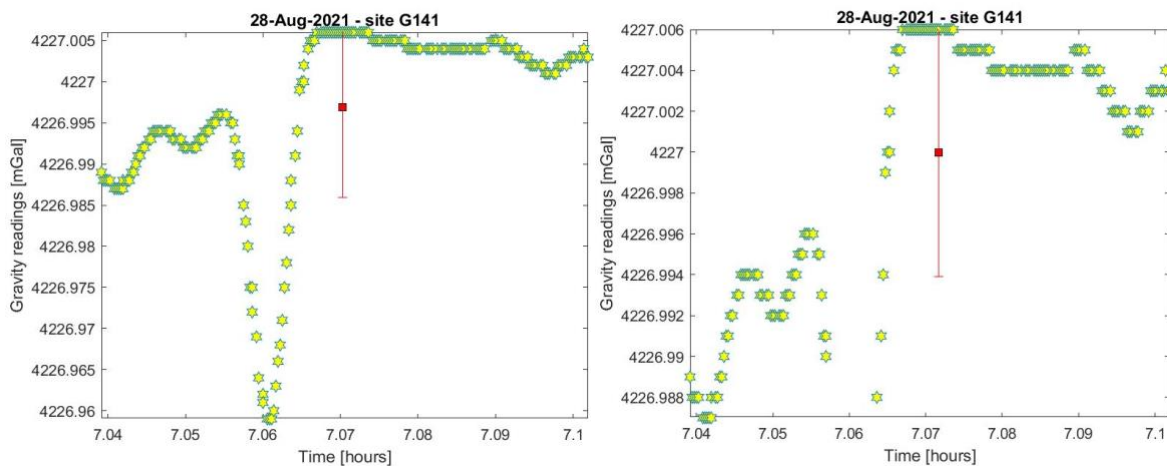


**Figure 1.** Gravity readings taken on August 28, 2021 at station G141 (lat: 50.72726, long: -123.47791), located on Salal Creek, north of the Meager Massif. (Left) Shows the gravity measurements raw, as collected with the LaCoste & Romberg G127 meter. (Right) Shows the same readings after gTOOLS identified and removed outliers.

### **Daily linear drift**

Gravity meters such as the LaCoste & Romberg and the Scintrex CG-5 are subject to instrumental drift caused by the intrinsic elastic properties of the gravimeter's zero-length spring (Lowrie, 2007; Seigel, 1995; Van Camp et al., 2017). This effect is linear and can be corrected by assuming the gravity at certain stations (e.g., a designated local reference station) is stable throughout the day. gTOOLS applies a linear regression to one loop of gravity data considering all station repetitions during the day and provides the weighted least-square gravity value as a gravity difference between the gravity survey stations and the base/reference station. After correcting the drift, any deviations from the linear estimation get accounted as standard deviations of the final measurement at the benchmark and incorporated in the error (Battaglia et al., 2022).

Daily drift can be mitigated by careful transport of the instrument, avoiding shocks, tilt, and violent changes in elevation (Carbone et al., 2017; Seigel, 1995). An example of a survey-day loop and the correction of linear drift done by gTOOLS is shown in Fig. 2.

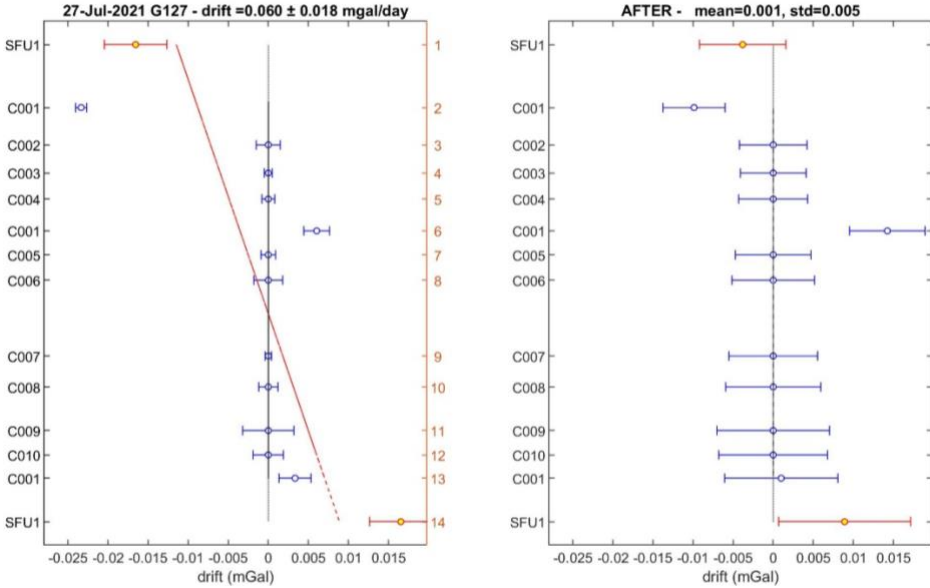


**Figure 2.** Gravity measurements and calculated linear drift for one survey loop at the Mount Cayley Volcanic Complex.

The final result from gTOOLS is a gravity difference between the designated reference station and their uncertainties at each benchmark.

**Data collection**

Gravity measurements were collected in daily survey loops where a designated reference station was measured at least two times per day: one at the beginning of the survey day and another at the end of the day. In the case of long travel times, we selected additional survey stations to be measured several times throughout the survey in order to better constrain the daily drift. Depending on the type of survey, the daily loop was modified to better suit the constraints of travel and time. In previous surveys (Grasby et al., 2021), several sites alongside the Sea to Sky Highway were linked to absolute gravity stations maintained by NRCan. These sites were used during the summer as reference stations for all survey loops. The coordinates and names of these stations are shown in Table 1, and the absolute gravity values as calculated in the [Phase 1 Geoscience BC Final Report](#) (Grasby et al., 2021) can be found in Table 2.

**Table 1.** Precise coordinates of reference stations in selected sites along the Sea to Sky Highway in Squamish, Pemberton, and Whistler, British Columbia. These reference sites have been linked to the absolute gravity site CGSN-9929-2008 (renamed as ABSW for short).

STAT	LAT (deg)	LONG (deg)	ELEV (m)	Sigma X (m)	Sigma Y (m)	Sigma H (m)
SFU2	50.11626	-122.95407	657.668	0.015	0.015	0.079
SFU3	50.32400	-122.75200	328.726	0.010	0.011	0.049
ABSW	49.3516344	-123.24916	148.885	0.013	0.013	0.060
SFU1	49.7183925	-123.146989	-11.813	0.012	0.016	0.048

**Table 2.** Absolute gravity values for stations linked directly or indirectly to ABSW (CGSN - 9929-2008). See Grasby et al. (2021) for more details on how these values were derived.

<b>SITE</b>	<b>Absolute Gravity (mGal)</b>
<b>ABSW</b>	980919.501
<b>SFU1</b>	980902.761
<b>SFU2</b>	980821.014
<b>SFU3</b>	980884.697
<b>BASE</b>	980840.757

### ***GPS measurements***

The precise location at each station was obtained with a Juniper Geode sub-meter GNSS receiver: this location is then used to correct for both temporal and spatial effects on the data. The Geode uses a SBAS correction signal to achieve a 30 cm horizontal accuracy (Juniper Systems, 2019): it has a receiver type GNSS single frequency with carrier phase tracking, 162 channels, and 3 channel SBAS parallel tracking. The data collected is in NMEA 0183, crescent binary format. To improve its line of sight, the Geode was mounted on a camera tripod levelled to be horizontal to the ground beside the gravity meter at a height of at least 1 metre. GNSS measurements were collected at a frequency of 1 Hz and stored for the totality of the gravity reading. The measurements were then post-processed to remove outliers in the data, and the average of the readings was used as the elevation of the gravity site, removing the height of the tripod.

### ***Data collection at the Mount Meager Volcanic Complex and surrounding areas***

The Bouguer gravity map previously presented in Grasby et al. (2021), which we also present here in Fig. 3, shows several areas of interest that would benefit from a more thorough understanding and a denser grid of gravity measurements. These areas are shown in Fig. 3 with black squares, and are marked with numerical tags 1, 2 and 3.

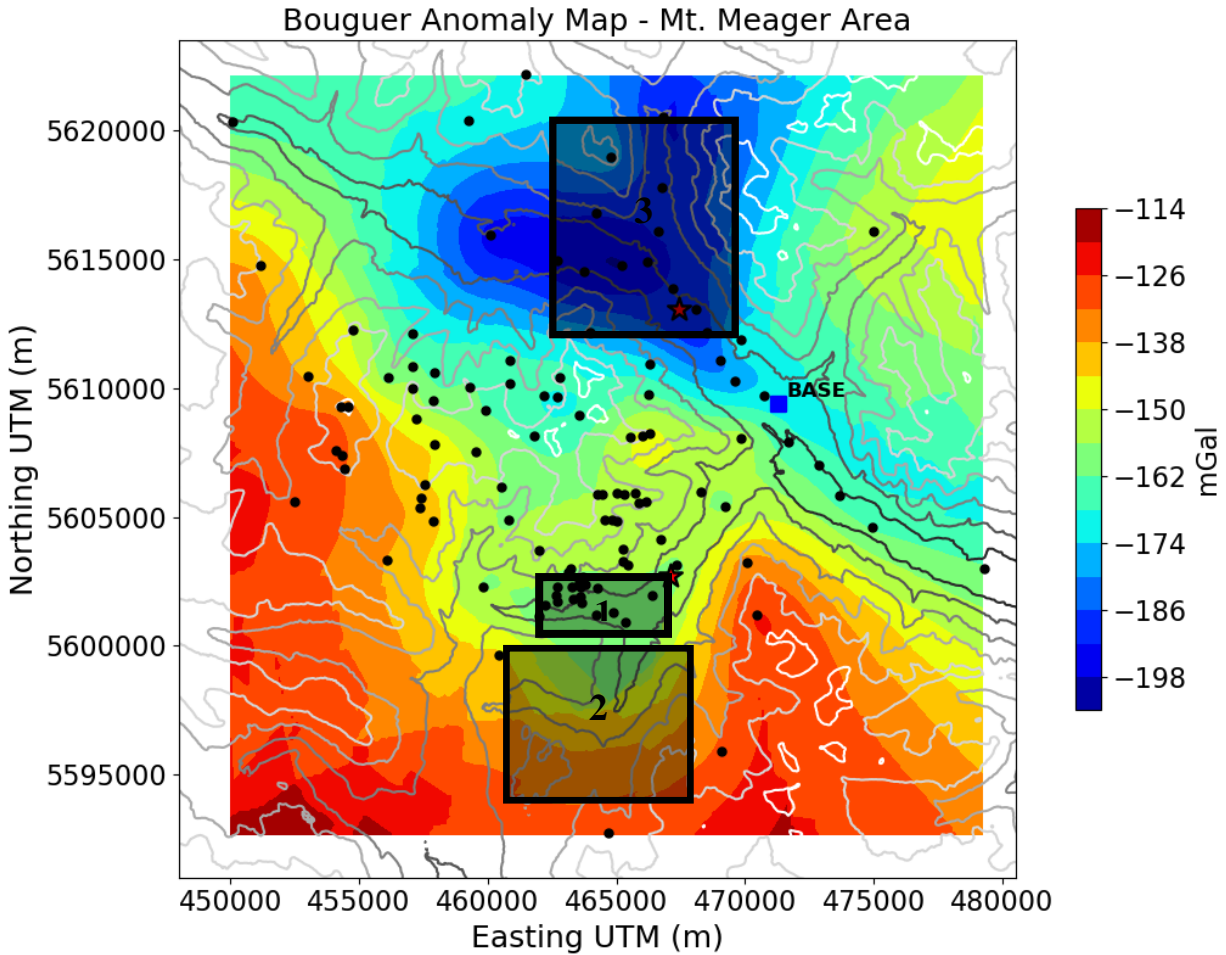


**Figure 3.** Bouguer gravity map of the Mount Meager Volcanic Complex as presented in Phase 1 Geoscience BC Final Report (Grasby et al., 2021). The areas where the density of gravity campaign sites was increased are marked with black squares.

***Survey loop: August 17, 2021***

This survey loop was undertaken with the aid of helicopter to travel between stations. In this area of focus (marked as 1 in Fig. 3), we measured 9 additional sites to further constrain the low Bouguer anomaly found there (shown as red points in Fig. 4). The reference stations used for this loop were SFU2 and BASE; however, station BASE was found to have a very large difference between measurements at the beginning and end of one day loop. This difference was interpreted as the result of the power plant adjacent to the site being operational and producing a large amount of ground vibrations in the second measurement of the survey. Therefore, data from BASE was excluded from further processing.

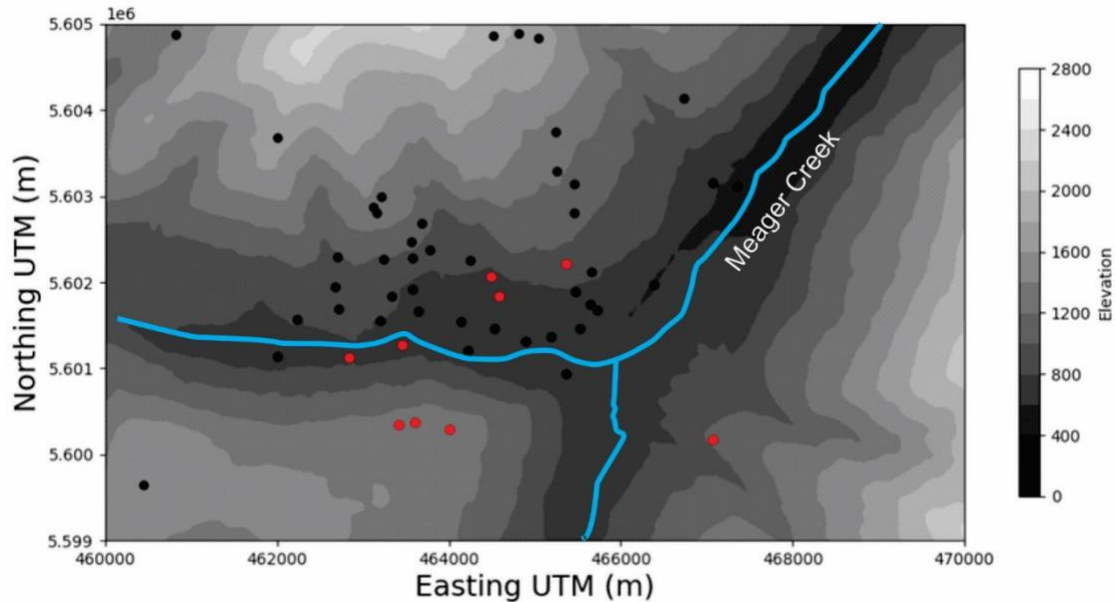


**Figure 4.** Gravity sites on the area of interest 1, with red circles showing sites visited on August 17, 2021.

***Survey loop: August 18, 2021***

With the help of staff from WellDunn Exploration, we continued focusing on the area of interest 1 by adding a further 10 gravity sites through a combination of hiking and driving along the old paths of the South Meager Geothermal Project Area. The sites are shown in red in Fig. 5. The reference stations for this loop were the new site CPRB (shown in Fig. 5) and site G123, which is shown as a square in Fig. 5.

***Survey loop: August 28, 2021***

The areas of focus for this loop (marked as area 2 and area 3 in Fig. 3), were surveyed with the aid of helicopter transport. Since the reference station for this survey loop was station SFU2, and the helicopter departed near the Whistler Heliport, the reference station was chosen as the first station visited during the day (site G133, the southernmost red point in Fig. 6). Ten additional sites were visited during this survey loop: 6 on the southernmost area of interest (area 2) and 4 in the northern part of the survey area (area of interest 3). The complete network of gravity sites for the Meager area can be seen in Figs. 6 and 7, with all the surveyed sites of the 2021 campaign shown in red.

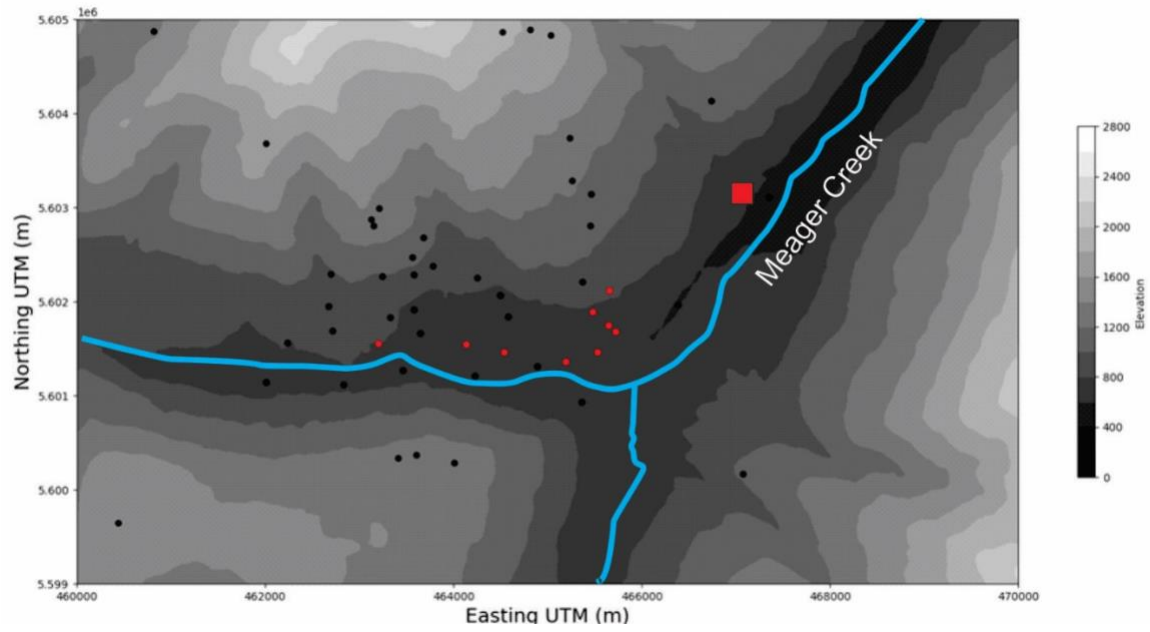


**Figure 5.** Gravity sites on area of interest 1, with sites in red showing the new gravity benchmarks visited on August 18, 2021. Station G123, a temporal reference site, is shown as a red square on the eastern part of the area.

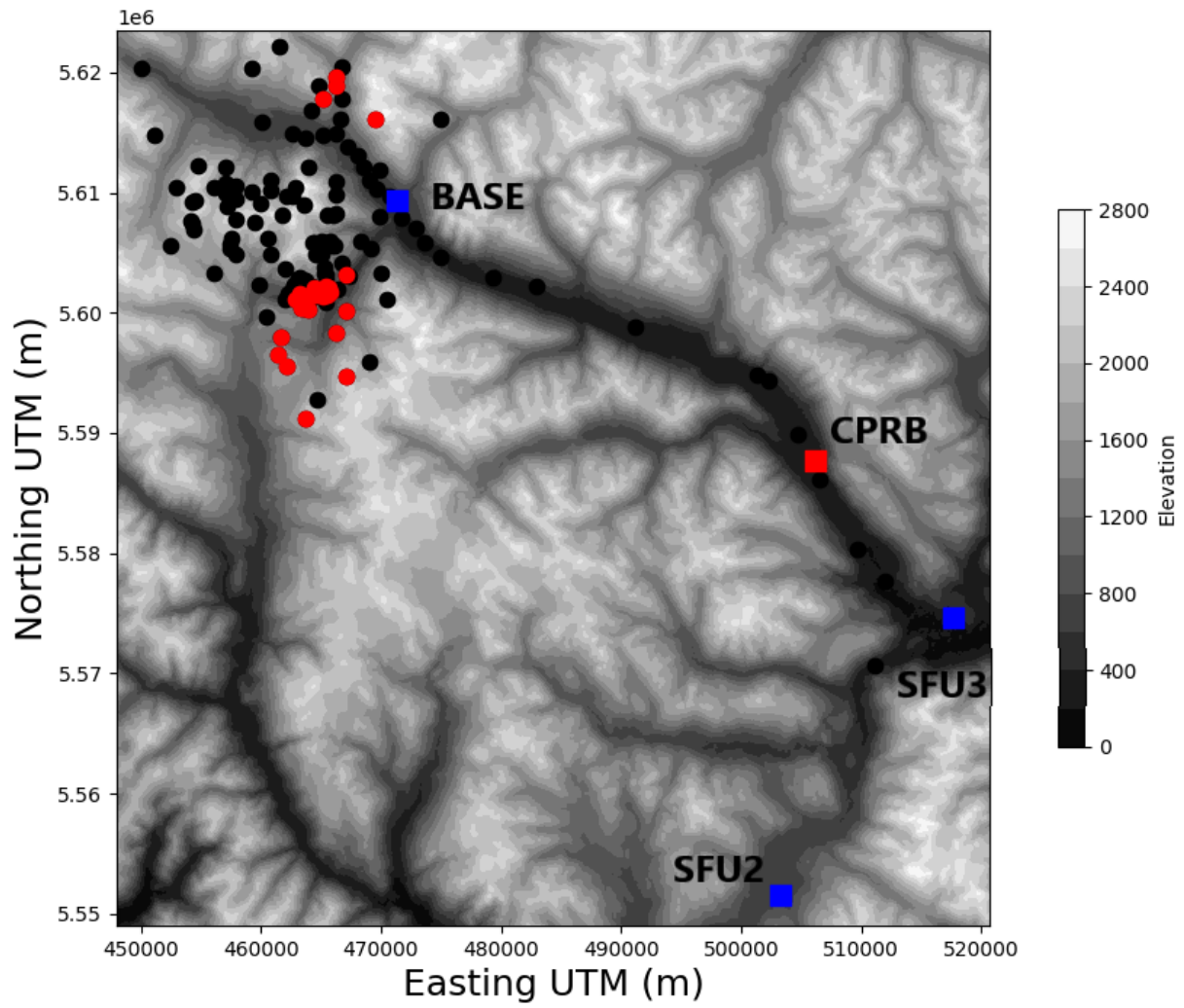


**Figure 6.** Gravity campaign sites (circles) and reference stations (squares) for the Mount Meager Volcanic Complex survey. All the sites surveyed in 2021 are shown in red.

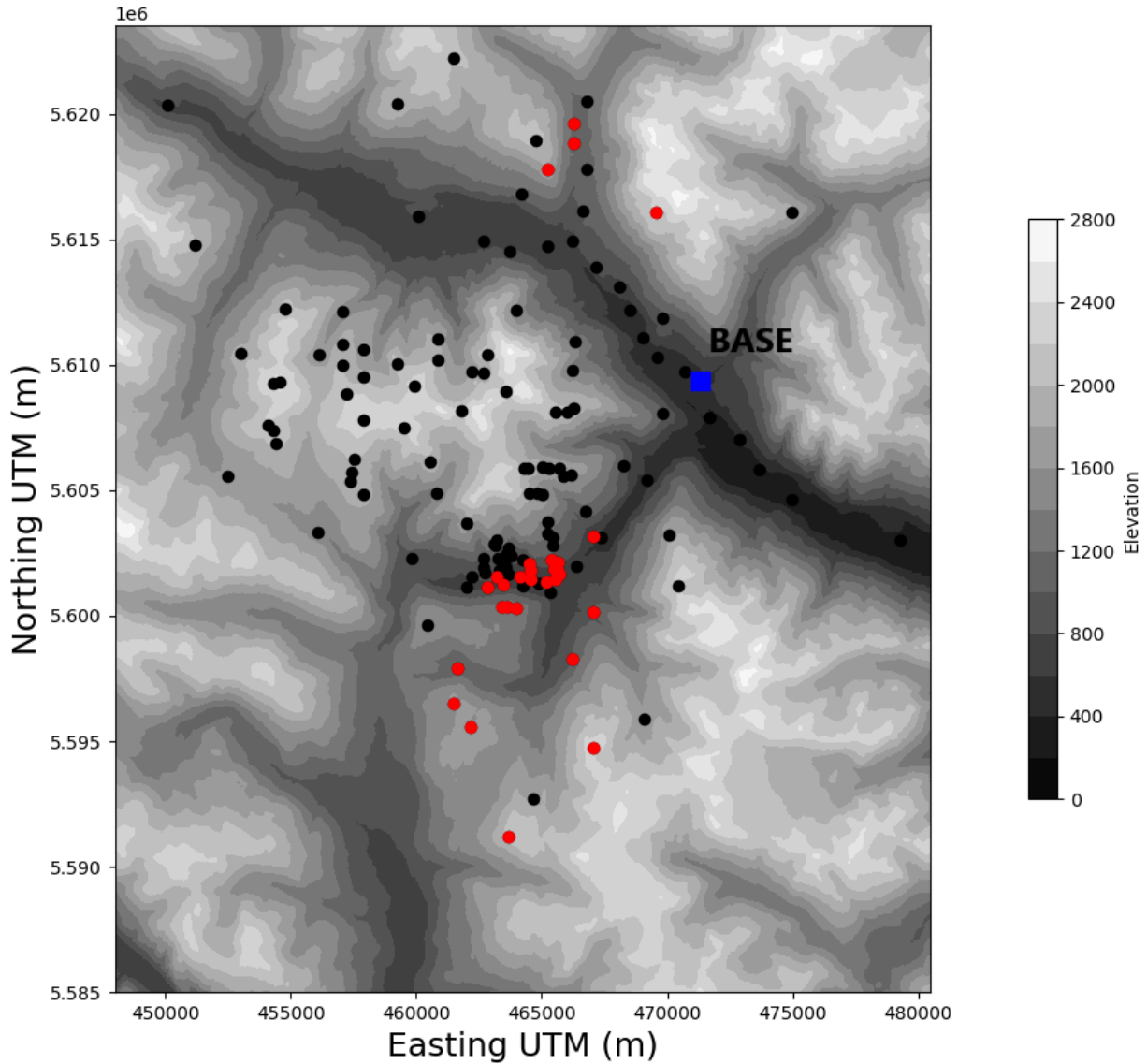


**Figure 7.** Close up of all gravity campaign sites for the Mount Meager Volcanic Complex. Sites surveyed in 2021 are shown in red, while previously surveyed sites are shown in black. The total number of gravity benchmarks occupied between 2019 and 2021 at Mt Meager is 142, in addition to the reference sites.

***Data collection at the Mount Cayley Volcanic Complex and surrounding areas***

In contrast with the survey at Mount Meager, the gravity survey grid at Mount Cayley was designed to span the largest amount of area in the most regular way, as to better identify possible signals of interest. The survey was done throughout 8 loop days on July, August, and September 2021. The July and August surveys were done entirely using a 4WD truck as transportation and surveying alongside the extensive set of logging roads around the Mount Cayley volcanic complex; higher elevation sites were surveyed in September by helicopter. The main reference site for this survey was station SFU1, although in certain

occasions SFU2 was used. Additionally, each day, several stations were chosen as temporal reference stations, and thus were surveyed several times during a day loop. Two of these temporal reference stations were chosen as future permanent sites: station CQMB will act as a secondary reference site for campaign stations on the western flank of the Mount Cayley Volcanic Complex, and site C011 will act as a reference site for future campaign stations on the Eastern Flanks of Mount Cayley. In total, 75 campaign gravity stations were established during the summer survey; these are shown in Fig. 8 in red, alongside the reference sites shown as blue squares.

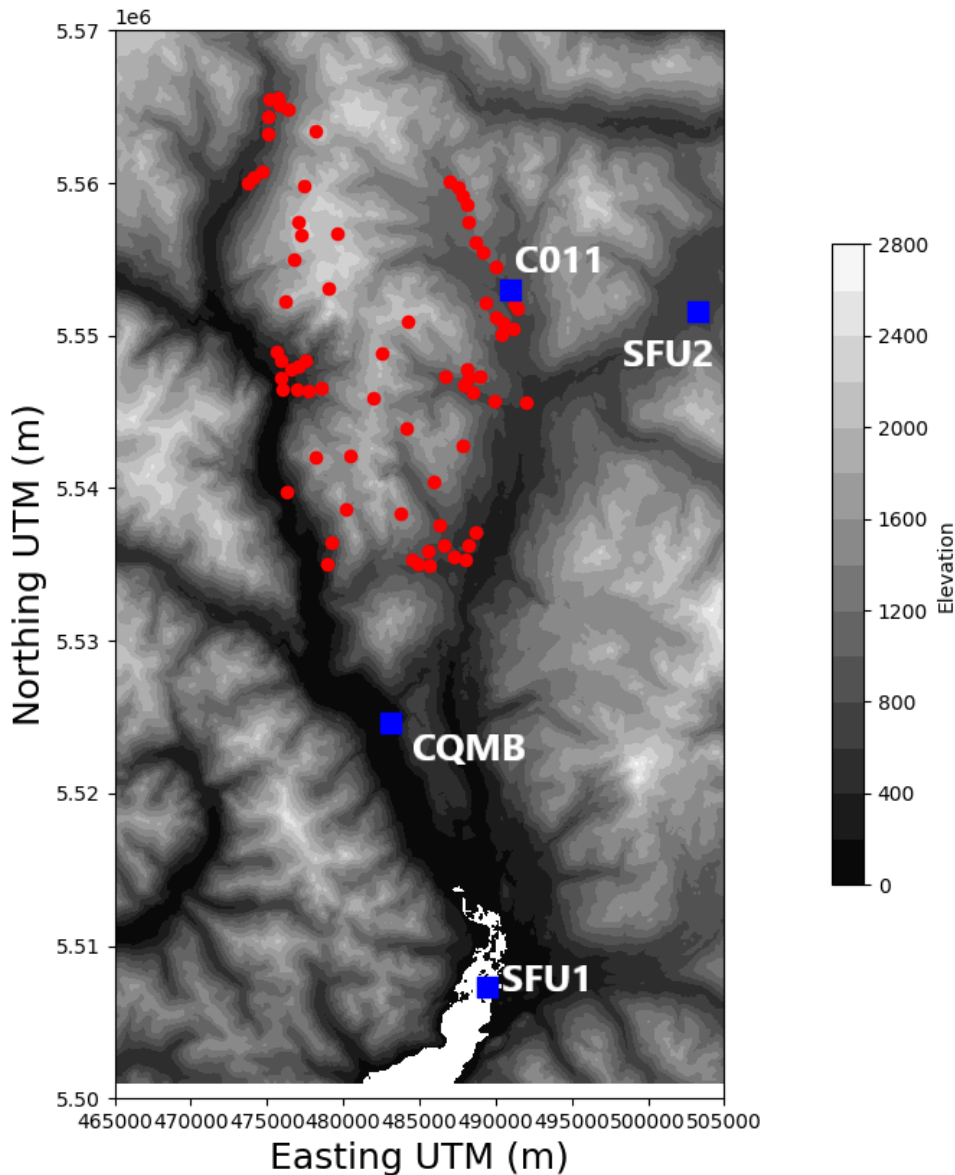


**Figure 8.** Gravity campaign sites surveyed at the Mount Cayley Volcanic Complex during summer 2021. All the campaign sites are shown as red circles, while reference stations are shown as blue squares.

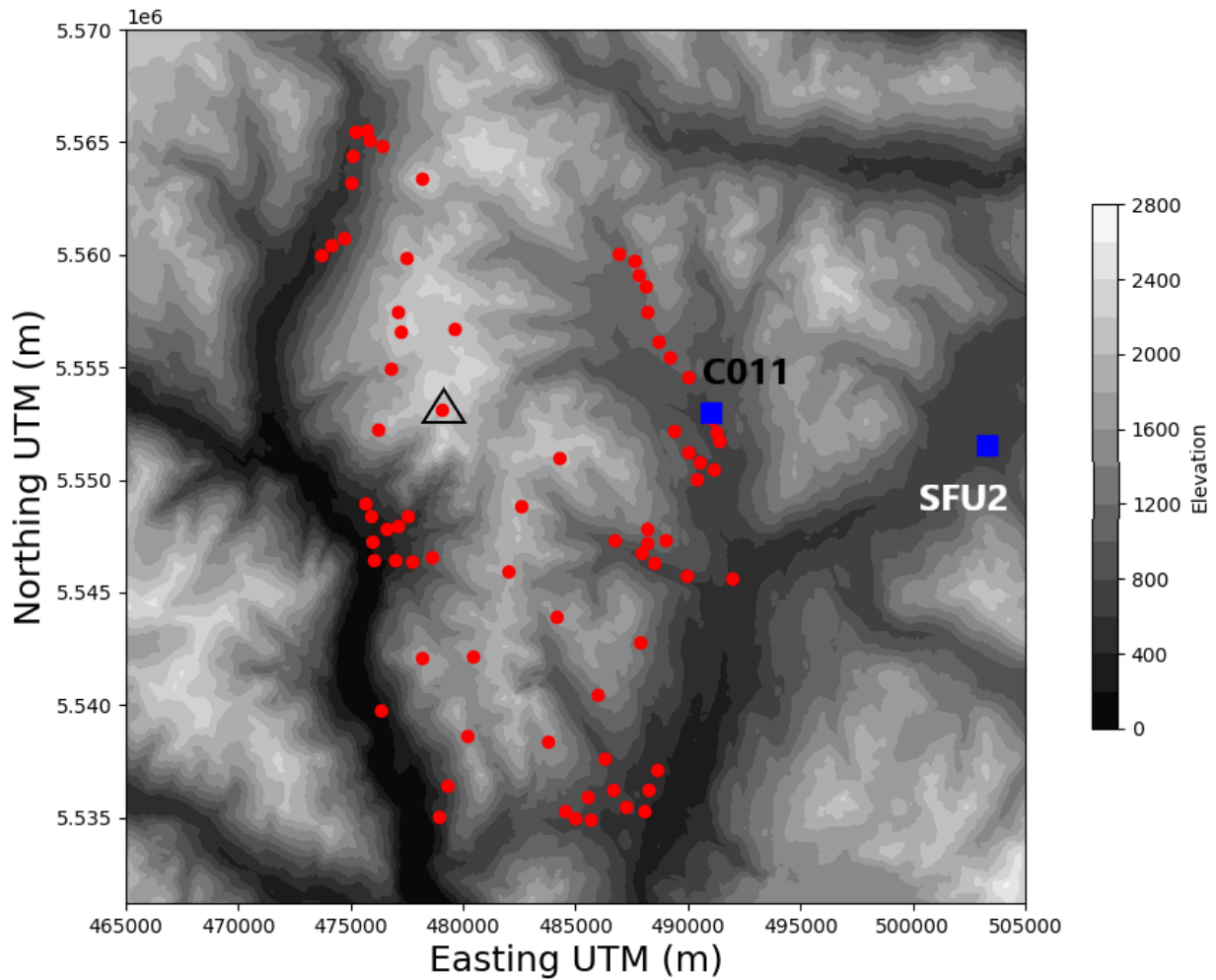


**Figure 9.** Close up of all gravity campaign sites measured in summer 2021 at the Mount Cayley Volcanic Complex. For reference, the black triangle represents the peak of Mount Cayley.

## Results

Gravity data processed for temporal effects using gTOOLS is presented in Tables 3, 4, and 5. All data is presented as gravity differences in comparison with a reference station (either SFU1 or SFU2). The processed data has been separated by volcanic complex (Meager or Cayley) and by reference station used. Since the standard deviation and standard error is estimated by gTOOLS depending on the daily drift, sites that were only visited once per survey loop cannot be assigned a stdev and stdev error value. However, the standard deviation for the reference stations for each loop gives an idea of the general estimation error for each survey loop.

**Table 3.** Least-square gravity differences (LSGRAVITY) between campaign sites at the Mount Meager Volcanic Complex and the reference site SFU2, surveyed during summer 2021. NaN values = Not a Number. No error could be calculated from the least square gravity reduction when there is only one occupation per site.

SITE	LATITUDE	LONGITUDE	ELEVATION	DATE	LSGRAVITY	STDEV	STDERROR
	DD	DD	metre		mGal	mGal	mGal
G114	50.55342	-123.50811	1281	17-Aug-21	-256.9104	NaN	NaN
G115	50.55420	-123.51373	1260	17-Aug-21	-112.4929	NaN	NaN
G116	50.55388	-123.51655	1246	17-Aug-21	-108.6247	NaN	NaN
G117	50.56226	-123.51591	701	17-Aug-21	-23.5308	NaN	NaN
G118	50.56076	-123.52467	722	17-Aug-21	-27.3773	NaN	NaN
G119	50.57081	-123.48906	901	17-Aug-21	-50.2237	NaN	NaN
G120	50.56953	-123.50145	801	17-Aug-21	-36.9453	NaN	NaN
G121	50.56739	-123.50017	775	17-Aug-21	-30.8823	NaN	NaN
G122	50.55255	-123.46476	1021	17-Aug-21	-67.6132	NaN	NaN
SFU2	50.11624	-122.95407	658	17-Aug-21	0.0055	0.0182	0.0129
CPRB	50.44137	-122.91283	227	18-Aug-21	79.466	0.0108	0.0076
G123	50.57942	-123.46509	629	18-Aug-21	-6.4825	0.011	0.0077
G124	50.57000	-123.48499	823	18-Aug-21	-36.9738	NaN	NaN
G125	50.56798	-123.48754	775	18-Aug-21	-28.2516	NaN	NaN
G126	50.56664	-123.48512	737	18-Aug-21	-21.0329	NaN	NaN
G127	50.56603	-123.48399	724	18-Aug-21	-20.6312	NaN	NaN
G128	50.56404	-123.48676	728	18-Aug-21	-21.2574	NaN	NaN
G129	50.56318	-123.49141	737	18-Aug-21	-22.711	NaN	NaN
G130	50.56413	-123.50070	754	18-Aug-21	-27.6965	NaN	NaN
G131	50.56475	-123.50642	774	18-Aug-21	-32.2367	NaN	NaN
G132	50.56473	-123.51965	806	18-Aug-21	-39.3375	NaN	NaN
SFU2	50.11626	-122.95408	658	18-Aug-21	0.0039	0.0105	0.0074
G133	50.47184	-123.51186	2106	28-Aug-21	-273.3189	0.009	0.0064
G134	50.51105	-123.53356	1602	28-Aug-21	-163.4324	NaN	NaN
G135	50.51923	-123.54346	1643	28-Aug-21	-172.936	NaN	NaN
G136	50.53206	-123.54123	1082	28-Aug-21	-75.9556	NaN	NaN
G137	50.53565	-123.47649	1009	28-Aug-21	-68.9866	NaN	NaN
G138	50.50357	-123.46423	2367	28-Aug-21	-327.2461	NaN	NaN
G139	50.69589	-123.43111	2325	28-Aug-21	-338.6772	NaN	NaN
G140	50.71110	-123.49275	1808	28-Aug-21	-253.3374	NaN	NaN
G141	50.72726	-123.47791	1165	28-Aug-21	-128.0306	NaN	NaN
G142	50.72042	-123.47787	1167	28-Aug-21	-127.2742	NaN	NaN
SFU2	50.11622	-122.95404	658	28-Aug-21	0.0031	0.0088	0.0062

**Table 4.** Least-square gravity differences (LSGRAVITY) between campaign sites at the Mount Cayley Volcanic Complex and the reference site SFU1, surveyed during summer 2021. This is not a comprehensive list of all measured sites at Mt Cayley Volcanic Complex during summer 2021, as some of the gravity sites were surveyed using SFU2 as reference station instead. The rest of gravity data as processed by gTOOLS are shown in Table 5. NaN values = Not a Number.

SITE	LATITUDE	LONGITUDE	ELEVATION	DATE	LSGRAVITY	STDEV	STDERROR
	DD	DD	meter		mGal	mGal	mGal
C058	50.22229	-123.30585	2177	21-Sep-21	-377.7739	NaN	NaN
C059	50.19048	-123.31572	2054	21-Sep-21	-338.4554	NaN	NaN
C060	50.16894	-123.3207	2202	21-Sep-21	-370.5081	NaN	NaN
C061	50.14654	-123.32515	1760	21-Sep-21	-277.424	0.0449	0.0318
C062	50.16111	-123.31887	2202	21-Sep-21	-370.5464	NaN	NaN
C063	50.16235	-123.28555	2172	21-Sep-21	-360.358	NaN	NaN
C064	50.12199	-123.33282	1736	21-Sep-21	-287.4181	NaN	NaN
C065	50.12979	-123.29345	2090	21-Sep-21	-347.0145	NaN	NaN
SFU1	49.71843	-123.14701	-12	21-Sep-21	-0.0067	0.0447	0.0316
C066	50.03135	-123.27294	1650	24-Sep-21	-266.1125	0.0326	0.0231
C067	50.11058	-123.22012	2079	24-Sep-21	-346.822	NaN	NaN
C068	50.09126	-123.24349	1981	24-Sep-21	-328.7254	NaN	NaN
C069	50.06521	-123.25154	1905	24-Sep-21	-318.1757	NaN	NaN
C070	50.04742	-123.22136	1673	24-Sep-21	-273.924	NaN	NaN
C071	50.03717	-123.16934	1314	24-Sep-21	-206.419	NaN	NaN
C072	50.01618	-123.19554	1323	24-Sep-21	-210.6579	NaN	NaN
C073	49.99749	-123.22679	1589	24-Sep-21	-266.1274	NaN	NaN
C074	49.99975	-123.27637	1601	24-Sep-21	-268.3122	NaN	NaN
C075	50.03051	-123.30511	1702	24-Sep-21	-291.5139	NaN	NaN
SFU1	49.71847	-123.14694	-12	24-Sep-21	0.0073	0.0316	0.0224
C001	49.96966	-123.16658	438	27-Jul-21	-56.4706	0.0069	0.004
C002	49.97174	-123.17786	620	27-Jul-21	-84.7467	NaN	NaN
C003	49.97820	-123.16424	453	27-Jul-21	-56.9774	NaN	NaN
C004	49.98616	-123.15834	404	27-Jul-21	-47.9933	NaN	NaN
C005	49.97824	-123.1861	664	27-Jul-21	-92.979	NaN	NaN
C006	49.99067	-123.19103	709	27-Jul-21	-102.0135	NaN	NaN
C007	49.96615	-123.19977	664	27-Jul-21	-93.5229	NaN	NaN
C008	49.97527	-123.20181	777	27-Jul-21	-113.4061	NaN	NaN
C009	49.96996	-123.21566	919	28-Jul-21	-138.1984	NaN	NaN
C010	49.96697	-123.20984	718	28-Jul-21	-104.1492	NaN	NaN
SFU1	49.71847	-123.14701	-12	27-Jul-21	0.0013	0.0083	0.0058
C011	50.12891	-123.12598	781	28-Jul-21	-99.2202	0.029	0.0205
C012	50.19259	-123.18284	1205	28-Jul-21	-171.8156	NaN	NaN
C013	50.18964	-123.17372	1215	28-Jul-21	-174.8541	NaN	NaN
C014	50.17931	-123.16663	1225	28-Jul-21	-177.6409	NaN	NaN
C015	50.18422	-123.1706	1244	28-Jul-21	-180.8025	NaN	NaN

SITE	LATITUDE	LONGITUDE	ELEVATION	DATE	LSGRAVITY	STDEV	STDERROR
	DD	DD	meter		mGal	mGal	mGal
C016	50.16950	-123.16539	1184	28-Jul-21	-169.2704	NaN	NaN
C017	50.15732	-123.15859	1088	28-Jul-21	-152.1683	NaN	NaN
C018	50.15119	-123.15112	1055	28-Jul-21	-145.4268	NaN	NaN
C019	50.14315	-123.13964	946	28-Jul-21	-126.2322	NaN	NaN
C020	50.06291	-123.11237	553	28-Jul-21	-64.1932	0.0243	0.0172
C021	50.07813	-123.18566	923	28-Jul-21	-128.8965	NaN	NaN
C022	50.07289	-123.16877	796	28-Jul-21	-107.676	NaN	NaN
C023	50.06889	-123.16097	779	28-Jul-21	-103.8277	NaN	NaN
C024	50.08265	-123.16556	1292	29-Jul-21	-193.4087	NaN	NaN
C025	50.07833	-123.15394	1149	29-Jul-21	-165.3797	NaN	NaN
C026	50.07684	-123.16526	1032	29-Jul-21	-147.4938	NaN	NaN
C027	50.06390	-123.14071	694	29-Jul-21	-90.0028	NaN	NaN
SFU1	49.71852	-123.14692	-12	28-Jul-21	0.004	0.0227	0.0161
C028	50.19851	-123.35476	710	29-Jul-21	-85.8807	NaN	NaN
C029	50.19531	-123.36245	581	29-Jul-21	-63.2059	NaN	NaN
C030	50.19122	-123.36838	468	29-Jul-21	-45.6668	NaN	NaN
C031	50.23537	-123.33123	1055	29-Jul-21	-150.4193	NaN	NaN
C032	50.23759	-123.3389	896	29-Jul-21	-121.1616	NaN	NaN
C033	50.24150	-123.34074	769	29-Jul-21	-101.5207	NaN	NaN
C034	50.24078	-123.34797	669	29-Jul-21	-84.1784	NaN	NaN
C035	50.23095	-123.34992	642	29-Jul-21	-78.6895	NaN	NaN
C036	50.22038	-123.34979	629	29-Jul-21	-74.1808	NaN	NaN
C037	50.00953	-123.33037	74	29-Jul-21	-13.1095	NaN	NaN
CQMB	49.87398	-123.23515	29	29-Jul-21	-6.3409	0.0029	0.0021
SFU1	49.71836	-123.14705	-12	29-Jul-21	0.0008	0.0021	0.0015
C038	50.08721	-123.31415	567	30-Jul-21	-74.438	NaN	NaN
C039	50.08365	-123.32064	424	30-Jul-21	-48.8548	NaN	NaN
C040	50.08226	-123.32721	346	30-Jul-21	-34.6132	NaN	NaN
C041	50.09251	-123.34026	468	30-Jul-21	-54.1218	NaN	NaN
C042	50.08750	-123.33724	391	30-Jul-21	-40.5018	NaN	NaN
C043	50.07716	-123.33585	238	30-Jul-21	-18.6047	NaN	NaN
C044	50.07104	-123.29913	945	30-Jul-21	-139.1957	NaN	NaN
C045	50.06958	-123.31147	581	30-Jul-21	-74.9534	NaN	NaN
C046	50.06999	-123.32146	383	30-Jul-21	-42.8803	NaN	NaN
C047	50.06996	-123.33508	193	30-Jul-21	-14.9073	NaN	NaN
C048	49.96712	-123.2936	447	30-Jul-21	-66.1695	NaN	NaN
C049	49.97990	-123.28808	678	30-Jul-21	-110.1173	NaN	NaN
CQMB	49.87402	-123.2352	29	30-Jul-21	-6.3216	0.023	0.0163
SFU1	49.71839	-123.14696	-12	30-Jul-21	0.0061	0.0219	0.0155

**Table 5.** Least-square gravity differences (LSGRAVITY) between campaign sites at the Mount Cayley Volcanic Complex and the reference site SFU2, surveyed during summer 2021. This is not a comprehensive list of all measured sites at Mount Cayley Volcanic Complex during summer 2021, as most of the gravity sites were surveyed using SFU1 as reference station instead. The rest of gravity data as processed by gTOOLS is shown in Table 4. NaN values = Not a Number.

SITE	LATITUDE	LONGITUDE	ELEVATION	DATE	LSGRAVITY	STDEV	STDERROR
	DD	DD	meter		mGal	mGal	mGal
C011	50.12891	-123.12594	781	19-Aug-21	-17.5181	0.013	0.0092
C050	50.12163	-123.14851	874	19-Aug-21	-33.3393	NaN	NaN
C051	50.11312	-123.14004	834	19-Aug-21	-27.1501	NaN	NaN
C052	50.10940	-123.13247	742	19-Aug-21	-12.2599	NaN	NaN
C053	50.10262	-123.13425	826	20-Aug-21	-27.4045	NaN	NaN
C054	50.10655	-123.12422	717	20-Aug-21	-8.3585	NaN	NaN
SFU2	50.11626	-122.95401	658	19-Aug-21	0.0007	0.0131	0.0092
C011	50.12892	-123.12596	781	20-Aug-21	-17.4718	0.0022	0.0016
C055	50.12605	-123.12514	758	20-Aug-21	-13.8574	NaN	NaN
C056	50.12095	-123.12251	729	21-Aug-21	-10.0183	NaN	NaN
C057	50.11785	-123.12051	697	21-Aug-21	-5.6209	NaN	NaN
SFU2	50.11624	-122.95405	658	20-Aug-21	0	0.0019	0.0013

*Absolute gravity measurements: All Sites*

Using the absolute gravity measurements presented in Table 2, the values of absolute gravity can be determined by the least-square gravity differences simply by summing the absolute gravity values of the appropriate reference station.

**Table 6.** Absolute gravity values for all campaign stations surveyed at the Mount Meager Volcanic Complex and surrounding areas on summer 2021. The absolute values were obtained by summing the absolute gravity value of reference station SFU2 (Table 2) with the least-squared gravity differences presented in Table 3.

SITE	LATITUDE	LONGITUDE	ELEVATION	ABS GRAV
	DD	DD	meter	mGal
G114	50.55342	-123.50811	1281	980564.104
G115	50.55420	-123.51373	1260	980708.521
G116	50.55388	-123.51655	1246	980712.389
G117	50.56226	-123.51591	701	980797.483
G118	50.56076	-123.52467	722	980793.637
G119	50.57081	-123.48906	901	980770.79
G120	50.56953	-123.50145	801	980784.069
G121	50.56739	-123.50017	775	980790.132
G122	50.55255	-123.46476	1021	980753.401
G123	50.57942	-123.46509	629	980814.532

SITE	LATITUDE	LONGITUDE	ELEVATION	ABS GRAV
	DD	DD	meter	mGal
G124	50.57000	-123.48499	823	980784.04
G125	50.56798	-123.48754	775	980792.762
G126	50.56664	-123.48512	737	980799.981
G127	50.56603	-123.48399	724	980800.383
G128	50.56404	-123.48676	728	980799.757
G129	50.56318	-123.49141	737	980798.303
G130	50.56413	-123.50070	754	980793.318
G131	50.56475	-123.50642	774	980788.777
G132	50.56473	-123.51965	806	980781.677
G133	50.47184	-123.51186	2106	980547.695
G134	50.51105	-123.53356	1602	980657.582
G135	50.51923	-123.54346	1643	980648.078
G136	50.53206	-123.54123	1082	980745.058
G137	50.53565	-123.47649	1009	980752.027
G138	50.50357	-123.46423	2367	980493.768
G139	50.69589	-123.43111	2325	980482.337
G140	50.71110	-123.49275	1808	980567.677
G141	50.72726	-123.47791	1165	980692.983
G142	50.72042	-123.47787	1167	980693.74
CPRB	50.44137	-122.91283	227	980900.48

**Table 7.** Absolute gravity values for all campaign stations surveyed at the Mount Cayley Volcanic Complex and surrounding areas on summer 2021. The absolute values were obtained by summing the absolute gravity value of reference station SFU1 and SFU2 (Table 2) with the least-squared gravity differences presented in Tables 4 and 5.

SITE	LATITUDE	LONGITUDE	ELEVATION	ABS GRAV
	DD	DD	meter	mGal
C001	49.96966	-123.16658	438	980846.29
C002	49.97174	-123.17786	620	980818.014
C003	49.97820	-123.16424	453	980845.784
C004	49.98616	-123.15834	404	980854.768
C005	49.97824	-123.1861	664	980809.782
C006	49.99067	-123.19103	709	980800.748
C007	49.96615	-123.19977	664	980809.238
C008	49.97527	-123.20181	777	980789.355
C009	49.96996	-123.21566	919	980764.563
C010	49.96697	-123.20984	718	980798.612
C011	50.12891	-123.12598	781	980803.541
C012	50.19259	-123.18284	1205	980730.945
C013	50.18964	-123.17372	1215	980727.907

SITE	LATITUDE	LONGITUDE	ELEVATION	ABS GRAV
	DD	DD	meter	mGal
C014	50.17931	-123.16663	1225	980725.12
C015	50.18422	-123.1706	1244	980721.959
C016	50.16950	-123.16539	1184	980733.491
C017	50.15732	-123.15859	1088	980750.593
C018	50.15119	-123.15112	1055	980757.334
C019	50.14315	-123.13964	946	980776.529
C020	50.06291	-123.11237	553	980838.568
C021	50.07813	-123.18566	923	980773.865
C022	50.07289	-123.16877	796	980795.085
C023	50.06889	-123.16097	779	980798.933
C024	50.08265	-123.16556	1292	980709.352
C025	50.07833	-123.15394	1149	980737.381
C026	50.07684	-123.16526	1032	980755.267
C027	50.06390	-123.14071	694	980812.758
C028	50.19851	-123.35476	710	980816.88
C029	50.19531	-123.36245	581	980839.555
C030	50.19122	-123.36838	468	980857.094
C031	50.23537	-123.33123	1055	980752.342
C032	50.23759	-123.3389	896	980781.599
C033	50.24150	-123.34074	769	980801.24
C034	50.24078	-123.34797	669	980818.583
C035	50.23095	-123.34992	642	980824.072
C036	50.22038	-123.34979	629	980828.58
C037	50.00953	-123.33037	74	980889.652
C038	50.08721	-123.31415	567	980828.323
C039	50.08365	-123.32064	424	980853.906
C040	50.08226	-123.32721	346	980868.148
C041	50.09251	-123.34026	468	980848.639
C042	50.08750	-123.33724	391	980862.259
C043	50.07716	-123.33585	238	980884.156
C044	50.07104	-123.29913	945	980763.565
C045	50.06958	-123.31147	581	980827.808
C046	50.06999	-123.32146	383	980859.881
C047	50.06996	-123.33508	193	980887.854
C048	49.96712	-123.2936	447	980836.592
C049	49.97990	-123.28808	678	980792.644
C050	50.12163	-123.14851	874	980787.675
C051	50.11312	-123.14004	834	980793.864
C052	50.10940	-123.13247	742	980808.754
C053	50.10262	-123.13425	826	980793.61
C054	50.10655	-123.12422	717	980812.656

SITE	LATITUDE	LONGITUDE	ELEVATION	ABS GRAV
	DD	DD	meter	mGal
C055	50.12605	-123.12514	758	980807.157
C056	50.12095	-123.12251	729	980810.996
C057	50.11785	-123.12051	697	980815.393
C058	50.22229	-123.30585	2177	980524.987
C059	50.19048	-123.31572	2054	980564.306
C060	50.16894	-123.32070	2202	980532.253
C061	50.14654	-123.32515	1760	980625.337
C062	50.16111	-123.31887	2202	980532.215
C063	50.16235	-123.28555	2172	980542.403
C064	50.12199	-123.33282	1736	980615.343
C065	50.12979	-123.29345	2090	980555.747
C066	50.03135	-123.27294	1650	980636.649
C067	50.11058	-123.22012	2079	980555.939
C068	50.09126	-123.24349	1981	980574.036
C069	50.06521	-123.25154	1905	980584.585
C070	50.04742	-123.22136	1673	980628.837
C071	50.03717	-123.16934	1314	980696.342
C072	50.01618	-123.19554	1323	980692.103
C073	49.99749	-123.22679	1589	980636.634
C074	49.99975	-123.27637	1601	980634.449
C075	50.03051	-123.30511	1702	980611.247

## Conclusions and Future Work

The analysis and modelling of gravity data have been used in several contexts to provide valuable information of subsurface geological structures or monitor changing geophysical phenomena. As such, the data collected at the Mount Meager Volcanic Complex and Mount Cayley Volcanic Complex during the summer of 2021 will surely prove equally useful to understand the geothermal potential of both areas, and to identify possible geohazards that might impact future developments. The data presented in this project has been processed to correct for temporal effects; however, it has not yet been processed to account for spatial features that may not be of interest but do nonetheless impact the value of the measured gravity at each site (e.g., topography, elevation change between stations, etc.). These spatial corrections were described in full in the report presented in the Geological Survey of Canada Open File 8732 (Grasby et al., 2020) and the [Geoscience BC Garibaldi Geothermal Energy Project - Phase 1 Final Report](#) (Grasby et al., 2021), and are necessary to generate a Bouguer Anomaly map similar to the one cited in Fig. 3. The removal of these spatial effects will be done in the future, and the gravity anomalies will be used to generate geophysical models of subsurface features informed by other geophysical data collected in the area.

## References

- Agnew, D.C. (2007). Earth Tides. In *Treatise on Geophysics, Geodesy* (pp. 163–195). Elsevier.
- Agnew, Duncan Carr. (2013). *SPOTL : Some Programs for Ocean- Tide Loading*.
- Battaglia, M., Calahorrano-Di Patre, A., & Flinders, A. F. (2022). gTOOLS, an open-source MATLAB program for processing high precision, relative gravity data for time-lapse gravity monitoring. *Computers and Geosciences*, 160(May 2021), 105028. <https://doi.org/10.1016/j.cageo.2021.105028>
- Carbone, D., Poland, M. P., Diament, M., & Greco, F. (2017). The added value of time-variable microgravimetry to the understanding of how volcanoes work. *Earth-Science Reviews*, 169(August 2016), 146–179. <https://doi.org/10.1016/j.earscirev.2017.04.014>
- Domra Kana, J., Djongyang, N., Raidandi, D., Njandjock Nouck, P., & Dadjé, A. (2015). A review of geophysical methods for geothermal exploration. *Renewable and Sustainable Energy Reviews*, 44, 87–95. <https://doi.org/10.1016/j.rser.2014.12.026>
- Grasby, S. E., Ansari, S. M., Barendregt, R. W., Borch, A., Calahorrano-DiPatre, A., Chen, Z., Craven, J. A., Dettmer, J., Gilbert, H., Hanneson, C., Harris, M., Hormozzade, F., Leiter, S., Liu, J., Muhammad, M., Quane, S. L., Russell, J. K., Salvage, R. O., Savard, G., ... Vestrum, Z. E. (2021). Garibaldi Geothermal Energy Project - Phase 1 Final Report. *Geoscience BC Report*, 2021–08.
- Grasby, S. E., Ansari, S. M., Bryant, R., Calahorrano-Di Patre, A., Chen, Z., Craven, J. A., Dettmer, J., Gilbert, H., Hanneson, C., Harris, M., Hormozzade, F., Liu, J., Montezadian, D., Muhammad, M., Russell, J. K., Salvage, R. O., Savard, G., Su, H., Tschirhart, V., ... Williamson, A. R. (2020). *The Garibaldi Volcanic Belt geothermal energy project - Mount Meager 2019 field program*. <https://doi.org/10.4095/326565>
- Jessop, A. M. (2008). *Review of National Geothermal Energy Program; Phase 2 – Geothermal Potential of the Cordillera*.
- Juniper Systems. (2019). *Geode Owner’s Manual*. Juniper Systems Inc.
- Longman, I. M. (1959). Formulas for computing the tidal accelerations due to the moon and the sun. *Journal of Geophysical Research*, 64(12), 2351–2355. <https://doi.org/10.1029/JZ064i012p02351>
- Lowrie, W. (2007). *Fundamentals of Geophysics*. In *Cambridge University Press*. Cambridge University Press. <https://doi.org/10.1017/CBO9780511807107>
- MacQueen, P., Zurek, J., & Williams-Jones, G. (2016). Connected magma plumbing system between Cerro Negro and El Hoyo Complex, Nicaragua revealed by gravity survey. *Journal of Volcanology and Geothermal Research*, 327, 375–384. <https://doi.org/10.1016/j.jvolgeores.2016.09.002>
- Miller, C. A., Currenti, G., Hamling, I., & Williams-Jones, G. (2018). Mass transfer processes in a post eruption hydrothermal system: Parameterisation of microgravity changes at Te Maari craters, New Zealand. *Journal of Volcanology and Geothermal Research*, 357, 39–55. <https://doi.org/10.1016/j.jvolgeores.2018.04.005>
- Rymer, H. (1994). Microgravity change as a precursor to volcanic activity. *Journal of Volcanology and Geothermal Research*, 61(3–4), 311–328. [https://doi.org/10.1016/0377-0273\(94\)90011-6](https://doi.org/10.1016/0377-0273(94)90011-6)
- Seigel, H. O. (1995). *A GUIDE TO HIGH PRECISION LAND GRAVIMETER SURVEYS*.

- Van Camp, M., de Viron, O., Watlet, A., Meurers, B., Francis, O., & Caudron, C. (2017). Geophysics From Terrestrial Time-Variable Gravity Measurements. *Reviews of Geophysics*, 55(4), 938–992. <https://doi.org/10.1002/2017RG000566>
- Zurek, J., Williams-Jones, G., Trusdell, F., & Martin, S. (2015). The origin of Mauna Loa's Nīnole Hills: Evidence of rift zone reorganization. *Geophysical Research Letters*, 42(20), 8358–8366. <https://doi.org/10.1002/2015GL065863>

# Chapter 5 – Summary of Broadband Magnetotelluric Measurements in the Garibaldi Volcanic Belt in August 2021

Unsworth, M.J., Hanneson, C., Slobodian, E.G.

Department of Physics, University of Alberta, Edmonton, Alberta, Canada

*The University of Alberta is furnishing this report "as is". The University of Alberta does not provide any warranty of the contents of the report whatsoever, whether express, implied, or statutory, including, but not limited to, any warranty of merchantability or fitness for a particular purpose or any warranty that the contents of the report will be error-free.*

## Introduction

Magmatism is a fundamental geological process that is important in many areas of Earth science. It occurs when crustal or mantle rocks melt to form partially molten rock, which rises due to its low density. The majority of the molten rock solidifies below the surface of the Earth to form plutonic, or intrusive, rocks. Molten rock that reaches the surface and erupts produces a volcano with associated volcanic, or extrusive, rocks. Magmatic systems are characterized by complicated interactions between the host rock, magma, and hydrothermal fluids. A number of fundamental scientific questions can be addressed by studying magmatic systems. A key question is how magmatic systems can transform mafic input into volcanic rocks with a broad range of compositions. Over geological time, this process has produced the bimodal distribution of oceanic and continental crust observed on Earth today. From a practical point of view, there are a number of compelling reasons for studying magmatic systems, with a specific focus on active volcanoes. These studies are important for understanding the nature of future eruptions, landslides, and the potential to generate geothermal energy from the hot water found in hydrothermal systems.

The Garibaldi Volcanic Belt is the location of Canada's most active volcanoes and contains some of Canada's most promising geothermal resources. There are many aspects of the history and structure of the Garibaldi Belt that are not well understood. These questions need to be addressed in order to fully understand: a) the hazards associated with future volcanic eruptions and landslides; and b) the nature of the geothermal resources that could be developed from the high temperature reservoirs that were discovered in the 1980s.

A key part of this type of study is to use geophysical data to image the subsurface structure beneath a region with active volcanoes. A range of geophysical methods are routinely used in this task, and by combining multiple methods, a more comprehensive subsurface image can be obtained than would be obtained with a single geophysical method. The magnetotelluric (MT) method is especially useful in this type of study because it is very effective at mapping subsurface fluids and molten rock.

With ongoing funding from GeoscienceBC and NRCan, a detailed multi-technique geophysical study of the Garibaldi Belt is in progress. Studies took place at Mount Meager in 2019 and 2020, and included magnetotelluric exploration (Grasby et al., 2020; Grasby et al., 2021). In 2021, the focus of this project shifted south to Mount Cayley. This chapter describes the results of a magnetotelluric study that took place at Mount Cayley in 2021 as an extension of the previous work at Mount Meager.

The aim of this project is to understand the hazards and geothermal resources of the Garibaldi Belt, by answering the following questions:

**(1) What is the nature of the geothermal resources that can be used for energy production?**

It is important to quantify the geothermal resources beneath a volcano to determine how much thermal energy could be extracted, either for direct use of heat or electricity generation. Geophysical data can be used to characterize the geothermal reservoir and the pathways that transport fluids from sources at depth. These data can contribute significantly to the development of a power plant by reducing the exploration risk.

**(2) What is the size, location and composition of the magma body beneath each volcanic centre?**

Determining the size and composition of magma bodies beneath the volcanoes can give information about size of future eruptions, on timescales from days to millennia. The last eruption at Mount Cayley occurred within the last 10 000 years, and hot springs indicate that the volcano still has a significant heat source. Understanding the nature of the entire magmatic system assists in the development of geothermal energy by defining the deeper source of heat and fluids feeding the present-day reservoirs. It could also lead to the discovery of concealed geothermal systems.

**(3) Are there structures within the volcanic edifice that could cause major landslides?**

Volcanic processes, such as hydrothermal circulation, can greatly decrease the strength of a volcanic edifice, and lead to sector collapses and major landslides. Mount Meager was the location of the largest recorded landslide in Canadian history in 2010 (Guthrie et al., 2012). Similar, large landslides have also taken place at Mount Cayley (Evans et al., 2001; Clague and Souther, 1982). Understanding the internal structure of the volcanic edifice is essential to determining the long-term risk of large events. This is also relevant to geothermal development, as it can guide plans to reduce the risks associated with constructing infrastructure on a restless volcano.

Information used to address these questions can be obtained from surface observations of erupted lavas, hydrothermal fluids, and gases. However, these methods are limited in what they can tell us about the structure of a volcanic system at depth. Geophysical methods are required to investigate the subsurface structure of these regions and a range of techniques can be used, as described elsewhere in this report. Each geophysical method measures a specific parameter that can be used to characterize the subsurface rock structure.

In many studies, geophysical exploration with the MT method has been used to image the structure of active volcanoes and associated geothermal fields. This method measures the subsurface resistivity, a parameter that is sensitive to the presence of fluids. The MT method was used at Mount Meager during exploration in 2019 and 2020 by groups from the University of Alberta and NRCan. This work is being

extended to Mount Cayley, and this report describes the work conducted by the University of Alberta at Mount Cayley in 2021.

## Geological Background of Mount Cayley

Mount Cayley is located in the Central Garibaldi Belt, which was formed by magmatism in the Northern Cascadia subduction zone (Green et al., 1988). Erupted lavas around Mount Cayley show a range of compositions from basaltic-andesite to rhyodacite. The Cayley Volcanic Field is located between the Cheakamus and Squamish river valleys in the central Garibaldi Volcanic Belt. Mount Cayley itself was formed during at least three periods of magmatism during the Pliocene and Pleistocene. Activity continued in the late Pleistocene and Holocene on a north-south axis extending north and south of Mount Cayley. These eruptions were dominantly subglacial. Vents in the Cheakamus Valley formed a 22-km-long lava flow sequence prior to 50 000 years before present that was topped by esker-like flows of late Pleistocene age. The youngest lava flows from Pali Dome West and from the subglacial Slag Hill volcano north of Mount Cayley were not impounded by ice at low elevations, implying that they erupted after the end of the Fraser Glaciation (less than 10 000 years ago). Large volcanic landslides have occurred at the heavily eroded Mount Cayley during the Holocene (Evans et al., 2001; Clague and Souther, 1982). At least five hot springs are present in valleys adjacent to the volcano, and shallow earthquakes have occurred in the vicinity. The summary above is based on the Smithsonian volcano database that can be found at: (<https://volcano.si.edu/volcano.cfm?vn=320811>).

## Previous Magnetotelluric Studies in the Garibaldi Volcanic Belt

Electrical resistivity is a useful parameter to measure in volcanic and geothermal studies because it is sensitive to the presence of magma, hydrothermal fluids, and the clay alteration produced by interactions of fluids with the host rock. A range of geophysical methods can be used to measure electrical resistivity. Electrical methods, such as direct current (DC) resistivity, use the injection of electric currents from metal electrodes, and have been used to image the near surface structure of many volcanos and geothermal systems worldwide (Eysteinnsson et al., 1994).

Exploration with DC resistivity in the Garibaldi Belt began in the 1970s and 1980s and included a number of DC resistivity surveys (Shore, 1975; Shore, 1981). A challenge of the DC resistivity method is that the depth of exploration is proportional to the current electrode spacing used. Thus, deeper sounding requires the deployment of large dipoles and this can be logistically challenging in rugged terrain. Deeper exploration is most efficient with electromagnetic (EM) methods that probe the resistivity structure with either naturally occurring electromagnetic signals or electromagnetic signals generated by a transmitter. The depth of exploration in these studies is controlled by the frequency of the EM signal, with the depth of investigation increasing as frequency decreases.

For imaging structure below a depth of 1-2 km, EM methods using natural signals are the most efficient, since it is expensive and logistically complicated to generate powerful, low-frequency EM signals with a transmitter. The most suitable natural source EM method is magnetotellurics, which is an established method that measures electric and magnetic fields at points on the surface. The MT method was developed in the 1950s and 1960s and has become a widely used tool in volcano studies and geothermal

exploration (Pellerin et al., 1996; Spichak and Manzella, 2009; Munoz, 2014). As shown in Fig. 1(a), EM waves originate in the atmosphere and travel toward the Earth. At the Earth's surface, most of the energy is reflected back into the atmosphere, but a small fraction of the energy enters the Earth. The depth to which this transmitted signal travels in the Earth depends on both the resistivity of the Earth and frequency of the signal through the skin depth equation. It can be shown mathematically that the resistivity of the Earth can be calculated from the ratio of the horizontal electric field and orthogonal horizontal magnetic field at the surface. This gives a value of resistivity that is an average from the surface to a depth of approximately one skin depth. By measuring EM signals at different frequencies, the variation of resistivity with depth can be determined. The instrument used in MT is basically a sensitive radio receiver that measures the electric and magnetic field components of these natural EM signals at the surface of the Earth. The instrument is shown schematically in Fig. 1(b). Additional details of the MT method are described by Vozoff (1991) and Simpson and Bahr (2005). Several prior studies have used MT exploration in the Garibaldi Belt and are summarized below.

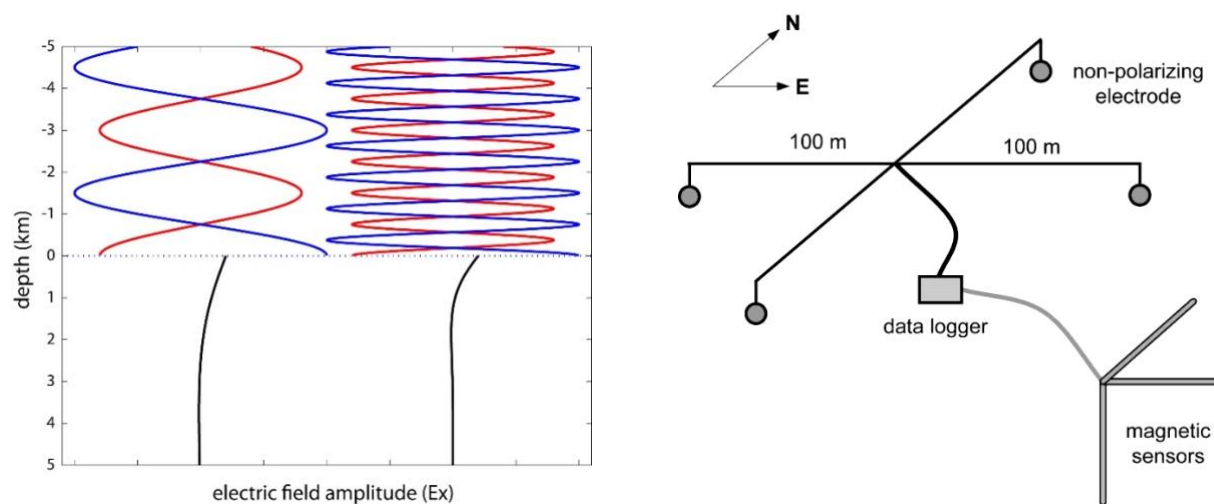


**Figure 1.** (a) Schematic of the electromagnetic (EM) signals used in magnetotelluric exploration. The blue lines show a low frequency signal (left) and high frequency signal (right) incident on the surface of the Earth. Most of the energy is reflected back into the atmosphere (red), and a small fraction is transmitted into the Earth (black). Within the Earth the EM energy travels by diffusion. Note that the low frequency signal travels deeper into the Earth than the high frequency. (b) Schematic diagram of a broadband magnetotelluric station used to measure the electric and magnetic fields. The electric fields are measured in the north-south and east-west directions using pairs of non-polarizing electrodes. The magnetic fields are measured in north-south, east-west and vertical directions using induction coils.

The locations of MT studies of the Garibaldi Belt are shown in Fig. 2. The first MT data were collected during an exploration program described by Pham (1977), Pham (1978) and Pham (1980). In total 17 MT soundings were collected, and shallow conductors were detected beneath both Mount Meager and Mount Cayley which were interpreted as being due to partial melt. MT exploration continued in 1982 with

the collection of a survey of 7 MT soundings at Mount Meager (Flores-Luna, 1986). A combination of 1-D, 2-D and 3-D analysis was applied to the Mount Meager data and defined a north-dipping conductor (Flores-Luna, 1986). This study was inconsistent with the presence of the shallow conductor at a depth of 2-4 km reported by Pham (1978).

New Lithoprobe MT data were collected in the Garibaldi Belt in the area around both Mount Meager and Mount Cayley by the Lithoprobe project in the 1980s.

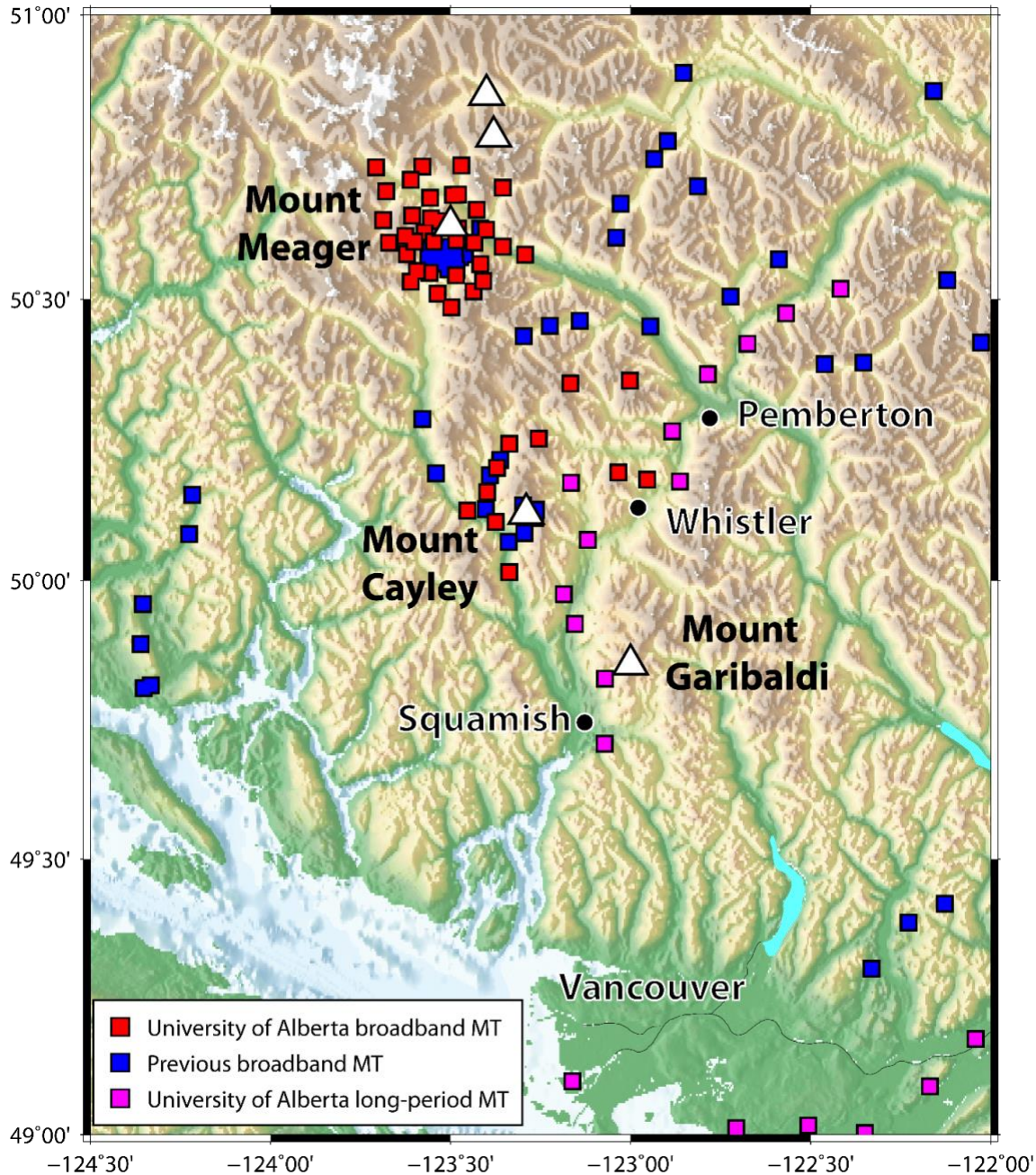


**Figure 2.** Regional map of the Garibaldi Belt showing previous magnetotelluric (MT) stations and also the 11 magnetotelluric stations described in this report. White triangles denote major volcanic centres.

Jones and Dumas (1993) applied a systematic approach to the whole Garibaldi MT dataset and developed the first regional scale resistivity model of the Garibaldi Belt. This study applied novel techniques to remove galvanic distortion from the MT data and undertook both 1-D and 2-D inversions. Jones and Dumas (1993) showed that shallow conductors were present beneath both Mount Cayley and Mount Meager and were interpreted as zones of hydrothermal alteration. The upper crust was found to have a high resistivity with a decrease in the mid-crust. Regional values in the mid-crust were intermediate and interpreted as saline aqueous fluids. Beneath the Garibaldi Volcanic Belt at Mount Meager and Mount Cayley, much lower resistivities were observed and interpreted as partial melt.

Since 2000, geothermal exploration with MT in the Garibaldi Belt has been focussed at Mount Meager. In 2000, a more detailed commercial MT survey collected 30 stations on the south slope of the Mount Meager Volcanic Complex (Candy, 2001). This gave a clearer impression of the geometry of the low resistivity layer. However, the combined MT dataset from surveys in the 1980s and 2000 was insufficient to reliably image the 3-D structure of the geothermal system, the magmatic system, or subsurface structures that may control the strength of the volcanic complex. To address the shortcomings of the previously collected MT data, a research program was initiated in 2019 that included a systematic component of MT exploration (Grasby et al., 2020; Grasby et al., 2021). This new study was motivated by the fact that: a) previous MT studies had identified a significant low resistivity target, but had insufficient station coverage to adequately define the geometry of the target; and b) since 2000, the MT method has advanced greatly and can now generate fully 3-D resistivity models because of improved instrumentation, new inversion algorithms, and accessibility to greater computer processing power. Fieldwork took place at Mount Meager in 2019 and 2020 and two types of MT instrument were used in the field. A group from NRCAN used audio-magnetotelluric (AMT) instruments that record high frequencies and image the near surface structure. The group from the University of Alberta used a separate broadband magnetotelluric (BBMT) system to measure lower frequencies and image structure to mid-crustal depths. Details of the data collection and analysis are described by Grasby et al. (2020) and Grasby et al. (2021).

The successful approach used at Mount Meager is now being extended to Mount Cayley. This report describes the field activity in 2021 in the area surrounding Mount Cayley. The resulting magnetotelluric data are described and recommendations for future work are described.

## Data Collection in the Mount Cayley Area in 2021

Studies of geothermal fields and volcanoes worldwide has shown the effectiveness of broadband MT surveys for locating subsurface hydrothermal and magmatic systems. Typical surveys now collect hundreds of MT stations and cover areas in excess of 100 km<sup>2</sup>. The University of Alberta MT research group has used this approach on a number of active volcanos in the Andes in recent years and been able to define the location, size and composition of magma bodies (Comeau et al., 2015; Cordell et al., 2018).

At Mount Cayley, it was planned to use a broadband MT survey to image the location and size of geothermal reservoirs beneath this volcano. It was also anticipated that these measurements might define the size and content of any magma bodies present beneath the volcano. The broadband MT data are sensitive to structures in the depth range of 1-50 km and typically have a horizontal spacing of 1-2 km

between stations. For more detailed studies of near-surface structure, the broadband MT data can be combined with audio-magnetotelluric (AMT) data.

At Mount Cayley, the electric fields were measured with dipoles 30-60 m in length and connected to the ground with porous pot electrodes. One pair of electrodes measured the north-south electric field component, and a second pair measured the east-west electric field component. The three orthogonal components of the magnetic field were measured with induction coils.

The duration of the measurement depends on the frequencies to be recorded. Logistics makes it efficient to record MT data for one day at each site, with recording continuing overnight. This typically gives measurements in the frequency band 1000 – 0.001 Hz. From the physics of EM signal propagation in the Earth, these frequencies typically sample from the surface to a depth of up to 50 km, depending on the subsurface conditions. Commercial MT instruments are manufactured by a number of companies and have been developed to be very efficient. All BBMT data collection at Mount Meager in August 2021 used the MTU-5C instruments manufactured by Phoenix Geophysics, a Canadian company based in Toronto.

Each phase of data collection began with instrument calibration that is an important check on the functioning of the instruments and induction coils. Calibrations were repeated at the end of data collection to confirm that the instrument responses had not changed. The calibration files are included in the data archive.

During the August 2021 broadband MT survey, data were collected at 11 points. A total of 4 stations were accessed by helicopter while 7 were accessed by truck. The station deployment is shown in Fig. 3 and details of each station are listed in Table 1. Recording times are shown in Fig. 4. Since MT is a natural source EM method, the data quality depends on the signal strength which is out of the control of the user. During the 2021 survey, the signal levels were generally low as expected, since 2021 coincided with low sunspot numbers following the minimum of the approximately 11-year solar cycle. However, given the low levels of human-caused electromagnetic noise in the study area, the MT data were generally of good quality, as explained in the following section. In the field, the MT data were recorded in geomagnetic coordinates with the x-axis oriented to geomagnetic north and the y-axis oriented geomagnetic east.

In 2021, standard MT data collection techniques were used, generally without problems. High contact resistances were obtained at some sites, as expected with high resistivity crystalline rocks or ice present in the subsurface.

## Analysis of the 2021 Broadband MT Data

### *Time series analysis for the 2021 Mount Cayley data*

Time series data from the 2021 MT stations were processed using the statistically robust algorithm of Egbert and Booker (1986). In the first processing step, the time series were processed to calculate the spectra of the electric and magnetic field components as functions of frequency. Since measurements were usually made simultaneously at multiple stations, the remote reference method of Gamble et al. (1979) was used to separate signal from noise when appropriate. In the second step, the spectra were used to compute the apparent resistivity and phase as functions of frequency. These quantities are

important because they depend only on Earth resistivity structure, and not on the characteristics of the EM signals. All 11 soundings are shown in Figs. 5a to k.

### ***Characteristics of the 2021 apparent resistivity and phase data***

Apparent resistivity can be considered as an average resistivity of the Earth from the surface to the maximum depth to which the EM signal penetrates. Thus, when apparent resistivity is plotted as a function of decreasing frequency, this corresponds to increasing depth in the Earth.

In each sounding there are two curves for apparent resistivity. The first is calculated from the north-south electric field and the east-west magnetic field, which is referred to as the XY component of the data. The second is calculated from the east-west electric field and the north-south magnetic field, which is referred to as the YX component of the data. By looking at both the XY and YX components of the data, information can be determined about whether the subsurface resistivity structure is 1-D, 2-D or 3-D. Inspection of MT sounding curves can determine the quality of the data. A number of tests can be applied to the data.

- (1) The apparent resistivity and phase curves should be smooth, as a function of frequency. This is generally the case for the 2021 MT data in the frequency band 100 – 0.001 Hz. The accuracy of the apparent resistivity and phase decreases as frequency decreases. This is because, for a given recording time, there will be fewer estimates of the low frequency signals than the high frequency signals.
- (2) The apparent resistivity and phase should be mutually consistent. It can be shown mathematically that when apparent resistivity increases with decreasing frequency, the phase angle should be in the range 0-45°. Similarly, when the apparent resistivity decreases with decreasing frequency, the phase angle should be in the range 45-90°. This observation provides a self consistency test for MT data and is generally valid for the stations collected in 2021.

Visual inspection of the apparent resistivity curves in Fig. 5 shows a number of features.

- (1) At high frequency (> 1 Hz), the apparent resistivity is quite variable and in the range 100 - 10 000  $\Omega\text{m}$ . These high frequency signals measure near surface structure, implying that the actual resistivity is spatially quite variable. This is as expected in volcanic environments where materials with a wide range of resistivity are found. Regions with recently extruded lava can have a resistivity in excess of 10 000  $\Omega\text{m}$ . In contrast, an area where the rock has undergone hydrothermal alteration to form clay minerals can have a resistivity less than 1  $\Omega\text{m}$ .
- (2) At low frequency (< 1 Hz), all of the MT curves show a decreasing apparent resistivity in both the XY and YX components. This implies that there is a low resistivity layer at depth beneath the entire survey area. An inversion of the MT data is needed to determine the actual depth and horizontal extent of the layer.
- (3) Electric and magnetic fields are each measured in two orthogonal directions. Thus, apparent resistivity / phase can be computed from the  $E_x$  and  $H_y$  components, or from the  $E_y$  and  $H_x$  components. These are referred to as the XY and YX data components in Fig. 5. If the XY and YX

components are identical for all co-ordinate systems, then this would imply that the subsurface resistivity structure was 1-D. This is clearly not the case for the MT data collected in 2021. The sounding curves shown in Fig. 5 give evidence of a 3-D resistivity structure, which requires a 3-D approach to inversion.

- (4) The XY and YX curves are often offset and parallel at high frequency showing the presence of complicated effects due to 3-D resistivity structure in the near surface. These offsets are sometimes referred to as static shifts and can greatly complicate MT data analysis in volcanic environments (Arnason, 2015).

Fig. 6 shows a comparison of the 2021 data with the Lithoprobe data collected in the Squamish Valley. The 9 stations are shown in a sequence from north to south. Note that the shape of the apparent resistivity and phase curves is similar in the two datasets.

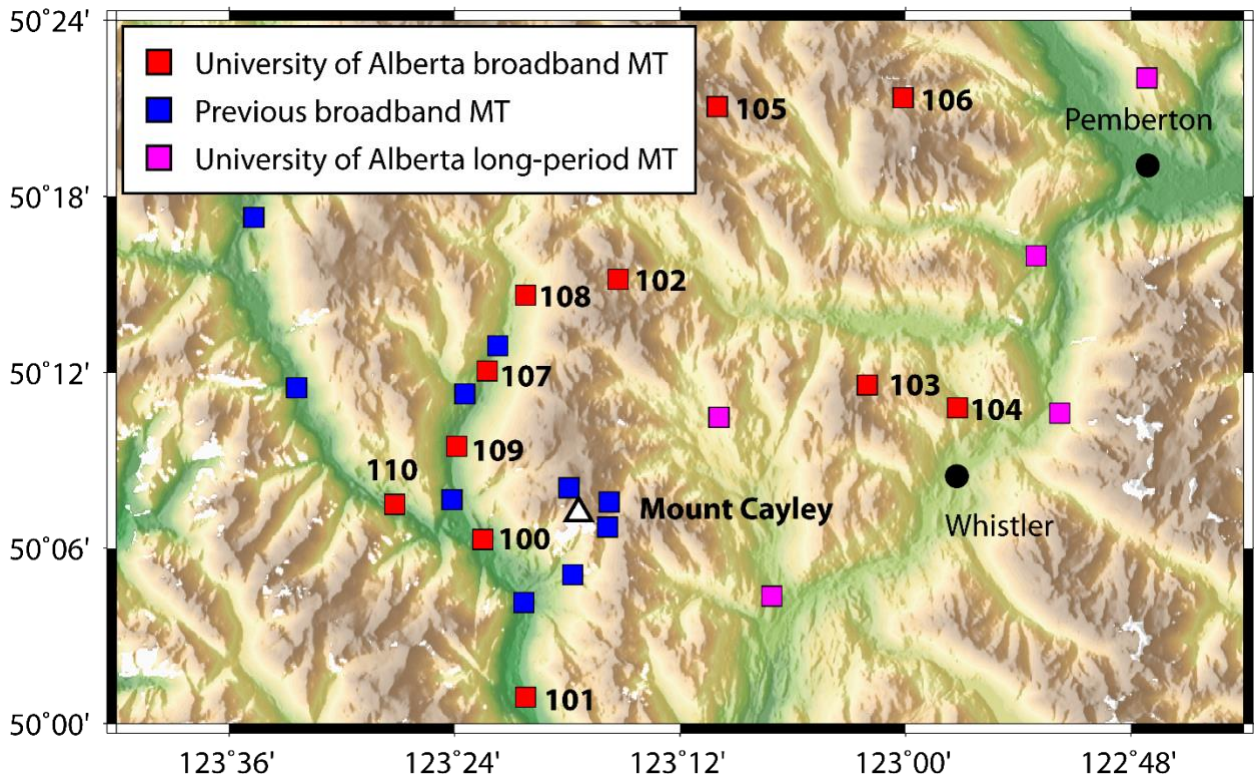


**Figure 3.** Regional map showing the 11 stations collected in 2021 in red (CAY100 - CAY110). Broadband stations from the Lithoprobe project are shown in blue.

***Characteristics of the Mount Cayley induction vector data***

MT instruments also measure the vertical component of the magnetic field. This quantity is sensitive to horizontal changes in resistivity structure and complements the apparent resistivity and phase data described above. The vertical magnetic field data at a set of stations can be conveniently plotted as induction vectors. When plotted in the Parkinson convention, the in-phase component of induction

vectors point at conductors (regions of low resistivity). If plotted in the Weise convention, the in-phase component of these vectors points away from conductors.

Fig. 7 shows the in-phase components of the induction vectors in the Weise convention. Note that this figure contains both the 11 stations collected in 2021, as well as earlier data collected by Lithoprobe project and described by Jones and Dumas (1993). Fig. 7 also includes the long-period MT data collected by the University of Alberta in 2019 using the Narod Intelligent Magnetotelluric System (NIMS) on a transect along the Sea-to-Sky Highway at locations shown in Figs. 2 and 3.

At a frequency of 2 Hz, the EM signals sample the near surface resistivity structure, and the induction vectors plotted in Fig. 7(a) all point west away from Mount Cayley. This indicates that the Mount Cayley complex has a low resistivity close to the surface. This is likely caused by hydrothermal fluids and extensive near surface clay alteration. Note the consistent direction of the induction vectors located west of Mount Cayley. This includes data collected in 2021 and Lithoprobe data recorded the 1980s. At a lower frequency of 0.01 Hz, the EM signals sample deeper resistivity structure, and the induction vectors plotted in Fig. 7(b) show a more complex pattern. Note that at this frequency, data are available at the long-period MT stations deployed by the University of Alberta. Inversion of the data will be required to determine the subsurface resistivity structure responsible for the observed induction vectors.

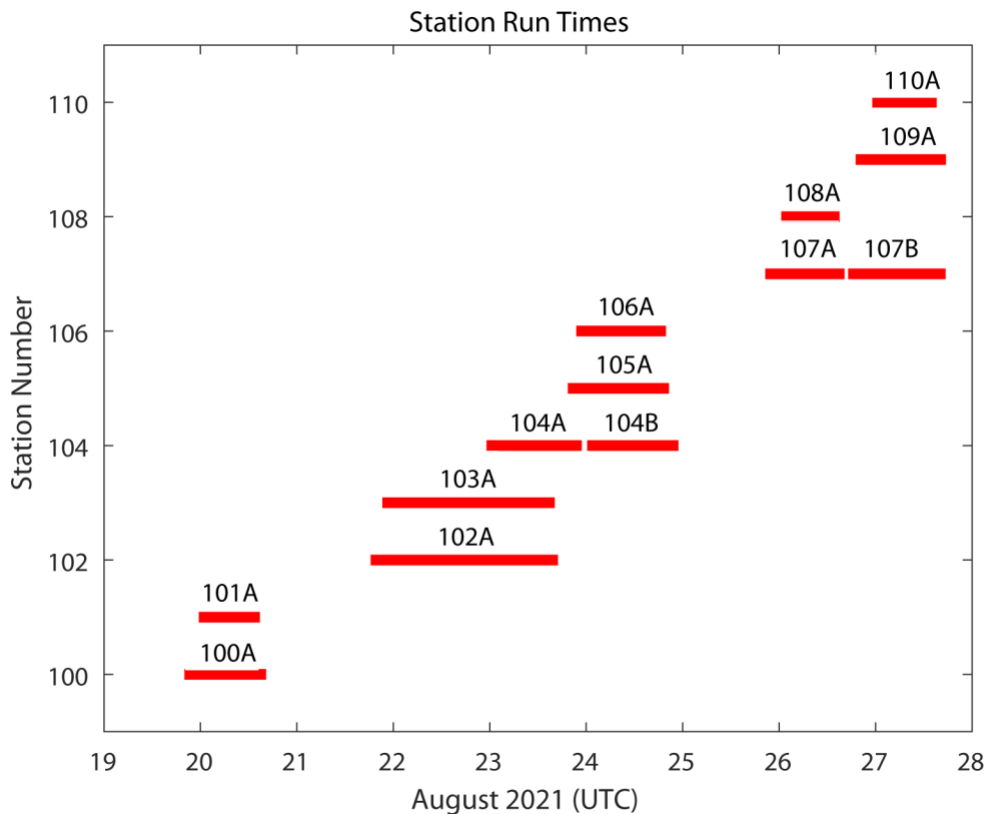


**Figure 4.** Run times of data collection during the August 2021 survey at Mount Cayley.

## Summary and Future Work

### **Summary**

The results above have shown that high quality MT data were collected in 2021 at the 11 measurement points around Mount Cayley. The MT data satisfy tests for internal consistency and are also consistent with legacy data collected in the 1980s during the Lithoprobe project.

### **Ongoing data analysis**

Additional data analysis is required and will include the following tasks:

- (1) MT data will be collected at additional measurement points in 2022 to give a dense grid of stations on the volcanic edifice.
- (2) The data will be inverted to give a 3-D model of subsurface resistivity. This will use the same approach used for the broadband MT data collected at Mount Meager in 2019 and 2020, with the ModEM algorithm of Kelbert et al., (2014).
- (3) The resulting resistivity model will be interpreted to determine the subsurface location of regions containing aqueous fluids, partial melt, and hydrothermal alteration. A key part of this process will be the joint analysis of all types of geophysical and geological data collected at Mount Cayley.

## Data

The measured MT time series data have been provided as requested and consist of the following files:

- (a) A summary of the data acquisition is provided in an Excel file listing recording dates, locations, and recording parameters.
- (b) The time series data files are sorted by recording date, with one folder being provided for each instrument and data run. The folder name contains the instrument number and the start time. Subfolders contain the data recorded at sample rates of 150 Hz and 24 KHz.
- (c) The calibration files recorded in 2021.

These time series data and calibration files can be viewed using the program EMPower provided by Phoenix Geophysics. The data files can also be processed using the EMPower software package.

**Table 1.** Run information for the 11 MT stations collected in 2021 in the Garibaldi Belt.

Start date	End date	Station /Run	Data File Name	Test Run File Name	Latitude (°N)	Longitude (°W)	Elevation (m)	N-S Line (m)	E-W Line (m)	Helicopter (H) or Truck (T)
08-19	08-20	CAY100A	10351_2021-08-19-200157	10351_2021-08-19-194538	50.105	123.375	139.691	50	48	T
08-19	08-20	CAY101A	10352_2021-08-19-233619	10352_2021-08-19-222312	50.015	123.337	59.9604	56	49	T
08-21	08-23	CAY102A	10351_2021-08-21-182307	10351_2021-08-21-180358	50.253	123.255	1642.84	42	44	H
08-21	08-23	CAY103A	10352_2021-08-21-211744	10352_2021-08-21-205808	50.193	123.034	1493.73	44	29	H
08-22	08-23	CAY104A	10430_2021-08-22-231215	10430_2021-08-22-223537	50.18	122.954	1082.11	36	39	T
08-23	08-24	CAY104B	10430_2021-08-23-233530	N/A	50.18	122.954	1082.11	36	39	T
08-23	08-24	CAY105A	10351_2021-08-23-192631	10351_2021-08-23-190405	50.351	123.167	1822.12	48	57	H
08-23	08-24	CAY106A	10352_2021-08-23-213519	10352_2021-08-23-210447	50.356	123.002	1516.38	41	46	H
08-25	08-26	CAY107A	10351_2021-08-25-203225	10351_2021-08-25-195912	50.201	123.371	438.709	39	49	T
08-26	08-27	CAY107B	10351_2021-08-26-163156	N/A	50.201	123.371	438.709	39	49	T
08-25	08-26	CAY108A	10352_2021-08-26-003212	10352_2021-08-25-234258	50.244	123.337	801.058	55	50	T
08-26	08-27	CAY109A	10430_2021-08-26-190406	10430_2021-08-26-184200	50.158	123.398	313.541	56	51	T
08-26	08-27	CAY110A	10352_2021-08-26-231105	10352_2021-08-26-223839	50.125	123.453	247.334	30	39	T

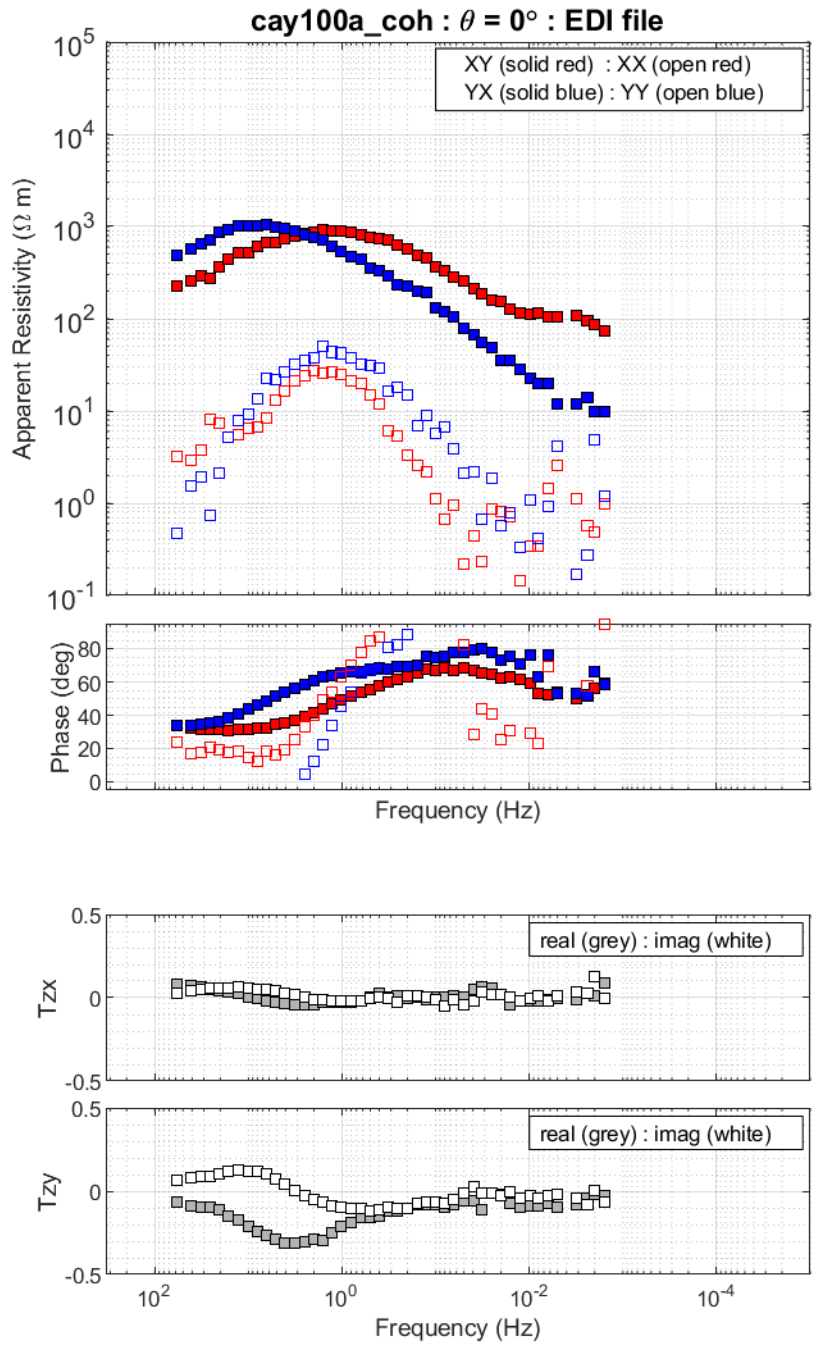


**Figure 5(a).** Apparent resistivity, phase and tipper at station CAY100.

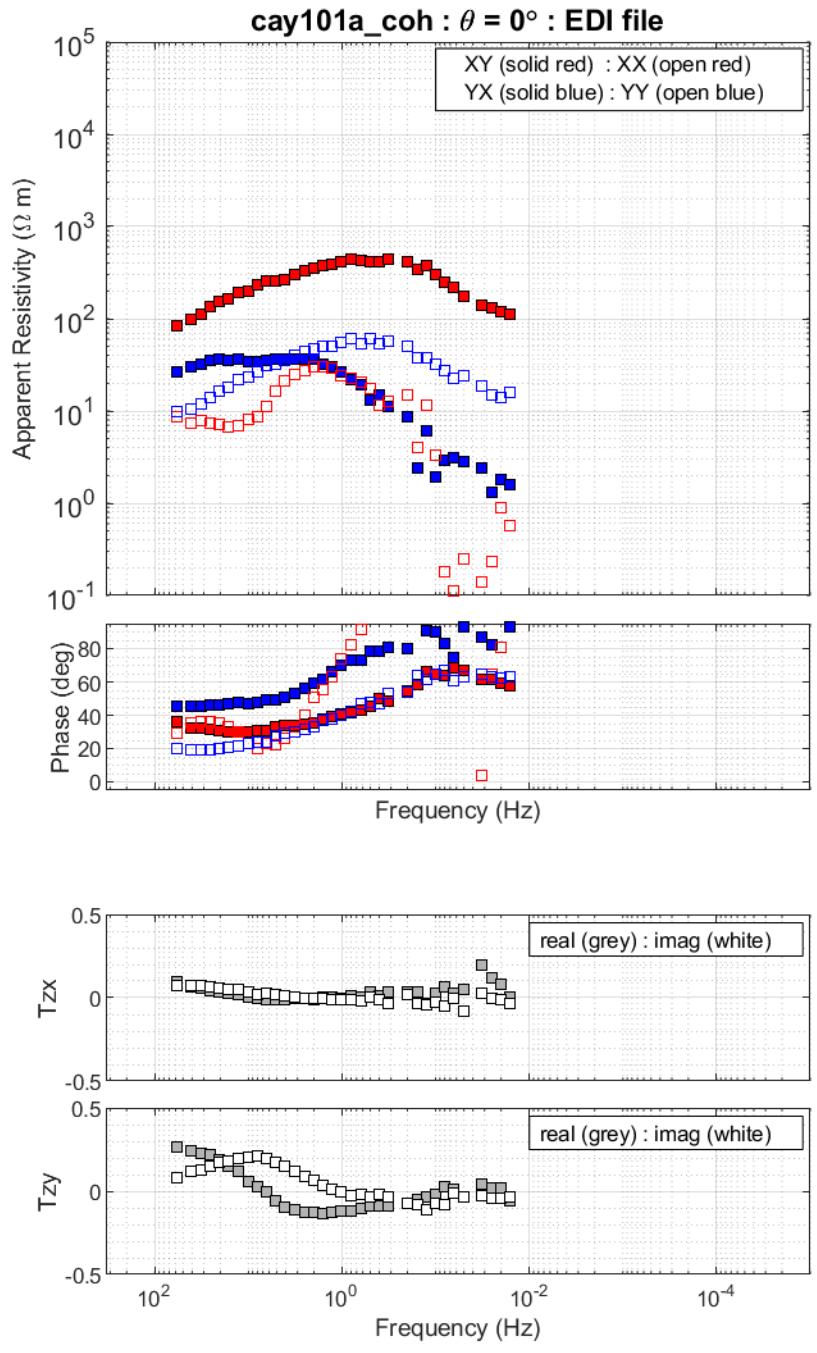


**Figure 5(b).** Apparent resistivity, phase and tipper at station CAY101.

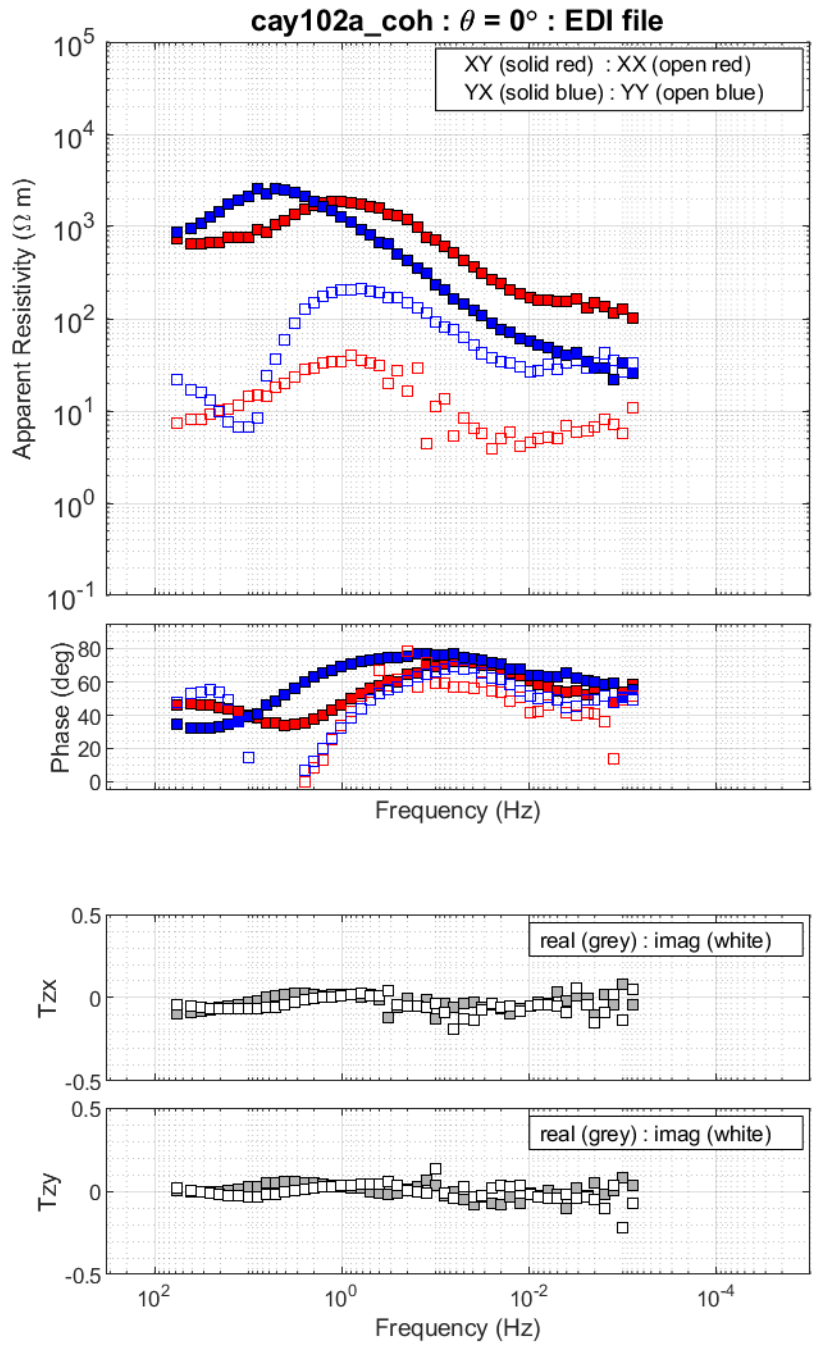


**Figure 5(c).** Apparent resistivity, phase and tipper at station CAY102.

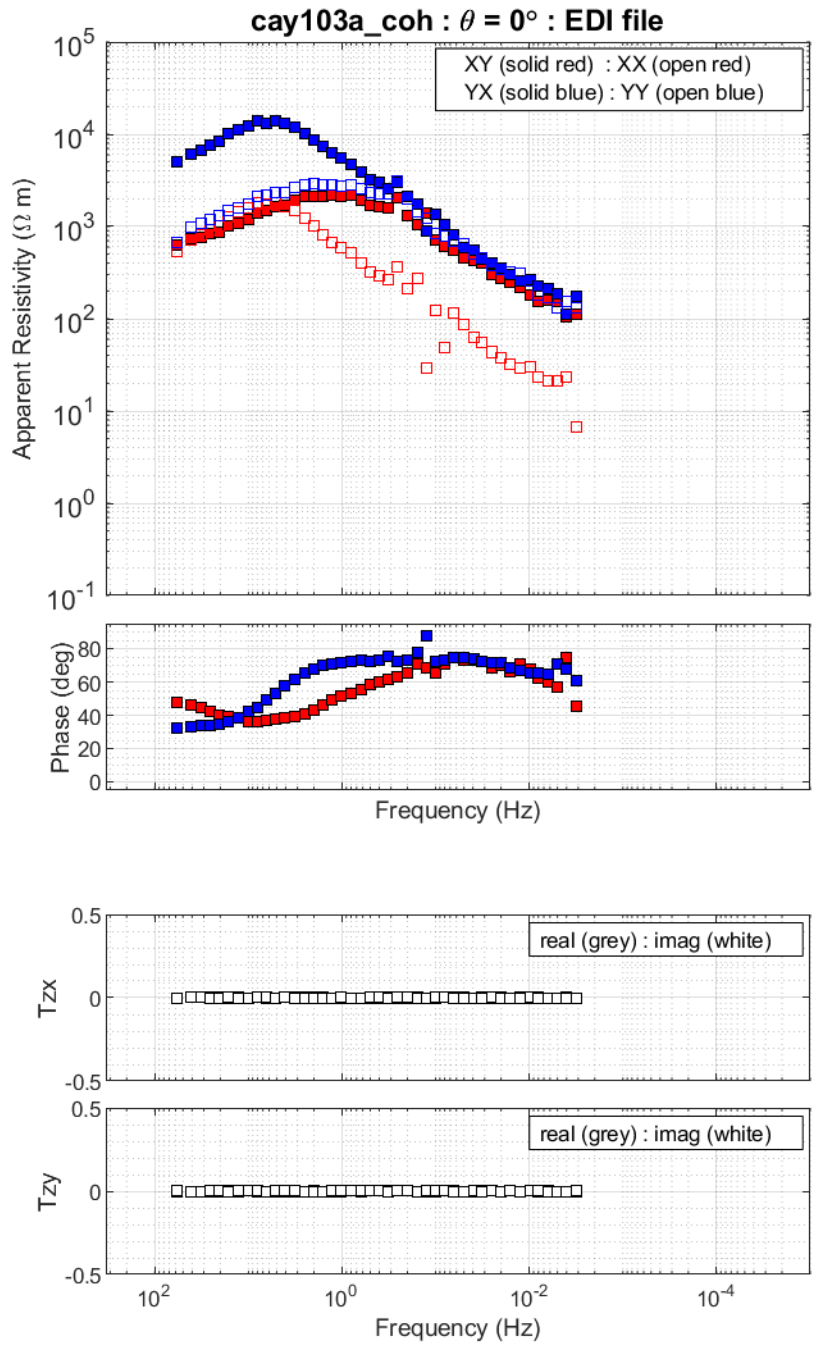


**Figure 5(d).** Apparent resistivity, phase and tipper at station CAY103. No tipper data were collected at this location owing to rocky ground conditions. See Jones and Dumas (1993) for a historical perspective on this issue.

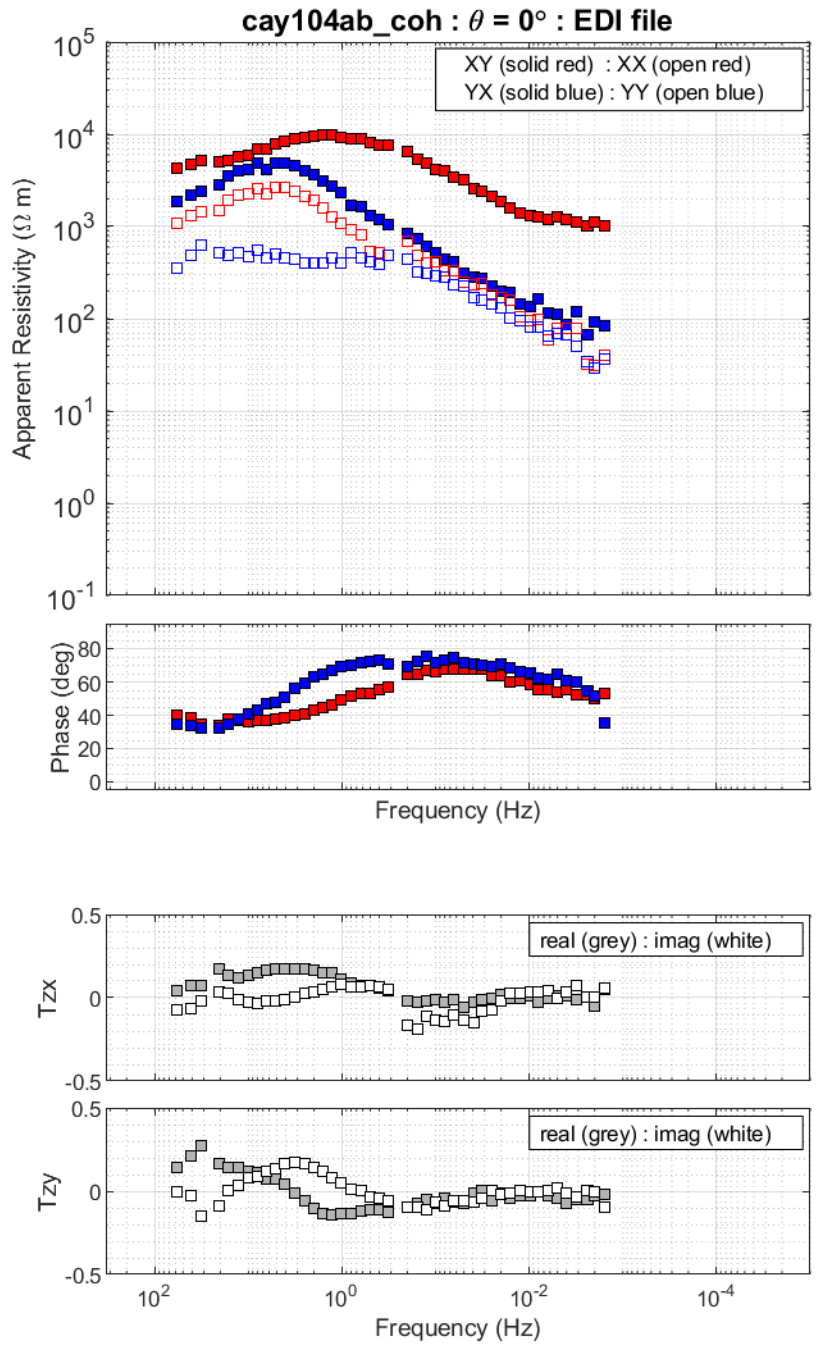


**Figure 5(e).** Apparent resistivity, phase and tipper at station CAY104. This response is the sum of run 'A' and run 'B'.

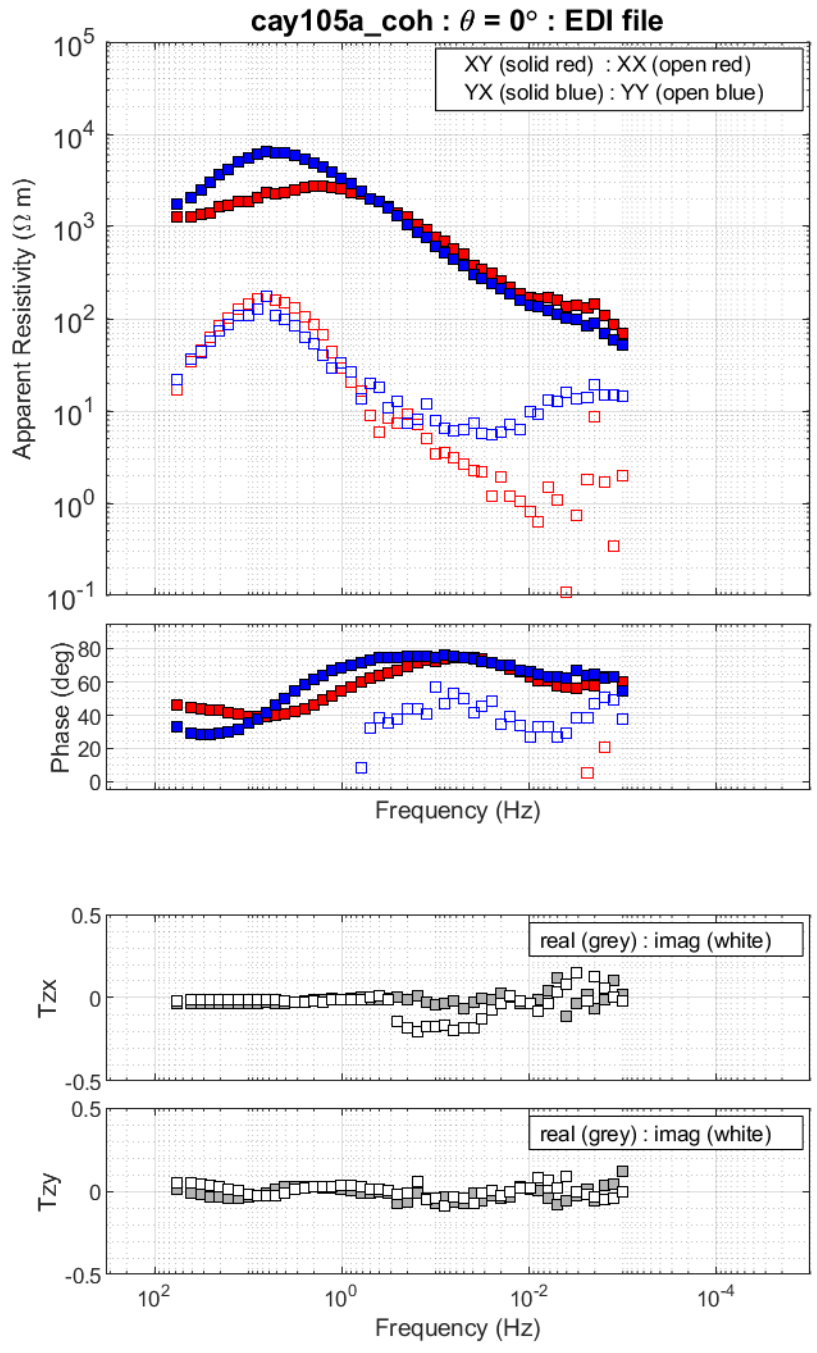


**Figure 5(f).** Apparent resistivity, phase and tipper at station CAY105.

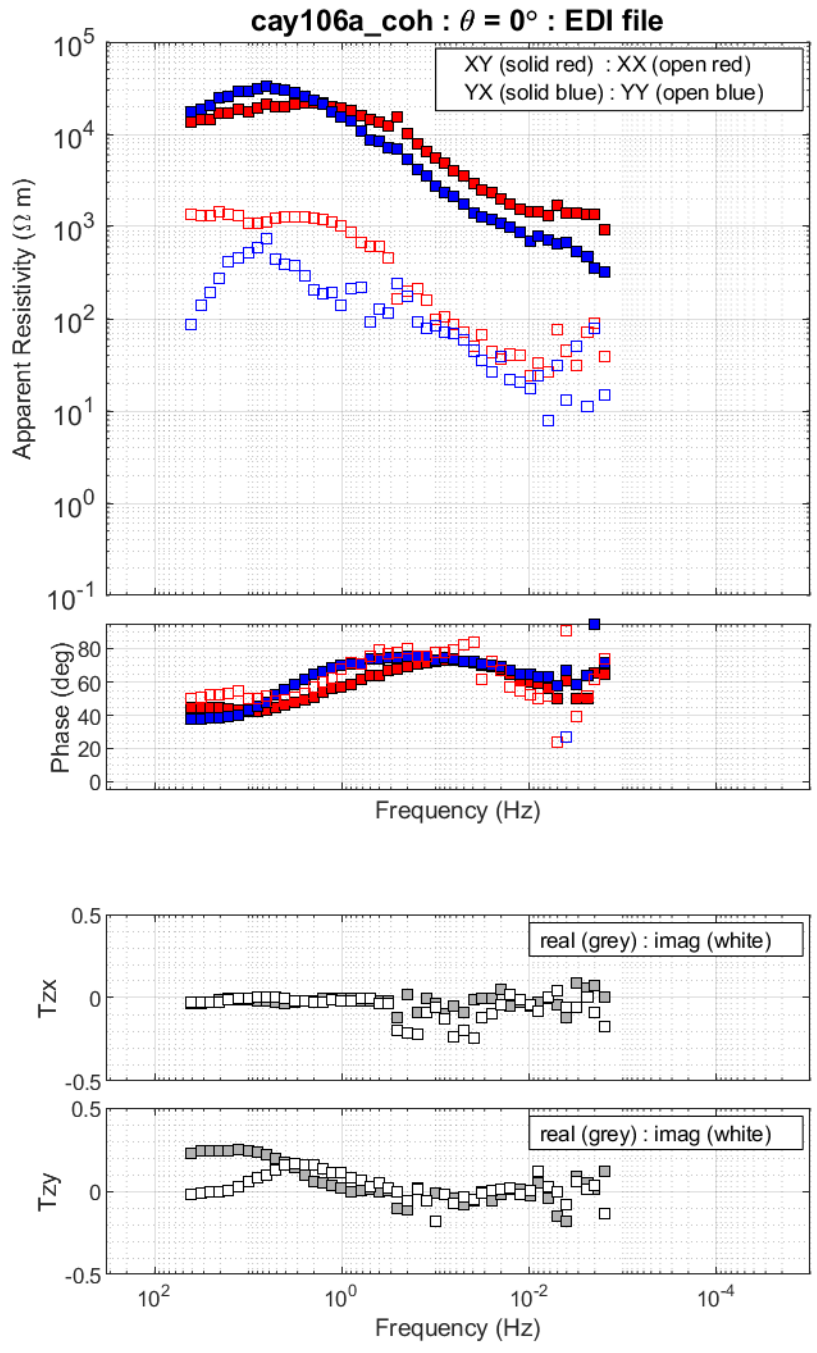


**Figure 5(g).** Apparent resistivity, phase and tipper at station CAY106.

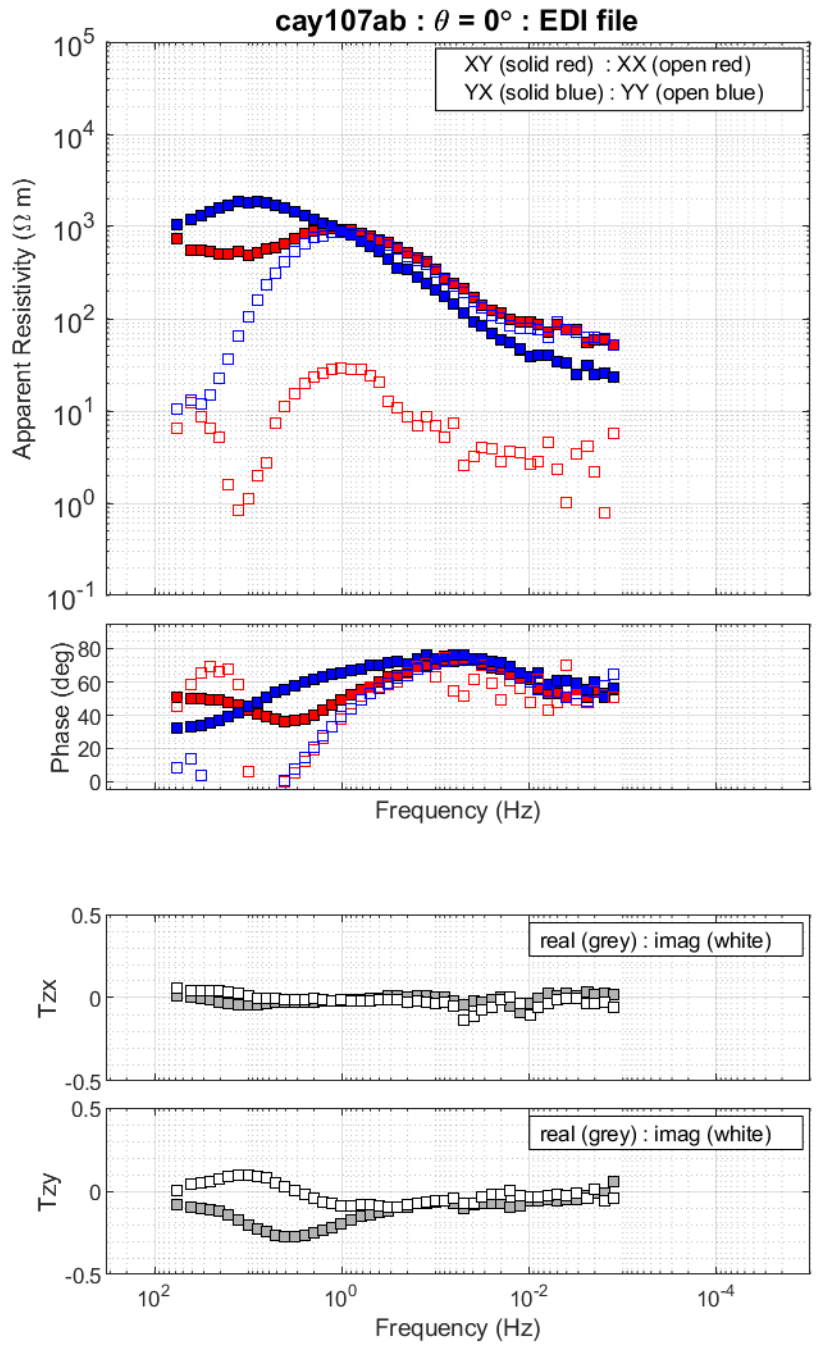


**Figure 5(h).** Apparent resistivity, phase and tipper at station CAY107. This response is the sum of run 'A' and run 'B'.

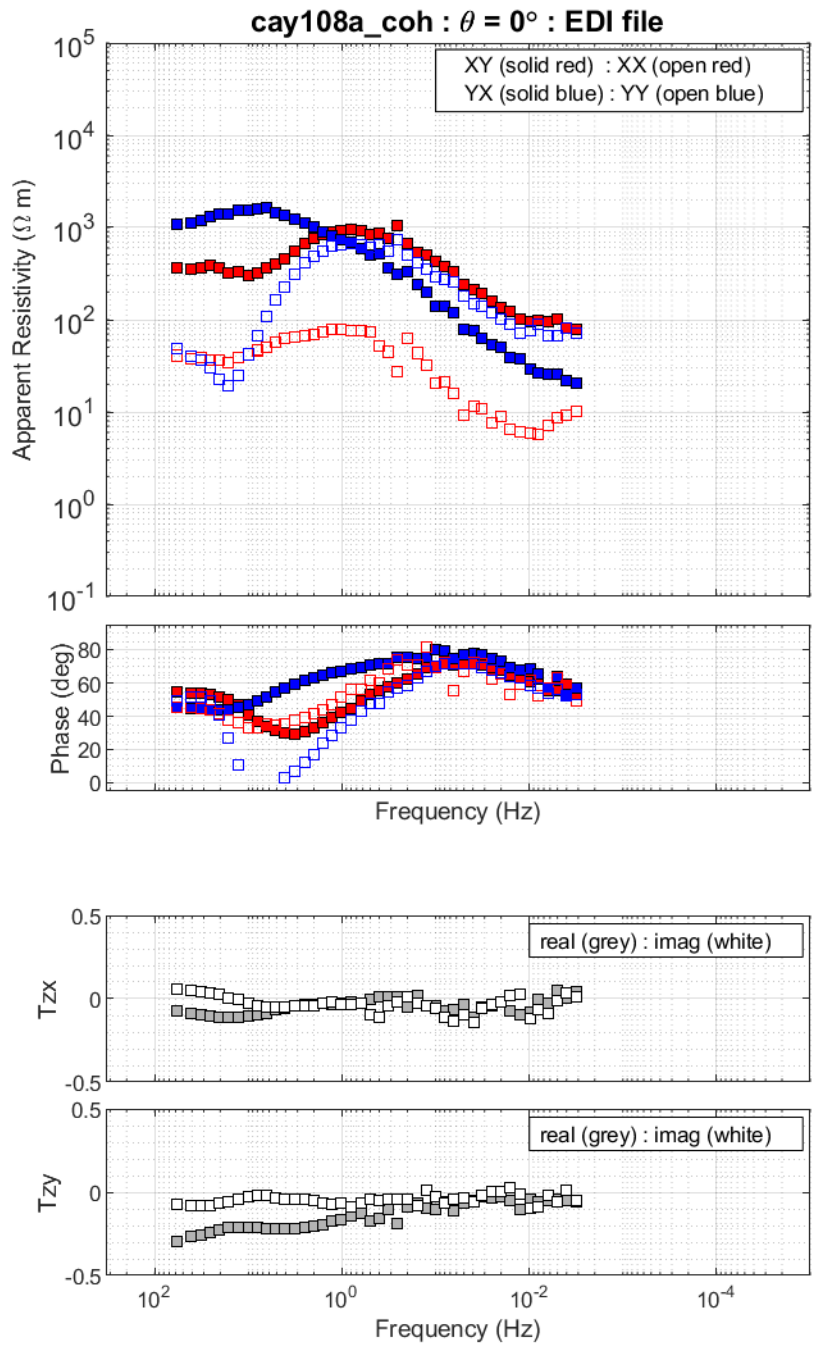


**Figure 5(i).** Apparent resistivity, phase and tipper at station CAY108.

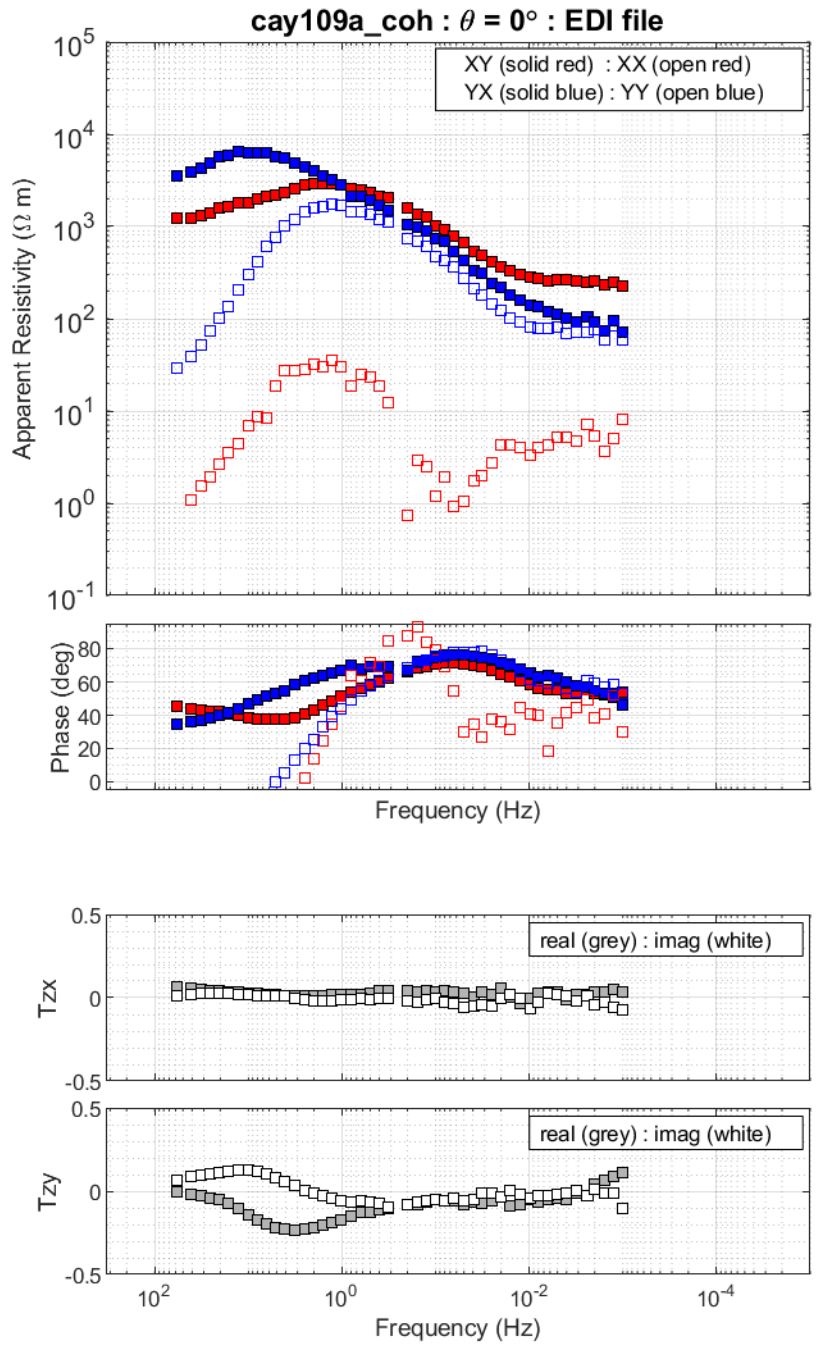


**Figure 5(j).** Apparent resistivity, phase and tipper at station CAY109.

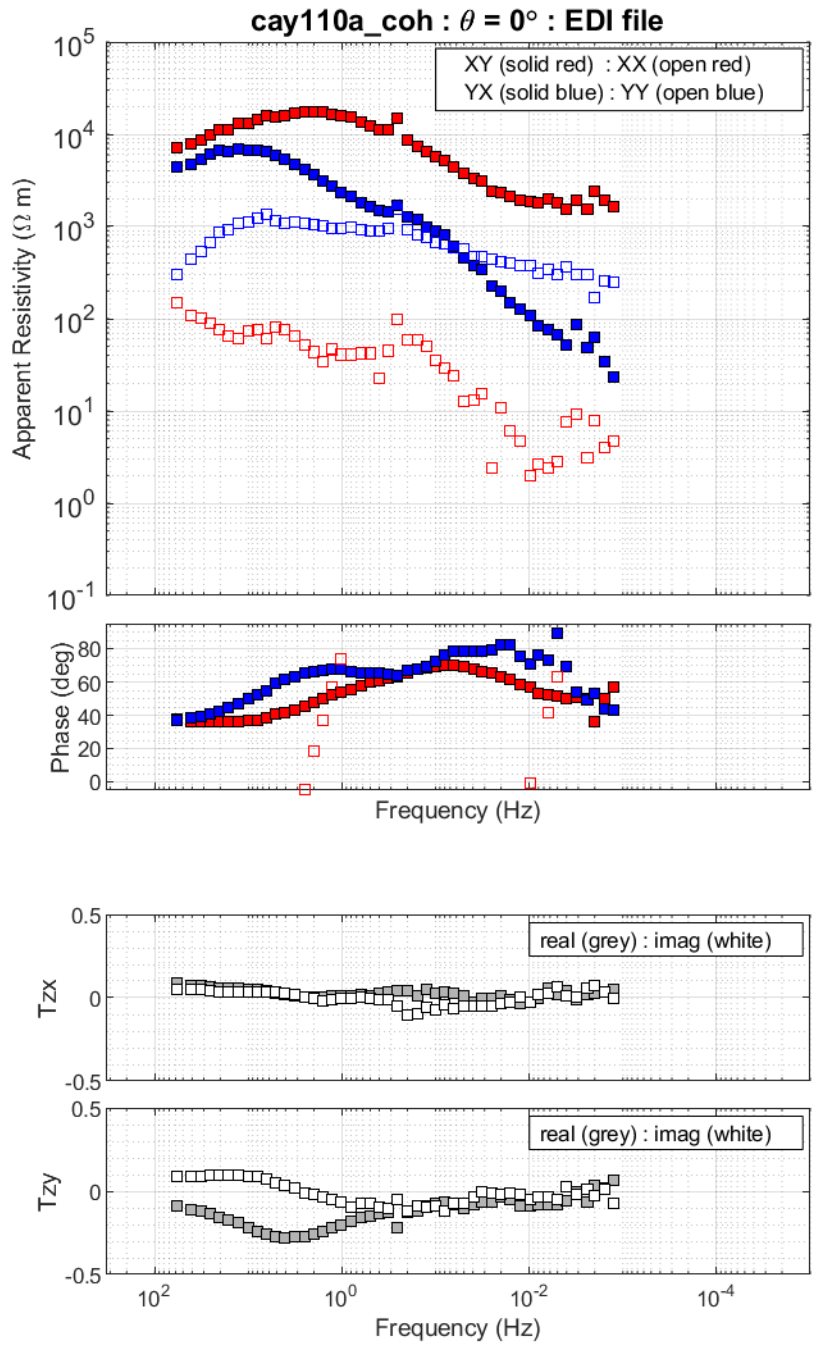


**Figure 5(k).** Apparent resistivity, phase and tipper at station CAY110.

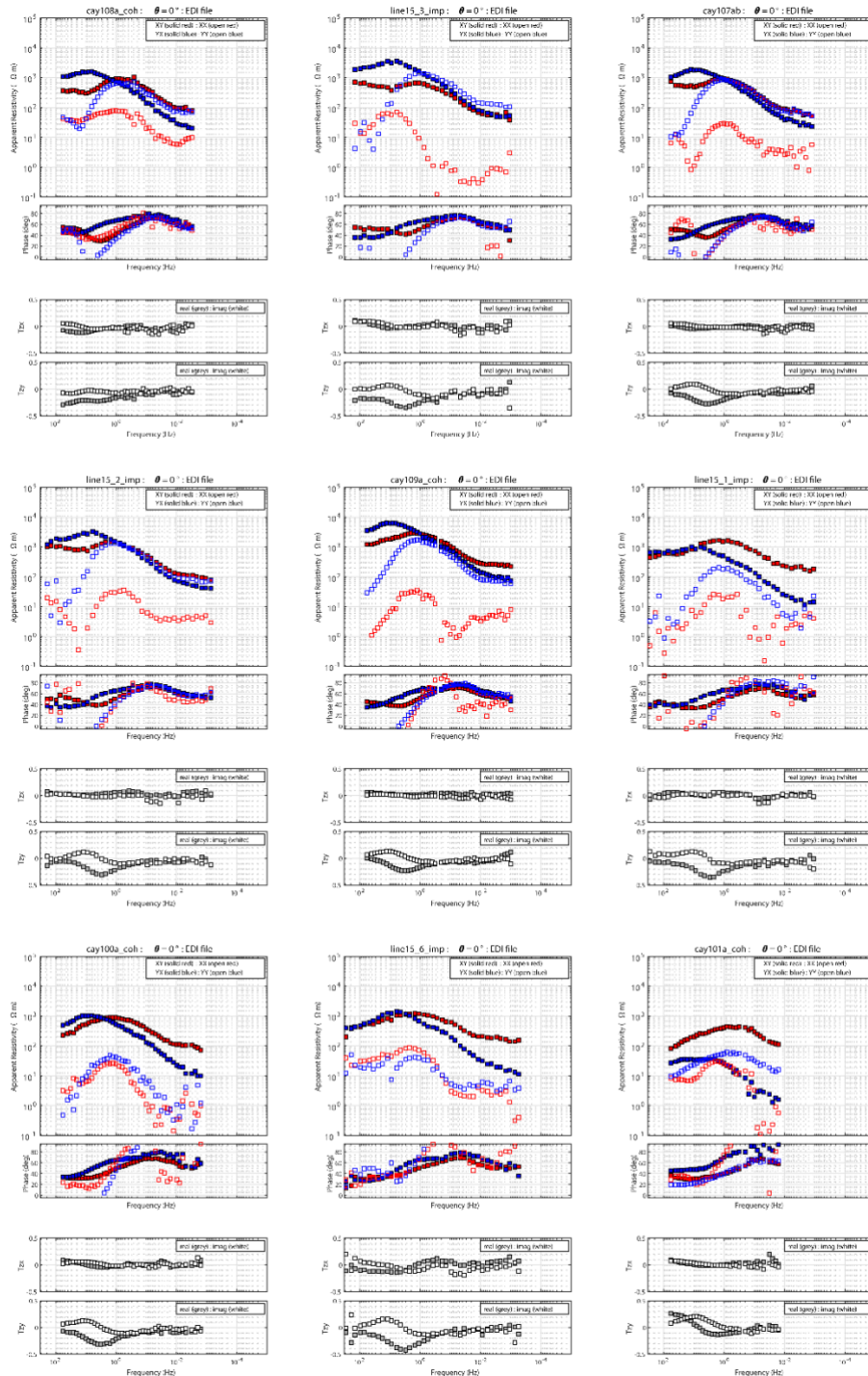


**Figure 6.** Comparison of 2021 MT data collected in the Squamish Valley with Lithoprobe MT data collected in the 1980s. Note the site-to-site consistency of the data. Locations are shown in Fig. 4. Top-left to bottom-right corresponds to north – south along the valley.

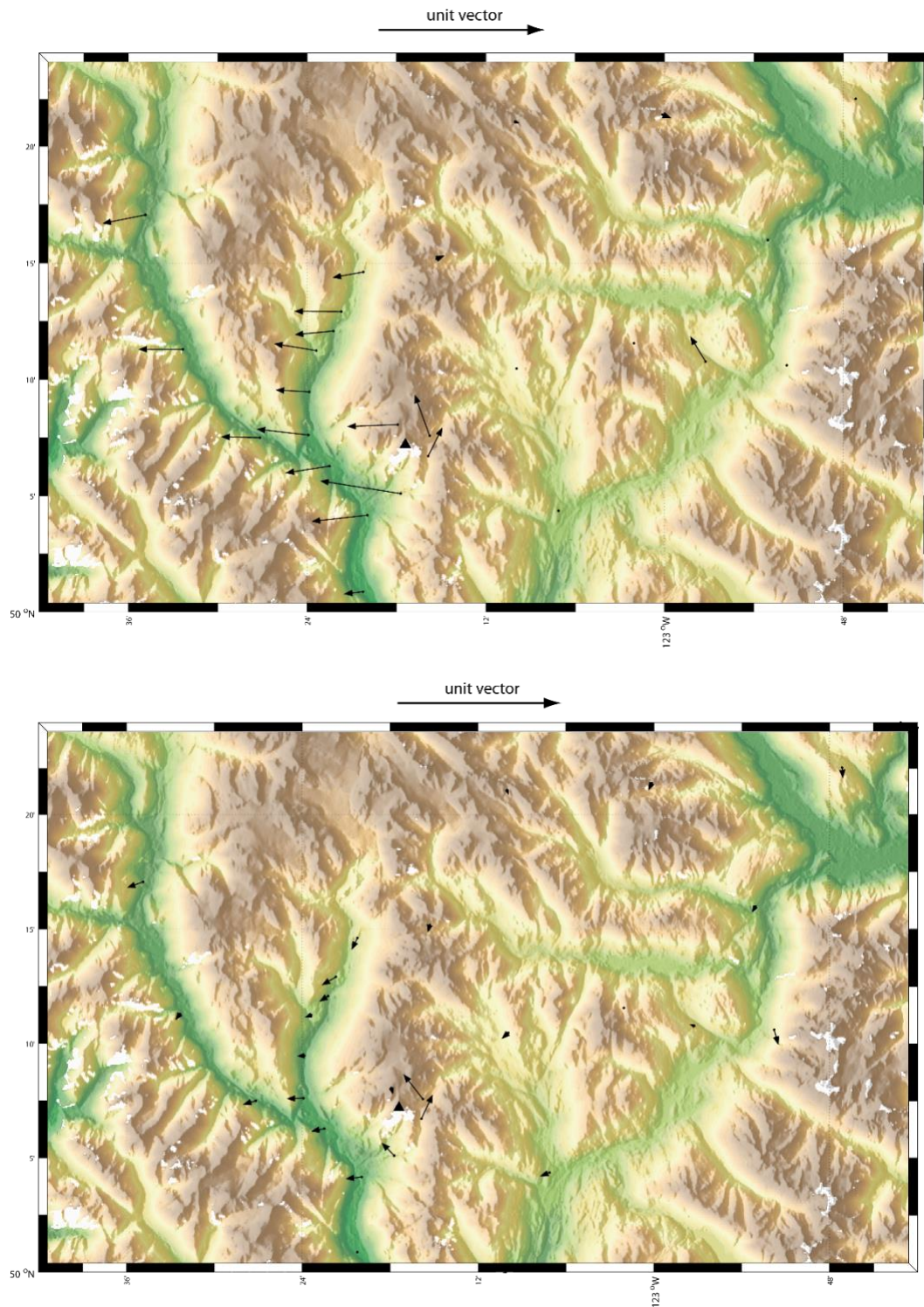


**Figure 7.** Maps of induction vectors collected in the Mount Cayley area. Real components are plotted in the Weise convention, so they point away from conductors. (a) shows data at a frequency of 2 Hz and (b) shows data at a frequency of 0.01 Hz. Broadband MT data from the Lithoprobe project in the 1980s and long-period MT data collected by the University of Alberta in 2019 are also shown. Scale is shown by the unit vector.

## References

- Arnason K, The Static Shift problem in MT Soundings, Proceedings of the World Geothermal Congress, Melbourne, Australia, 19-25 April 2015
- Candy C, Crew Development Corporation report on a magnetotelluric survey : South Meager Geothermal Project, Pemberton, British Columbia, Frontier Geosciences project FG1-581, 2001.
- Clague JJ and Souther JG, The Dusty Creek landslide on Mount Cayley, British Columbia, Canadian Journal of Earth Sciences, 19, 524-539, 1982.
- Comeau M, MJ Unsworth, F Ticona, M Sunagua, Magnetotelluric images of magma distribution beneath Volcan Uturuncu, Bolivia : Implications for magma dynamics, *Geology*, 43(3), 243-246, 2015.
- Cordell DR, MJ Unsworth, and D Diaz, Imaging the Laguna del Maule Volcanic Field, central Chile using magnetotellurics: Evidence for crustal melt regions laterally-offset from surface vents and lava flows, *Earth and Planetary Science Letters*, 488, 168-180, 2018.
- Egbert GD, and J. R. Booker, Robust estimation of geomagnetic transfer functions, *Geophysical Journal of the Royal Astronomical Society*, 87, 173-194, 1986.
- Evans SG, Hungr O, Clague JJ, Dynamics of the 1984 rock avalanche and associated distal debris flow on Mount Cayley, British Columbia, Canada; implications for landslide hazards assessment on dissected volcanoes, *Engineering Geology*, 61, 29-51, 2001.
- Eysteinnsson H, K Arnason and OG Flovenz, Resistivity methods in geothermal prospecting in Iceland, *Surveys in Geophysics*, 15, 263-275, 1994.
- Flores-Luna CF, Electromagnetic induction studies over the Meager Creek Geothermal Area, British Columbia: Research in Applied Geophysics No. 37, University of Toronto, 1986
- Gamble TB, WM Goubau, J Clarke, Magnetotellurics with a remote reference, *Geophysics*, 44, 53-68, 1979
- Grasby SE, Ansari SM, Calahorrano A, Chen Z, Craven JA, Dettmer J, Gilbert H, Hanneson C, Harris M, Liu J, Muhammad M, Russell JK, Salvage RO, Savard G, Tschirhart V, Unsworth MJ, Vigouroux-Caillibot N, Williams-Jones, G, Geothermal Resource Potential of the Garibaldi Volcanic Belt, Southwestern British Columbia (Part of NTS 092J). Geoscience BC Summary of Activities 2019:103-108, 2020.
- Grasby SE, Ansari SM, Barendregt RW, Borch A, Calahorrano A, Chen Z, Craven JA, Dettmer J, Gilbert H, Hanneson C, Harris M, Hormozzade F, Leiter S, Liu J, Muhammad M, Quane SL, Russell JK, Salvage RO, Savard G, Tschirhart V, Unsworth MJ, Vigouroux-Caillibot N, Williams-Jones G, Williamson AR and Vestrum ZE, Garibaldi Geothermal Energy Project – Phase 1 : Final report, Geoscience BC Report 2021-08, 2021.
- Green NL, Armstrong RI, Harakal JE, Souther JG, Read PB, Eruptive history and K-Ar geochronology of the late Cenozoic Garibaldi Belt, southwestern British Columbia, *GSA Bulletin*, 100, 563-579, 1988.
- Guthrie RH et al., The 6 August 2010 Mount Meager rock slide-debris flow, Coast Mountains, British Columbia: characteristics, dynamics, and implications for hazard and risk assessment, *Nat. Hazards Earth Syst. Sci.*, 12, 1277–1294, 2012
- Jones, A.G., and I. Dumas, Electromagnetic images of a volcanic zone, *Physics of the Earth and Planetary Interiors*, 81, 289-314, 1993.
- Kelbert A, N Meqbel, GD Egbert, K Tandon, ModEM : A modular system for inversion of electromagnetic geophysical data, *Computers and Geosciences*, 66, 40-53, 2014.
- Munoz G, Exploring for Geothermal Resources with Electromagnetic Methods, *Surveys in Geophysics*, 35, 101-122, 2014.

- Pellerin L, JM Johnston and GW Hohmann, A numerical evaluation of electromagnetic methods in geothermal exploration, *Geophysics*, 61, 121-130, 1996.
- Pham van Ngoc, Magnetotelluric reconnaissance survey in the Lilloet Valley, BC, Earth Physics Branch Open File 77-20, Earth Physics Branch, Department of Energy, Mines and Resources, Ottawa, 40 pp., 1977.
- Pham van Ngoc, Magnetotelluric prospecting in the Mount Meager Geothermal Region, Earth Physics Branch Open File 78-6E, Earth Physics Branch, Department of Energy, Mines and Resources, Ottawa, 31 pp., 1978.
- Pham van Ngoc, Magnetotelluric survey of Mount Meager and the region of the Squamish Valley, Earth Physics Branch Open File 80-8E, Earth Physics Branch, Department of Energy, Mines and Resources, Ottawa, 77 pp., 1980.
- Shore GA, Deep Resistivity Surveys and Supplementary Geophysics at Meager Creek selected area, Pemberton BC, report prepared for British Columbia Hydro and Power Authority, report G.T. 4, 1975
- Shore GA, Report on DC resistivity survey in the Meager Creek Geothermal Area 1980, report prepared for British Columbia Hydro and Power Authority, report G.T. 26, 1981.
- Simpson F and K Bahr, *Practical magnetotellurics*, Cambridge University Press, 2005.
- Spichak V and A Manzella, Electromagnetic sounding of geothermal zones, *Journal of Applied Geophysics*, 68, 459-478, 2009.
- Vozoff K, The magnetotelluric method, in *Electromagnetic Methods in Applied Geophysics*, Vol2B 641-711, Society of Exploration Geophysicists, 1991.

# Chapter 6 – Ground Temperature Data and Fracture System Analyses of the Mount Meager and Mount Cayley Areas

Chen, Z., Grasby, S.E., Yuan W.

Geological Survey of Canada – Calgary, Calgary, AB, Canada

## Introduction

A two-week field campaign was conducted in the Mount Meager and Mount Cayley areas during the period of August 17-30, 2021, to conduct geological and fracture studies. The main objectives of the study were: a) ground temperature data collection for improving the understanding of the geothermal heat flux and hydrothermal systems in prospective geothermal areas; b) to understand better the fracture systems in the Mount Cayley area; and c) to test new methods and apply potential geoscience indicators learned from the south Mount Meager geothermal area to the Mount Cayley area. The specific aim of the 2021 fieldwork was to collect geological and other relevant data for evaluation of geothermal resource potential in the volcanic belt with following tasks:

- A) retrieving ground temperature data from loggers deployed in southern Mount Meager in 2020;
- B) re-deploying ground temperature loggers using improved layout for better data collection in southern Mount Meager;
- C) deploying ground temperature loggers with improved layout in Mount Cayley;
- D) measuring fracture attributes, such as strike, dip direction, dip angle, spacing/density, for fracture characterization in the Mount Cayley area;
- E) collecting samples in logger sites (soil) and basement outcrop observation sites (rock) to obtain thermal-physical parameters (porosity, permeability and density, thermal conductivity, thermal capacity and enthalpy); and
- F) collecting geological evidence and indicative features of geothermal anomalies in the Mount Cayley volcanic complex.

## Methods

In situ measurement of ground temperature was made using miniature temperature data loggers (HOBO Water Temp Pro v2). The temperature data logger is waterproof, and has precision of 0.2 °C and temperature ranging from -40 to 70 °C in air and up to 50 °C in water. In the 2020 deployment, a single HOBO temperature logger was buried in soil approximately at 1 to 7 cm depth from the ground surface to avoid direct exposure to the solar radiance. For each site, a soil sample was taken for laboratory analysis to examine its physical and thermal properties. In the field, we used a shadiness index (SI) to quantify the impact of vegetation canopy or topographic feature on ground surface temperature. The SI has a value between 0 to 1, from direct exposure to completely shielded from solar radiance.

Re-deployment of the monitoring network was made at the same locations with an improved configuration in the 2021 field season, in which two HOBO temperature loggers were buried at the same site ranging 30-50 cm apart vertically depending on the ground condition. The newly deployed loggers will be retrieved in the next fieldwork season in 2022. The deployment of the ground surface temperature (GST) monitoring network in southern Mount Meager area is aimed to investigate the use of a GST monitoring system as a cost-effective tool for geothermal exploration. The geothermal heat flow data from temperature wells in the South Meager prospect can be used to validate the observations and interpretations.

A thermal infrared camera was used to take temperature images of various objects, ground-surface cover and water bodies for calibration of Landsat converted land surface temperature (LST), as well as for identifying GST anomalies, particularly for the area with groundwater seeps. Fig. 1 compares the temperature image captured by the thermal infrared camera and the true colour photo to show the usefulness of the new tool in the field study for identifying ground temperature anomalies.

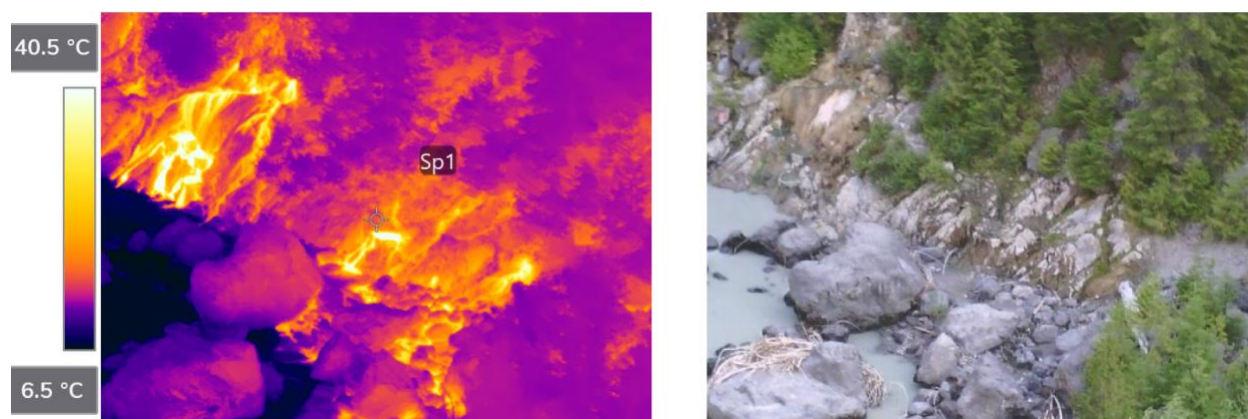


**Figure 1.** Comparison of the temperature image from thermal infrared camera and true colour image of Pebble Creek Hot Spring in Mount Meager Volcanic Complex, showing the water temperature of 6.5 °C in Lillooet River, and 40.5 °C of the water from the pools of Pebble Creek Hot Spring, demonstrating the usefulness of temperature image for identifying ground temperature anomalies. (Recorded maximum Temperature is 45.9 °C and minimum 6 °C). Photo taken from helicopter about 500 m above ground level.

Outcrop geological examination and fracture measurement followed traditional field methods in the Mount Caley area. The field party observed, identified and recorded geological and geomorphologic features, measured fracture attitudes (strike, dip direction, dip angle, density and spacing) and fault planes, and collected rock samples for laboratory analysis. The identified geological and geomorphologic features and evidence of geological processes were analyzed in relation to tectonic and volcanic activities of the region and to assess their association to potential reservoir development in and around each station. Photos were taken at the outcrops where well exposed fracture traces are present for statistical characteristics of fracture spacing and density.

## Data Collection

Ground surface temperature data from 22 data loggers were retrieved for data in the south Meager geothermal prospect area (Fig. 2). Table 1 provides general information of the monitoring stations and basic statistics of the retrieved data; the raw data are presented in Appendix A. Fourteen shallow-deep coupled dual logger pairs were deployed in the Mount Cayley area (Fig. 3, Table 2). The data logger will be retrieved for analysis in the next field season in 2022. Soil samples were taken at each logger station in both areas for laboratory analysis (Table 3).

We have made 30 stations for outcrop geological observation and fracture measurement (Table 4; Fig. 4) and taken 10 rock specimens for laboratory analysis in the Mount Cayley area. Depending on the bedrock exposure, we have 28 stations with fracture measurements (Table 4) and over 400 fracture planes were recorded (Appendix B); a number of photo images were also taken for statistical analysis of fracture traces to study the density and spacing quantitatively.



**Figure 2.** Google Earth map showing the location of the ground temperature monitoring stations in the southern Mount Meager area.

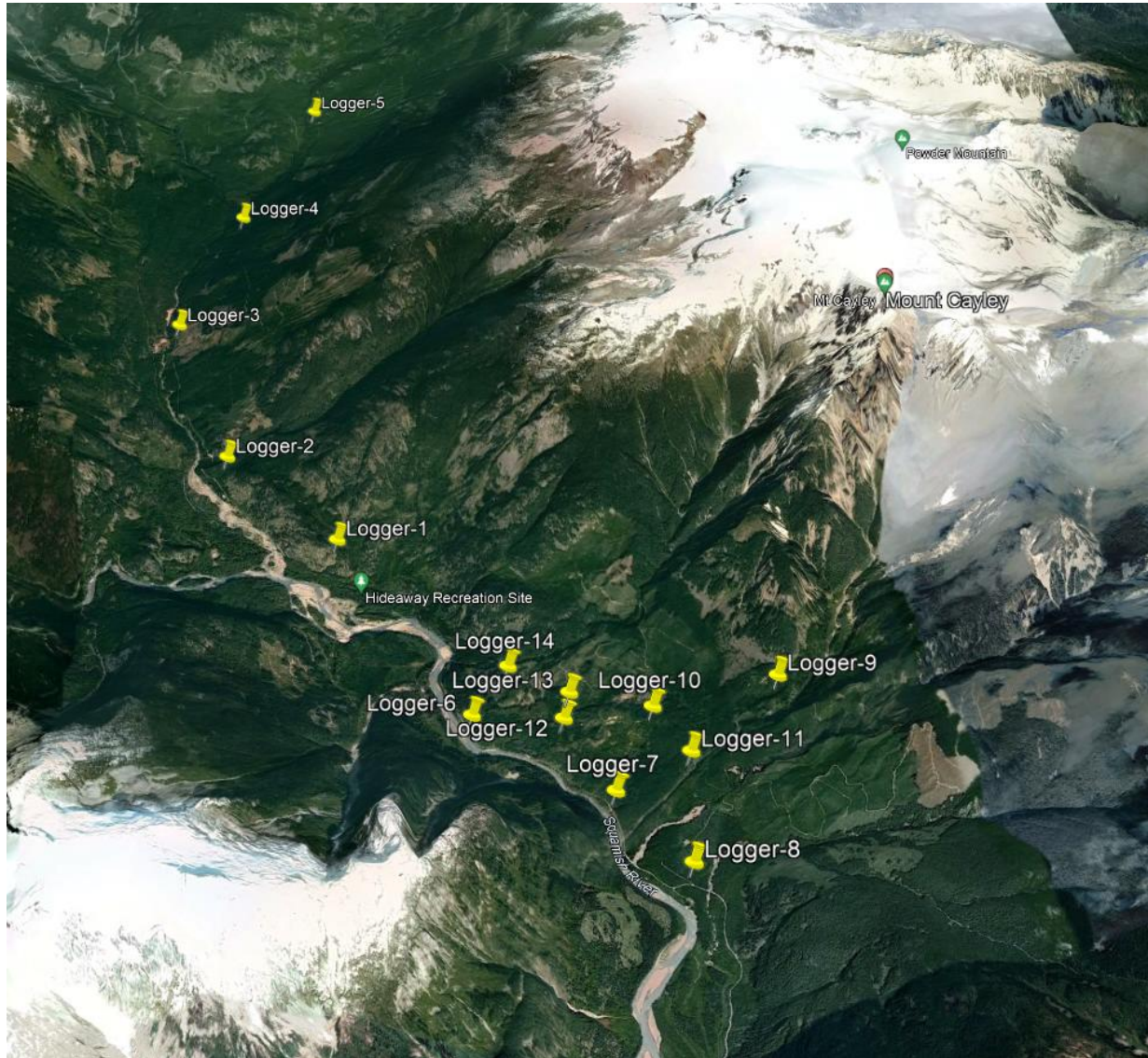


**Figure 3.** Google Earth map showing the location of the 14 deployed ground temperature monitoring stations in Squamish Valley of the Mount Cayley area.



around zero, snow cover (SC) with almost constant temperature slightly above zero, and snow melt (SM) with temperature about zero followed by a rapid increase in temperature. The length of each segment varies from station to station. There is no clear boundary between SC and SM because the latent heat of snowmelt absorbs heat.

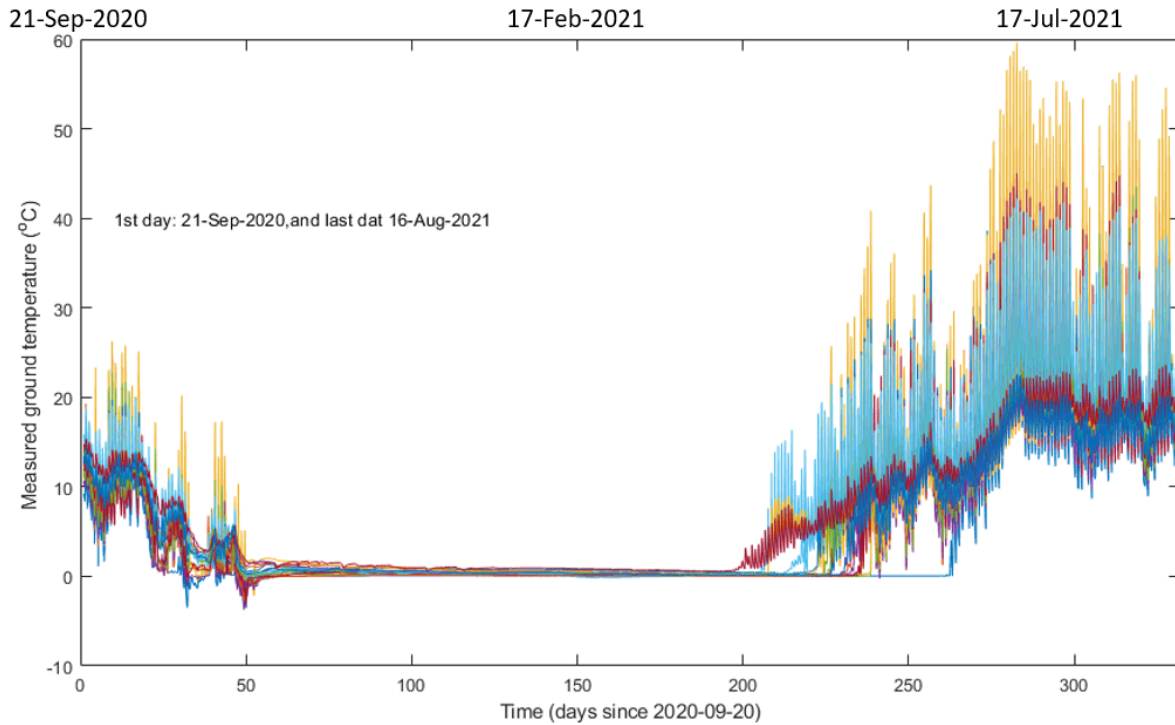


**Figure 5.** The year-long ground surface temperature time series recorded from 22 temperature loggers in the south Meager study area from 2020/09/21 to 2021/08/15. The colours reflect different data logger records. See Fig. 6 for interpretation of the different segments of the temperature records.

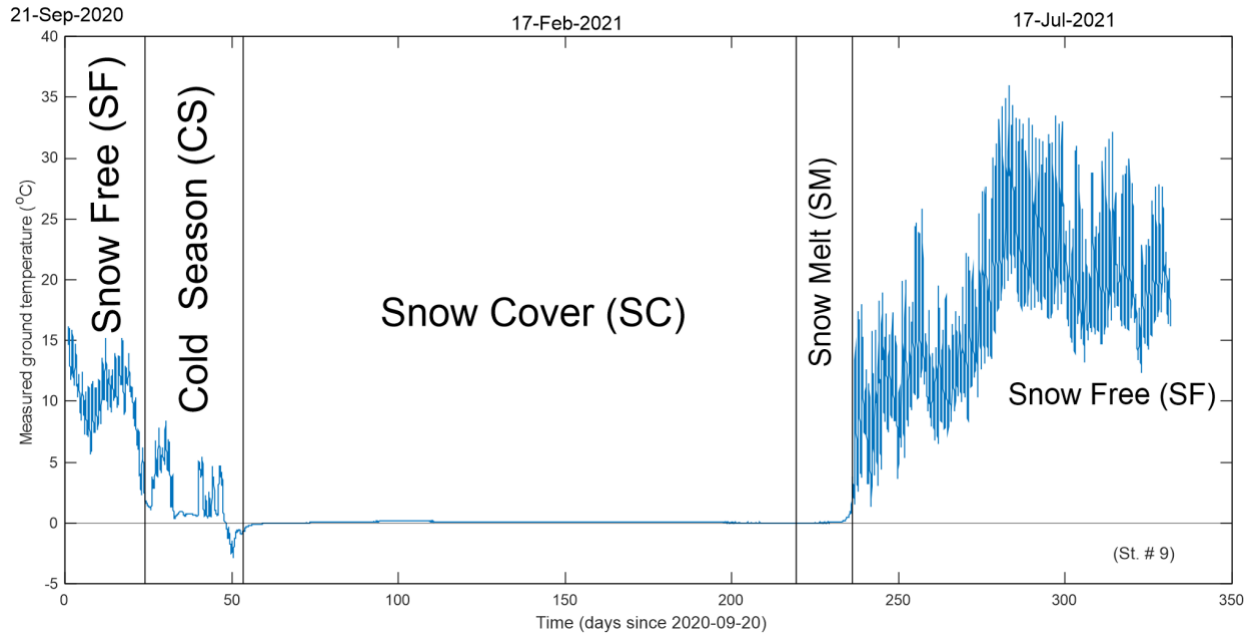


**Figure 6.** GST record example at station # 9. This example illustrates how the temperature time series is divided into four segments in response to seasonal variation, South Meager area.

To display the spatial variation of the recovered temperatures and special environmental conditions, the overall mean temperature, as well as the average values of temperature in the snow cover and snow free periods at the 22 stations are plotted in Figs. 7a to c. The measured soil moisture on the time of the data retrieval is shown in Fig. 7d.

The magnitude and intensity of daily GST fluctuations in the snow free season shows environmental footprints, and is complicated by burial depth and soil properties. The GST mean for the snow-free period shows a strong positive correlation with its standard deviation (STD), and the sites with the high STDs occurring in ground with bare gravel and low vegetation cover; this suggests that direct exposure to solar radiance is the major cause of daily high temperature fluctuations and high STD of the temperature time series. The vegetation cover (measured by shadiness index) has a negative correlation with Tmean and STD. Similar to SI, burial depth exhibits a negative correlation with GST mean.

Machine learning methods have been used for clustering the time series of the 22 temperature loggers. The hierarchical clustering (Davis, 2002) resulted in three groups with two separate clusters in space that are in coincidence with two distinct geothermal heat flow anomalies. One cluster is underlain by the convective flow disturbed zone in the core area of the geothermal prospect of the South Meager with high estimated heat flow (Lewis, et al., 1985); while the other is linked to the Meager Creek hot spring and warm water seeps in the southeastern Meager Creek (Lewis and Souther, 1978). The k-means method (Arthur and Vassilvitskii, 2009) was also applied to generate statistically similar classes in assisting data interpretation.

In the snow cover period, thick snow insulates ground from cold air temperatures, and filters out daily heat fluctuation from solar irradiation, resulting in a zero-curtain, in which the logger recovered a constant temperature slightly above zero. Differences in temperature and variation in the zero-curtain days reflect the variation in the subsurface geothermal flux. The average recorded temperature from the stations forms two high temperature anomalies. The two high anomaly stations are spatially coincident with the clustering results from the machine learning methods. Similarly, the days in the zero-curtain periods display two short day clusters, consistent with the average temperature in the zero-curtain period. Since the thick snow cover greatly suppresses the impacts from solar irradiation, the differences in recovered temperature variation in monitoring stations provide useful information on geothermal heat flux. As a comparison to the solar energy flux on the Earth surface, geothermal heat flux accounts for less than 0.1% on average (Pollack, et al., 1993; Tsao, et al., 2003). This suggests that at times of higher solar heat flux that ground surface temperatures variations are greatly overwhelmed. The spatial variation of GST can provide meaningful clues for characterizing the geothermal heat flux when snow-covered however. Chen et al. (submitted for publication) provides more detail on the data interpretation and implications to geothermal exploration using the GST monitoring data.

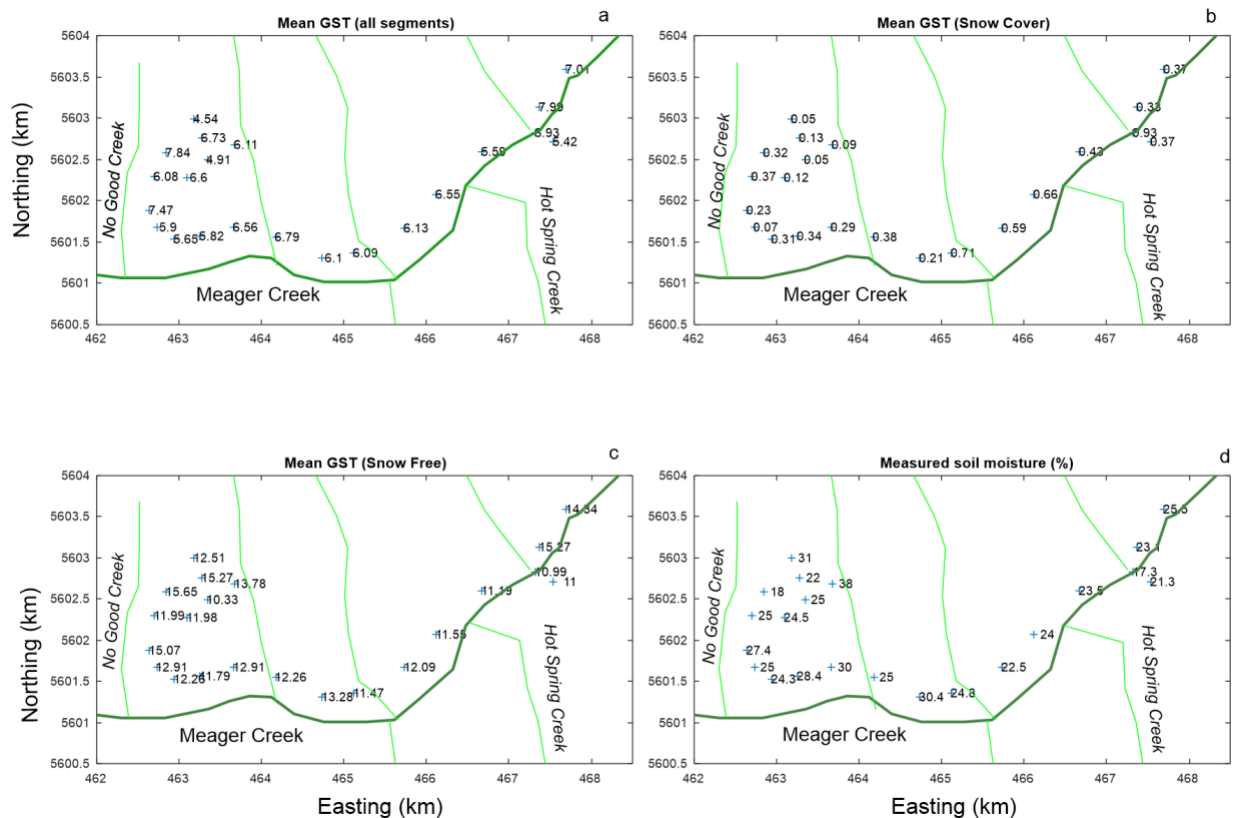


**Figure 7.** Spatial variation of the overall mean temperature, as well as the average values of temperature in the snow cover and snow free periods at the 22 stations (a to c). The measured soil moisture on the time of the data retrieval (d).

## Field Fracture Data Analysis

The fracture stations are located on both sides of Mount Cayley, on the eastern side in the Callahan Creek valley and the western side the Squamish River valley (Fig. 4). The measured fracture attitudes and occurrence vary greatly from station to station, as well as to the location relative to Mount Cayley. Fig. 8 shows the projection of measured fracture planes in the eastern side of the Squamish River in Stations 15 to 21 (Fig. 4), showing three fracture groups: a) NE striking and dipping toward SW; b) NW striking and dipping NE with a low dipping angle; and c) NE striking and NW dipping, although a few scattered fractures also occur. In the Callahan Creek area, the fracture occurrence is more complex as shown in Fig. 9 from Stations 4, 5, and 26.

Figs. 9 and 10 are stereonet plots and pole projection plots for measured fracture planes illustrating the variation in fracture abundance and attitudes. The measured attitudes are listed in Appendix B. Interpretation of the measured fractures under a regional geological context will be made when more surface geological data and information becomes available.

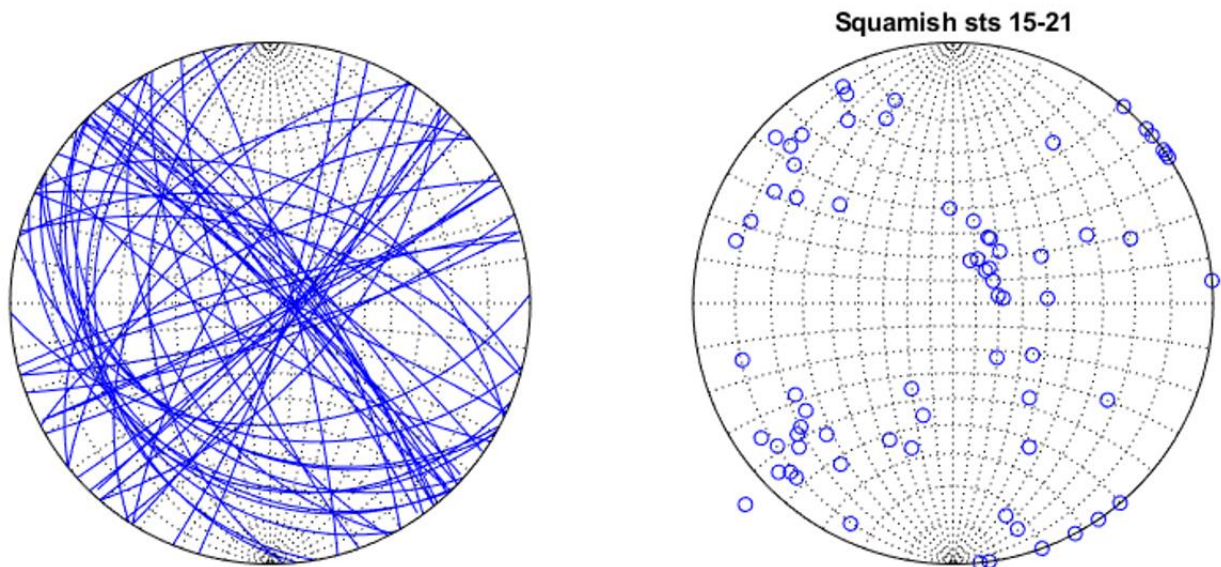


**Figure 8.** Stereonet plot of fracture planes (left) and projected poles of the fracture planes on stereonet (right) in stations from Stations 15-21 eastern side along the Squamish River.

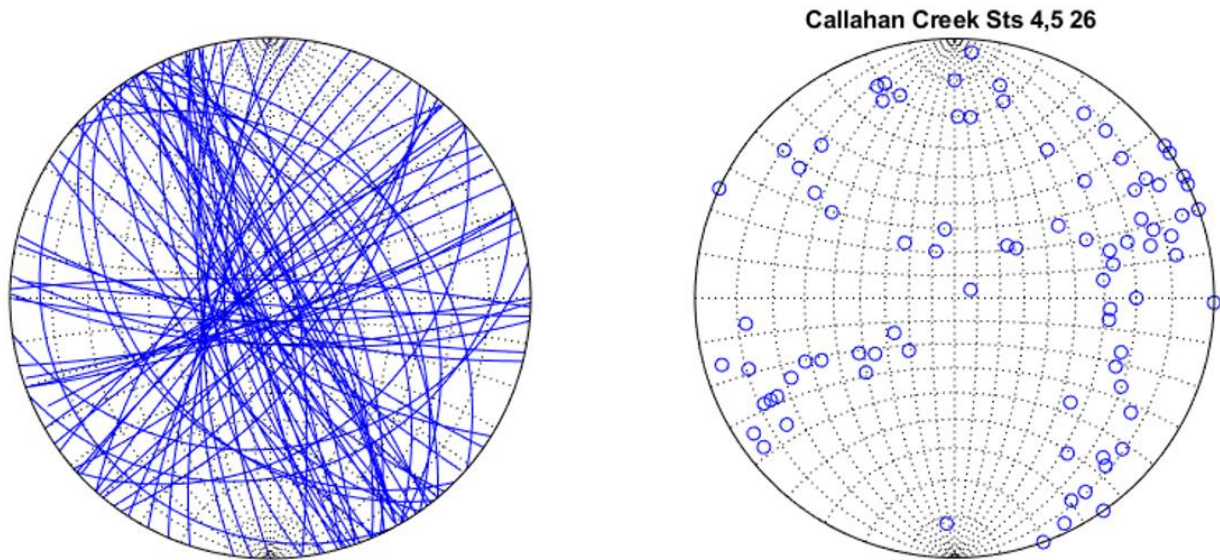


**Figure 9.** Stereonet plot of fracture planes (left) and projected poles of the fracture planes on stereonet (right) in stations from Stations 4, 5, 26 in the Callahan Creek area.

Rock and soil samples will be sent to laboratories for different analyses and tests. Two major categories of analysis are considered at this time: a) petrology, such as type and characteristics of the rock (thin section and mineral composition); and b) petrophysical and thermal properties of the rock, such as density, permeability, porosity, thermal conductivity and heat capacity. The results will be released as a Geological Survey of Canada Open File when the analysis and tests are completed.

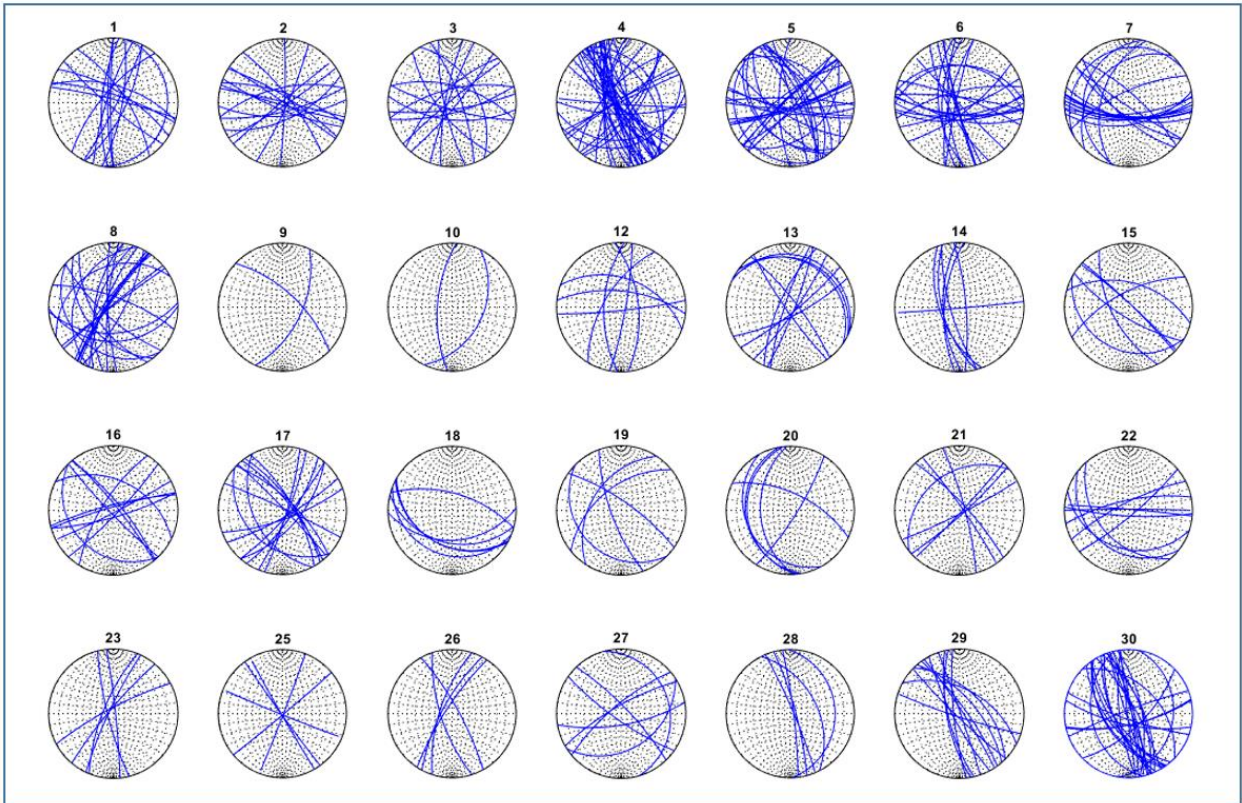


**Figure 10.** Equal angle stereonet plots of measured fracture strikes at different stations. The plots show the variation of strikes of fracture planes from different stations. The number above the net is the station number. Stations 1 to 11 and 23 to 30 were measured in the Callahan Creek area, Station 12 to 22 were in the Squamish River drainage area.

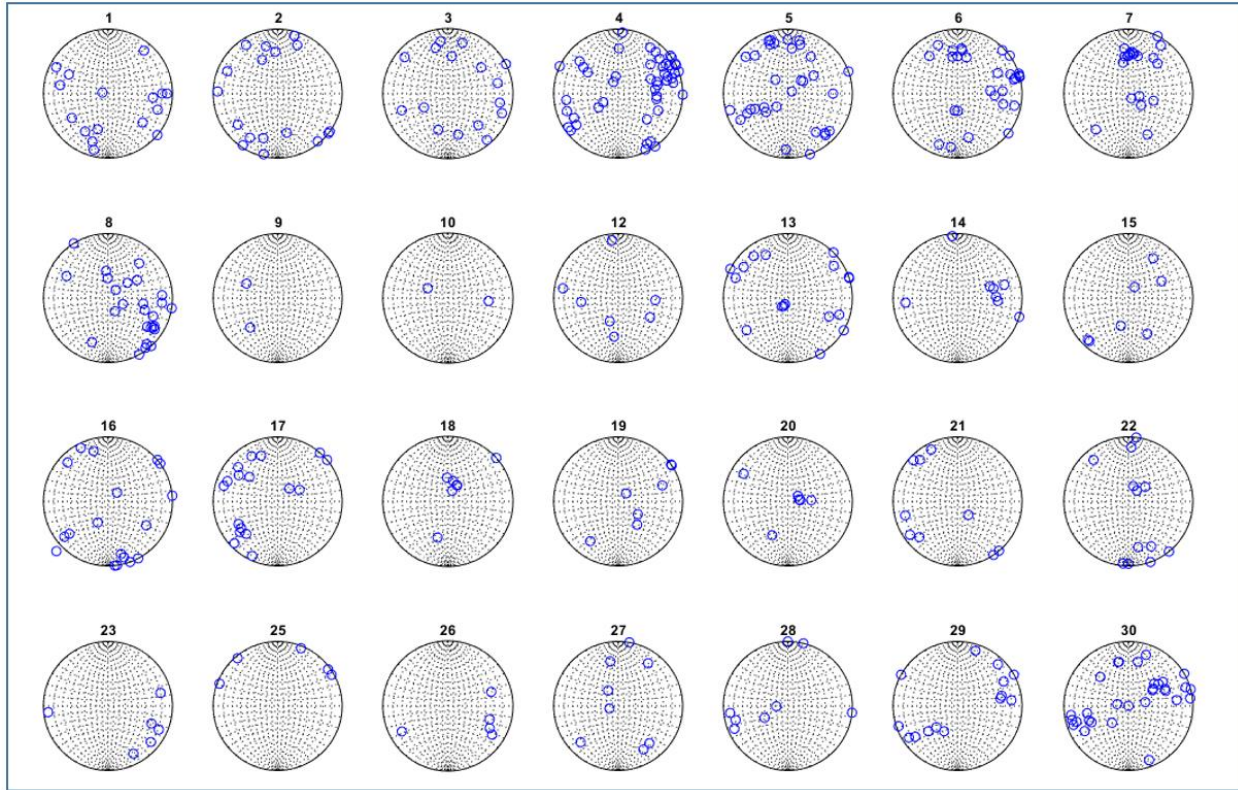


**Figure 11.** The projected poles of the measured fracture planes on stereonet in stations in Mount Cayley area.

**Table 1.** General information of the ground surface temperature monitoring stations in the Mount Meager Area recorded from 2020-09-21 to 2021-08-16.

Site #	Latitude	Longitude	Mean Temperature (°C)	T. standard deviation	Burial Depth (cm)	Soil Temperature (°C)	Soil Moisture (%)	Shadiness index
1	50.57770278	123.5199944	4.32	8.79	2	10	31	0.2
2	50.57559444	123.5187194	6.48	10.43	1	14	22	0.05
3	50.57400556	123.5247972	7.57	11.30	2	23	18	0.1
4	50.57322778	123.5176944	4.70	7.02	5	10	25	0.7
5	50.57492222	123.5129944	5.89	9.22	4	23	38	0.1
6	50.57126944	123.5211806	6.39	7.57	5	22	24.5	0.4
7	50.57136667	123.526825	5.88	7.28	4	21	25	0.5
8	50.56766111	123.5275722	7.23	9.79	2	21.6	27.4	0.3
9	50.56583056	123.5262722	5.68	8.37	5	16	25	0.5
10	50.56451667	123.5233389	5.45	7.30	3	29	24.3	0.6
11	50.56489167	123.5188944	5.63	7.31	3	23	28.4	0.8
12	50.56588889	123.513125	6.37	7.91	3	20	45	0.6
13	50.56480556	123.5058694	6.58	8.02	6	23	25	0.5
14	50.56262778	123.4980222	5.90	8.78	2	25	30.4	0.6
15	50.56313333	123.4924472	5.90	6.65	4	25	24.8	0.8
16	50.56595	123.4838806	5.93	7.12	3	25	22.5	0.7
17	50.569575	123.478425	6.34	6.70	6	25	24	0.6
18	50.57435278	123.4706944	5.40	6.42	4	25	23.5	0.8
19	50.58331667	123.4562917	6.80	8.69	2	33	25.5	0.6
20	50.57920833	123.4609528	7.75	9.87	3	30	23.1	0.4
21	50.57640833	123.4614694	6.73	6.87	7	25	17.3	0.9
22	50.57542778	123.4584778	5.24	6.49	4	25	21.3	0.95

**Table 2.** Ground surface temperature monitoring network station locations in the Mount Cayley area.

Logger #	Latitude	Longitude	Notes
1	50° 6'38.40"N	123°22'38.88"W	Ground temperature logger
2	50° 7'33.24"N	123°23'36.36"W	Ground temperature logger
3	50° 9'1.26"N	123°24'2.04"W	Ground temperature logger
4	50°10'14.28"N	123°23'18.78"W	Ground temperature logger
5	50°11'38.46"N	123°22'24.48"W	Ground temperature logger
6	50° 5'9.30"N	123°21'40.86"W	Ground temperature logger
7	50° 4'29.64"N	123°20'37.92"W	Ground temperature logger
8	50° 3'56.82"N	123°20'9.36"W	Ground temperature logger
9	50° 5'4.00"N	123°19'7.00"W	Ground temperature logger
10	50° 4'59.00"N	123°20'12.00"W	Ground temperature logger
11	50° 4'40.00"N	123°19'58.00"W	Ground temperature logger
12	50° 5'2.00"N	123°20'56.00"W	Ground temperature logger
13	50° 5'12.00"N	123°20'51.00"W	Ground temperature logger
14	50° 5'28.00"N	123°21'19.00"W	Ground temperature logger

**Table 3.** Soil samples in the Mount Meager and Mount Cayley areas from 2021 field work season.

Soil sample #	latitude	Longitude	Location	C#
SM. 1	50°34'39.73"N	123°31'11.98"W	M Meager	C-641147
SM. 2	50°34'32.14"N	123°31'7.39"W	M Meager	C-641148
SM. 3	50°34'26.42"N	123°31'29.27"W	M Meager	C-641149
SM. 4	50°34'23.62"N	123°31'3.70"W	M Meager	C-641150
SM. 5	50°34'29.72"N	123°30'46.78"W	M Meager	C-641151
SM. 6	50°34'16.57"N	123°31'16.25"W	M Meager	C-641152
SM. 7	50°34'16.92"N	123°31'36.57"W	M Meager	C-641153
SM. 8	50°34'3.58"N	123°31'39.26"W	M Meager	C-641154
SM. 9	50°33'56.99"N	123°31'34.58"W	M Meager	C-641155
SM. 10	50°33'52.26"N	123°31'24.02"W	M Meager	C-641156
SM. 11	50°33'53.61"N	123°31'8.02"W	M Meager	C-641157
SM. 12	50°33'57.20"N	123°30'47.25"W	M Meager	C-641158
SM. 13	50°33'53.30"N	123°30'21.13"W	M Meager	C-641159
SM. 14	50°33'53.30"N	123°30'21.13"W	M Meager	C-641160
SM. 15	50°33'47.28"N	123°29'32.81"W	M Meager	C-641161
SM. 16	50°33'57.42"N	123°29'1.97"W	M Meager	C-641162
SM. 17	50°34'10.47"N	123°28'42.33"W	M Meager	C-641163
SM. 18	50°34'27.67"N	123°28'14.50"W	M Meager	C-641164
SM. 19	50°34'59.94"N	123°27'22.65"W	M Meager	C-641165
SM. 20	50°34'45.15"N	123°27'39.43"W	M Meager	C-641166
SM. 21	50°34'35.07"N	123°27'41.29"W	M Meager	C-641167
SM. 22	50°34'31.54"N	123°27'30.52"W	M Meager	C-641168
SM. 23	50°30'28.7"N	123°27'56.1"W	M Meager	C-641169
SQ 1	50° 6'38.40"N	123°22'38.88"W	M Cayley	C-641170
SQ 2	50° 7'33.24"N	123°23'36.36"W	M Cayley	C-641171
SQ 3	50° 9'1.26"N	123°24'2.04"W	M Cayley	C-641172
SQ 4	50°10'14.28"N	123°23'18.78"W	M Cayley	C-641173
SQ 5	50°11'38.46"N	123°22'24.48"W	M Cayley	C-641174
SQ 6	50° 5'9.30"N	123°21'40.86"W	M Cayley	C-641175
SQ 7	50° 4'29.64"N	123°20'37.92"W	M Cayley	C-641176
SQ 8	50° 3'56.82"N	123°20'9.36"W	M Cayley	C-641177
SQ 9	50° 5'4.00"N	123°19'7.00"W	M Cayley	C-641178
SQ 10	50° 4'59.00"N	123°20'12.00"W	M Cayley	C-641179
SQ 11	50° 4'40.00"N	123°19'58.00"W	M Cayley	C-641180
SQ 12	50° 5'2.00"N	123°20'56.00"W	M Cayley	C-641181
SQ 13	50° 5'12.00"N	123°20'51.00"W	M Cayley	C-641182
SQ 14	50° 5'28.00"N	123°21'19.00"W	M Cayley	C-641183

**Table 4.** Geological observation and fracture measurement stations in the Mount Cayley area from the 2021 fieldwork season.

Station #	Latitude	Longitude	Notes
1	50° 3'60.00"N	123° 8'51.00"W	Geology and fracture
2	50° 3'57.00"N	123° 8'46.00"W	Geology and fracture
3	50° 7'4.00"N	123° 7'14.00"W	Geology and fracture
4	50° 6'22.00"N	123° 7'13.00"W	Geology and fracture
5	50° 6'25.00"N	123° 7'9.00"W	Geology and fracture
6	50° 7'10.00"N	123° 7'16.00"W	Geology and fracture
7	50° 7'21.00"N	123° 7'24.00"W	Geology and fracture
8	50° 7'27.00"N	123° 7'27.00"W	Geology and fracture
9	50° 9'15.00"N	123° 9'10.00"W	Geology and fracture
10	50°10'50.00"N	123°10'2.00"W	Geology and fracture
11	50° 8'37.00"N	123° 8'32.00"W	Observation
12	50° 7'19.00"N	123°23'38.00"W	Geology and fracture
13	50° 7'7.00"N	123°23'32.00"W	Geology and fracture
14	50° 6'59.00"N	123°23'15.00"W	Geology and fracture
15	50° 1'40.00"N	123°20'31.00"W	Geology and fracture
16	50° 1'29.00"N	123°20'21.00"W	Geology and fracture
17	50° 0'7.00"N	123°19'30.00"W	Geology and fracture
18	49°59'48.00"N	123°19'23.00"W	Geology and fracture
19	49°59'3.00"N	123°19'18.00"W	Geology and fracture
20	49°58'29.00"N	123°18'20.00"W	Geology and fracture
21	49°57'21.00"N	123°17'55.00"W	Geology and fracture
22	49°54'57.00"N	123°17'33.00"W	Geology and fracture
23	50° 7'1.00"N	123° 7'18.00"W	Geology and fracture
24	50° 8'1.00"N	123° 7'47.00"W	Observation
25	50° 8'10.00"N	123° 7'40.00"W	Geology and fracture
26	50° 6'20.00"N	123° 7'11.00"W	Geology and fracture
27	50° 5'44.00"N	123° 6'47.00"W	Geology and fracture
28	50° 4'33.00"N	123° 6'31.00"W	Geology and fracture
29	50° 4'26.00"N	123° 6'22.00"W	Geology and fracture
30	50° 4'10.00"N	123° 5'50.00"W	Geology and fracture

**Table 5.** Rock samples from the Mount Cayley area sampled in the 2021 season.

Rock sample Label	Latitude	Longitude	Location	Sample type	GSC C#
M6A	50°34'16.57"N	123°31'16.25"W	M Meager	Rock sample	C-641135
M6B	50°34'16.57"N	123°31'16.25"W	M Meager	Rock sample	C-641136
Cayley 1	50°04'0.0"N	123°08'51.0"W	Callaghan area	Rock sample	C-641137
Cayley 2	50°03'57"N	123°08'46"W	Callaghan area	Rock sample	C-641138
Cayley 3	50°07'14.0"N	123°07'14.0"W	Callaghan area	Rock sample	C-641139
Cayley 4	50°06'22.0"N	123°07'13.0"W	Callaghan area	Rock sample	C-641140
Cayley 5	50°06'25.07"N	123°07'09.0"W	Callaghan area	Rock sample	C-641141
Cayley 6	50°07'02.0"N	123°07'24.0"W	Callaghan area	Rock sample	C-641142
Cayley 7	50°09'15.0"N	123°09'10.0"W	Callaghan area	Rock sample	C-641143
SQV 8	50° 7'7.00"N	123°23'32.00"W	Squamish Area	Rock sample	C-641144
SQV 9	49° 58'29.00"N	123°18'20.00"W	Squamish Area	Rock sample	C-641145
SQV 1	50° 6'38.40"N	123°22'38.88"W	Squamish Area	Rock sample	C-641146

**Appendix A.** GST monitoring records of 22 loggers in the Mount Meager area during 2020-september to 2021 August (in separate Excel files).

**Appendix B.** Fracture measurements in the Mount Cayley area in the 2021 field season (in separate Excel file).

## Acknowledgements

This is an output from the Geoscience for New Energy Supply program of Natural Resources Canada. Natural Resource Canada and Geoscience BC provided financial support for the data collection and fieldwork.

## References

- Arthur, D., and S. Vassilvitskii, 2007, "K-means++: The Advantages of Careful Seeding." SODA '07: Proceedings of the Eighteenth Annual ACM-SIAM Symposium on Discrete Algorithms. 2007, pp. 1027– 1035. DOI: [10.1145/1283383.1283494](https://doi.org/10.1145/1283383.1283494).
- Chen, Z., Grasby S.E., Liu, X. and Yuan W., (submitted) ,Ground surface temperature monitoring data analysis and implications for geothermal exploration in volcanic areas, Mount Meager, western Canada.

- Davis J., 2002. *Statistics and Data Analysis in Geology*, 3rd edn. John Wiley and Sons Inc., New York, p. 656. ISBN: 978-0-471-17275-8.
- Lewis, J.F., and Souther, J.G., 1978, Meager Mt., B.C.-Possible Geothermal Energy Resource: EMR, Earth Physics Branch, Geothermal Series No. 9, Ottawa, 17 pp.
- Lewis, TJ, Jessop AM, and Judge, AS., 1985. Heat flux measurements in southwestern British Columbia: the thermal consequences of plate tectonics. *Canadian Journal of Earth Science*, Vol. 22, p.1262-1273.
- Outcalt SJ, Nelson FE and Hinkel KM., 1990, The zero-curtain effect: Heat and mass transfer across an isothermal region in freezing soil. *Water Resources Research* vol. 26, no.7, p.1509-1516. <https://doi.org/10.1029/WR026i007p01509>
- Pollack HN, Hurter SJ and Johnson JR, 1991 Heat flow from Earth's interior: Analysis of the global data set, *Reviews of Geophysics*, 31, 3 / August 1993, p. 273 [Archived](#) 2011-08-11 at the [Wayback Machine](#) doi:10.1029/93RG01249.
- Tsao J, Lewis N, and Crabtree G, 2006 Solar FAQs. U.S. Department of Energy, <https://www.sandia.gov/~jytsao/Solar%20FAQs.pdf>